universität wien

DISSERTATION | DOCTORAL THESIS

Titel | Title

Derivation, Analysis and Simulation of Volume Exclusion Interaction Models of Elongated Particles and of Network Formation Models

verfasst von | submitted by

Dipl.-Ing. Claudia Mußnig-Wytrzens BSc

angestrebter akademischer Grad | in partial fulfilment of the requirements for the degree of

Doktorin der Naturwissenschaften (Dr.rer.nat.)

Wien | Vienna, 2025

Studienkennzahl lt. Studienblatt | Degree programme code as it appears on the student record sheet:	UA 796 605 405
Dissertationsgebiet lt. Studienblatt | Field of study as it appears on the student record sheet:	Mathematik
Betreut von | Supervisor:	Univ.-Prof. Sara Merino Aceituno PhD ao. Univ.-Prof. i.R. Dr. Christian Schmeiser

Dedicated to Maria and all young girls whose scientific curiosity leads them to explore the world. May you shape the future of science.

Acknowledgements

First of all, I would like to express my deepest gratitude to my supervisor, Sara Merino Aceituno, who not only introduced me to the fascinating field of kinetic theory but also supported me throughout the past years with my mathematical questions and struggles. I greatly enjoyed our discussions – on mathematical topics and beyond –, and I am immensely grateful for her support, encouragement, time, feedback, and generosity in sharing her wisdom. She has always cared deeply about the well-being of her students; even during the pandemic, she made time for us and looked out for our needs.

I would also like to thank my co-supervisor, Christian Schmeiser, for his continuous interest in my work, for consistently raising inspiring research questions, and especially for introducing me to the Summer Schools in Weißensee.

I am very grateful to my collaborators – Pedro Aceves Sanchez, Pierre Degond and Havva Yoldas – for their time, the fruitful discussions and for generously sharing their expertise.

My special thanks go to Magali Ribot and Marie-Therese Wolfram for kindly agreeing to review my thesis.

This work would not have been possible without the financial support of the Wiener Wissenschafts-, Forschungs- und Technologiefonds (WWTF) and the Österreichischer Wissenschaftsfonds (FWF). I am also deeply grateful to the European Women in Mathematics, whose support made it possible for me to attend conferences with my little child.

I would also like to thank all the members of the research group I have been part of over the past few years – Gianluca, Havva, Leo, and Raphael. Thank you for your openness, for the time you devoted to (mathematical) discussions and for answering my questions. Talking to you always lifted my spirits. Special thanks to my academic siblings, Carmen and Steffen, for sharing this journey with me, and to Steffen in particular for all the coding tips he shared with me – doing a PhD during the pandemic was much more enjoyable with him. Thanks also to Angelika – not only for proofreading parts of my thesis, but also for her mentoring and all our tea times.

Many thanks also to all my previous and current office and floor mates for the welcoming atmosphere, all the occasional chit-chat, their encouraging words and open ears, as well as the fun time outside of work. In particular, I would like to thank Andras, Andrea, Caroline, Chiara, Giancarlo, Giulia, Laura, Leo, Mateusz, Noema, and Willi.

Moreover, I am immensely grateful to all my friends who have supported me in so many different ways over the last few years – especially to Anna, Alex, Coelestin, Cordula, Bianca, Hanna, Isi, Josipa, Petra, Phil, Steffi, and Stefan. Without them, this journey would have been much less fun. Thank you for sharing many happy memories, believing in me and cheering me up! Mein Dank gilt auch Ingrid Wiedner für ihre kontinuierlich aufbauenden, stärkenden und ermutigenden Worte.

Mein tiefster Dank gebührt meiner Familie und meiner Schwiegerfamilie. Danke, dass Ihr mich in allen Lebenslagen unterstützt, an mich glaubt und mir zur Seite steht! Danke für all Eure emotionale, zeitliche und finanzielle Unterstützung.

Ich finde kaum Worte, um auszudrücken, wie dankbar ich Dir, Fabian, für all Deine Unterstützung und Deine ermutigenden Worte bin. Es bereitet mir große Freude, mit Dir über

Mathematik zu diskutieren – auch wenn wir beide oft nicht genau wissen, wovon der andere spricht. Danke auch für den Halt und die Liebe, die Du mir in den letzten Jahren gegeben hast!

Zu guter Letzt gebührt Dir, Maria, der größte Dank von allen. Du bist der wichtigste Mensch in meinem Leben. Danke, dass Du mir die Möglichkeit und die Zeit gibst, gemeinsam mit Dir zu wachsen. Deine Fragen und Deine wissenschaftliche Neugier sind meine Quelle der Inspiration und waren ein treibender Motor beim Abschluss dieser Arbeit.

Kurzfassung

Die vorliegende Arbeit befasst sich mit emergenten Phänomenen in Zusammenhang mit biologischen Systemen mittels Modellierung, formaler Herleitungen und numerischer Simulationen multiskaliger Dynamiken. Eine zentrale Herausforderung in der Entwicklung der Modelle besteht darin, nicht nur die mikroskopischen Teilcheninteraktionen realistisch zu erfassen, sondern gleichzeitig auch auf meso- und makroskopischer Ebene mathematisch und numerisch handhabbar zu bleiben. Hierzu wenden wir Methoden der kinetischen Theorie, des Coarse-Grainings sowie der Numerik in drei komplementären Projekten an.

Zunächst führen wir ein teilchenbasiertes Modell ein, welches die Exklusionsinteraktionen anisotroper Teilchen aufgrund ihres Volumens mithilfe eines gaußschen Repulsionspotentials beschreibt. Mittels Mean-Field- und hydrodynamischer Grenzwerte leiten wir formal die zugehörigen kinetischen und makroskopischen Gleichungen her und zeigen, dass dieses Potential auf natürliche Weise nematische Ausrichtung sowie nichttriviale räumliche Effekte induziert. Ergänzend lösen wir das teilchenbasierte System numerisch, um Parameterbereiche zu identifizieren, in denen die makroskopische Beschreibung des Systems gültig ist. Der hydrodynamische Grenzwert führt zu einem nichtlinearen Diffusionsterm für die Teilchendichte, der von der Anisotropie der Teilchen beeinflusst wird, sowie zu einer gekoppelten Transport-Diffusions-Gleichung für die mittlere Orientierung der Teilchen.

Des Weiteren präsentieren und analysieren wir eine FFT (Fast Fourier Transformation)-basierte Spektralmethode zur Simulation eines makroskopischen Modells unter periodischen Randbedingungen, das die Bildung biologischer Netzwerke erfasst. Diese Methode ist verglichen zu impliziten Verfahren einfacher zu implementieren und ermöglicht effiziente Berechnungen. Wir reproduzieren den in der Literatur beschriebenen Einfluss der Aktivierungs- und Diffusionsparameter sowie des metabolischen Exponenten auf die Netzwerkmorphologie und analysieren das Konvergenzverhalten in Bezug auf die Gitterverfeinerung.

Abschließend betrachten wir ein Modell zur Fasernetzwerkbildung. In diesem Modell können Fasern Bindungen miteinander eingehen, die sich auch spontan wieder lösen. Wir erweitern dieses Modell um ein Repulsionspotential und leiten die entsprechende kinetische Gleichung formal her. Im Zuge dessen identifizieren wir zwei Annahmen, die für den rigorosen Mean-Field-Beweis entscheidend sind. Somit verdeutlicht diese Herleitung wesentliche analytische Herausforderungen, deren Bewältigung für zukünftige rigorose Beweise zentral sein wird.

Abstract

This thesis investigates emergent phenomena associated with biological systems through the modelling, derivation, analysis, and simulation of multiscale dynamics. A central challenge is to develop models that both capture microscopic particle interactions and remain mathematically and computationally tractable at larger scales. To address this, we employ kinetic theory, coarse-graining and numerical simulations by investigation of three complementary projects.

First, we introduce a particle model for anisotropic particles interacting via a Gaussian-type repulsive potential that encodes volume exclusion. We formally derive the corresponding kinetic and macroscopic equations via the mean-field and hydrodynamic limits and demonstrate that this repulsion naturally induces nematic alignment and non-trivial spatial effects. Moreover, we perform numerical simulations of the particle system to identify parameter regimes supporting the continuum description. The macroscopic derivation reveals a nonlinear diffusion of the particle density, modulated by particle anisotropy, and a coupled transport–diffusion dynamics for the mean orientation of the particles.

Next, we propose and study an FFT (Fast Fourier Transformation)-based spectral method to simulate a continuum model of biological network formation under periodic boundary conditions. The method is simpler to implement than implicit schemes and enables efficient computations. We reproduce the previously documented influence of the activation, diffusion and metabolic exponent parameters on the network morphology and report grid-convergence results.

Lastly, we extend a fiber network model with linking and unlinking dynamics by incorporating a repulsive potential. We provide a formal derivation of the corresponding kinetic equation and identify two assumptions that are critical for establishing a rigorous mean-field limit. Hence, this derivation clarifies key analytical challenges for future rigorous proofs.

Contents

1 Introduction

Many real-life systems exhibit complex phenomena or large-scale structures that arise from the underlying interactions between the individual particles of the system. Examples of such emergent phenomena include collective dynamics such as schooling of fish, flocking of birds, pedestrian dynamics, traffic flow, network formation (e.g., leaf venation, fiber networks in tissues, capillary formation, or ant trails), opinion dynamics, weather patterns, tumour growth, and tissue development. These large-scale structures are not directly encoded in the interaction rules between individuals but rather emerge from the collective interplay of many interacting particles. Predicting how such emergent behaviours develop from the underlying particle dynamics is generally not straightforward. In this thesis, we will employ kinetic theory to investigate emergent phenomena within specific systems. To facilitate this analysis, **kinetic theory** distinguishes between three levels of description: microscopic, mesoscopic, and macroscopic.

At the **microscopic level**, the system is described with detailed information about each particle or individual. This level provides a comprehensive description of the system, including the position and velocity of every molecule in a gas or the specific characteristics and locations of all cells in a tissue.

The next scale is the **mesoscopic level**, which refers to an intermediate level of description. Here, the system is characterised by the proportions of particles in various states. For instance, this could involve describing the proportion of gas molecules at specific positions and velocities or the fraction of cells located in specific areas with defined properties. At the mesoscopic level, less information is retained compared to the microscopic level.

Finally, the **macroscopic level** focuses on observable quantities that describe collective behaviours of the system at larger scales, such as the average velocity of particles in a given area. At this level, one typically captures pattern formation and emergent behaviour. Compared to the mesoscopic scale, the macroscopic description contains less information, as it results from an averaging process that reduces the detailed structure of the mesoscopic description.

In mathematical terms, at the microscopic level, the dynamics of individual particles or agents are modelled explicitly through interaction rules. Here, the evolution in time of particle i represented by, for example, its position $X_i \in \mathbb{R}^d$ and velocity $v_i \in \mathbb{R}^d$ is described by deterministic or stochastic processes.
At the mesoscopic level, the focus shifts to statistical descriptions in terms of distribution functions $f = f(t, x, v)$, as provided by kinetic theory. Kinetic theory was originally developed in the context of gas dynamics in mathematical physics. One of the most prominent kinetic equations is the Boltzmann equation [23, 32]. The distribution $f = f(t, x, v)$ does not contain the information of each individual particle, but rather $f(t, x, v)\,\mathrm{d}x\,\mathrm{d}v$ gives the average number of particles in position x with velocity v at time t in the volume $\mathrm{d}x\,\mathrm{d}v$. Thus, compared to an individual-based model, we lose the information on the individual particles. Therefore, kinetic equations for $f = f(t, x, v)$ give the evolution of the average behaviour of the system over time. Finally, at the macroscopic level, the collective behaviour of the system is captured by continuum equations for quantities like the density $\rho(t, x)$ and the mean velocity $\bar{v}(t, x)$ of the particles, which depend only on time and space.

As mentioned, understanding the principles of emergence is essential for explaining the oc-

currence of observable phenomena. The general goal is to link the different levels of description using mathematical methods. In doing so, we gain insight into the mechanisms of emergence, so that these three levels form a natural hierarchy of models, each reducing complexity while retaining essential features of the system.

However, deriving effective kinetic and macroscopic models from particle interactions, while retaining essential features of the underlying microscopic system, remains a central challenge. A key concept in this context is the method of coarse-graining, i.e., the process of reducing the complexity of the microscopic model in order to obtain effective descriptions at larger scales. Here, we will focus on the method of the mean-field limit, i.e., letting the numbers of particles N go to infinity, to go from microscopic to mesoscopic scales and the hydrodynamic limit, i.e., rescaling the system by a small parameter ε and let ε go to zero, in order to derive according macroscopic equations from the mesoscopic description of a system. Figure 1.1 provides a short graphical overview of the connection of the different levels of description. Examples of microscopic systems include particle interaction models, which might involve Newton dynamics (but not necessarily), such as e.g., [37,83,84,99]. As already mentioned, one of the most famous kinetic equations is the Boltzmann equation [23,32]. Note, that it is not obtained as a mean-field limit from the underlying Newton dynamics [50,61]. Other prominent types of kinetic equations obtained as mean-field limits are Vlasov-type [81] or Fokker-Planck-type equations [93]. At the macroscopic level, we are considering hydrodynamic equations, which also include Euler-type equations [13, 14, 95]. Nowadays, the applications of kinetic theory and coarse-graining are extended far beyond the classical context of gases to for example liquid crystals (see e.g., [28, 41, 59]), swarm dynamics (see e.g., [30, 31, 42, 44]), opinion formation (see e.g., [4, 5, 52–54]), pedestrian dynamics (see e.g., [1, 38, 57, 75]) and biological systems (see e.g., [7, 34, 39, 74, 91]).

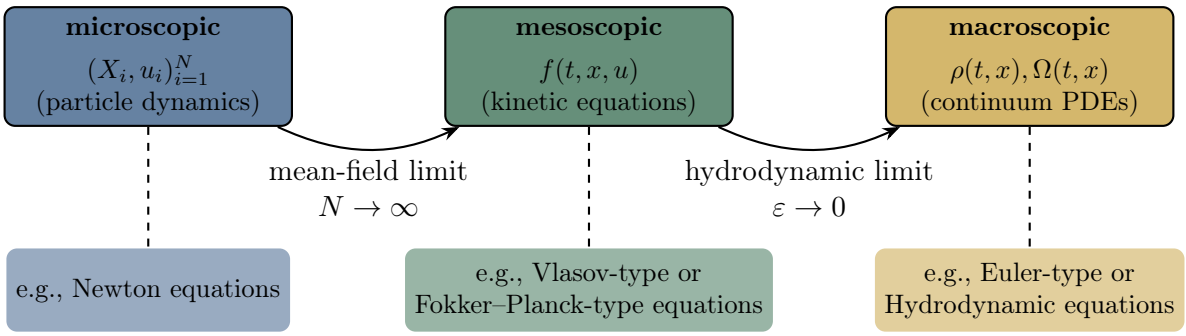

Figure 1.1: Schematic illustration of the connection between microscopic, mesoscopic, and macroscopic model descriptions with representative examples. The curved arrows indicate the mathematical tools, i.e., the mean-field limit ($N \to \infty$) and the hydrodynamic limit ($\varepsilon \to 0$), in order to link the levels. A detailed example is given in Section 1.1.

To gain full insight into models across different scales of description, numerical simulations play a crucial role, as many systems are too complex to be fully understood solely analytically. Hence, numerical experiments are vitally important for exploring emergent behaviour and for investigating the model dynamics beyond the reach of theory. Especially in the context of coarse-graining, numerical simulations are a fundamental tool to assess whether mesoscopic and macroscopic descriptions of a system capture the behaviour observed at the microscopic level. They also help to determine the influence of the system's parameters on the emerging dynamics.

Therefore, developing appropriate numerical methods is essential for gaining insight into the equations and understanding the connection between different scales.

This PhD thesis addresses several challenges and complements current research in the areas outlined above. In Chapter 2, we derive not only the kinetic equation but also the macroscopic description for a discrete system of non-overlapping ellipsoidal particles, and we support the analysis with numerical simulations of the underlying particle system. Chapter 3 introduces a new numerical method for a continuum model that captures the emergence and evolution of biological networks. Finally, Chapter 4 is devoted to the derivation of a kinetic equation for a system of fibers undergoing dynamic linking and unlinking processes.

In the following, we complement this conceptual overview with a short introduction to the formal derivation of kinetic and macroscopic models from the underlying microscopic system.

1.1 Bridging Microscopic, Mesoscopic, and Macroscopic Models: A Formal Overview and Example

The purpose of this section is to provide a short formal overview of the coarse-graining process depicted in Figure 1.1, which forms the theoretical foundation for the models developed in Chapters 2 and 4. We briefly outline the connection between microscopic particle models and their mesoscopic and macroscopic descriptions. This illustrates that kinetic theory serves as an intermediate bridge between the microscopic dynamics and the macroscopic description. The following sections are based on [33, 49, 96, 100].

1.1.1 Microscopic Description

In the following, we will exemplarily consider an interacting particle system of N particles with positions $X_i \in \mathbb{R}^d$ and velocities $V_i \in \mathbb{R}^d$ for all particles $i \in \{1, \dots, N\}$ and where d is the dimension of the considered space. The motion of each particle over time is described by a system of ordinary or stochastic differential equations (ODEs or SDEs), depending on whether random fluctuations are included. A general formulation of such a system reads

$$\begin{aligned} \mathrm{d}X_i(t) &= V_i(t)\,\mathrm{d}t \\ \mathrm{d}V_i(t) &= F_i(t, X_1(t), \dots, X_N(t), V_1(t), \dots, V_N(t))\,\mathrm{d}t + \sqrt{2D}\,\mathrm{d}B_i^t \end{aligned}$$

for all $i \in \{1, \dots, N\}$ and where F_i denotes the sum of all deterministic forces acting on particle i (e.g., nematic alignment, repulsion, attraction, or external forces from the surrounding tissue). Furthermore, $(B_i^t)_{i=1,\dots,N}$ are independent Brownian motions, also known as the Wiener process, which model stochastic perturbations acting on particle i at time t. The constant $D > 0$ denotes the noise intensity. The trajectory of each particle is thus governed by the combined effects of deterministic particle interactions and random motion.

In the following, we will state the discrete Vicsek model as one of many examples of such particle interaction models. We will also present its corresponding mesoscopic and macroscopic descriptions in the subsequent sections.

The discrete Vicsek model. The original Couzin-Vicsek model [36,99] was first introduced as a time-discrete algorithm, and it describes the particles' interactions for animal societies such

as fish schools or bird flocks. A particle is described by its position $X_i \in \mathbb{R}^3$ and its orientation $\omega_i \in \mathbb{S}^2$, where $\mathbb{S}^2$ is the 2-dimensional unit sphere, for all $i = 1, \dots, N$, with N being the total number of particles. A particle is moving with constant speed $c > 0$ with orientation ω_i, and it modifies its orientation over time to adopt the mean orientation $\bar{\omega}_i$ of its neighbours, up to some noise. Hence, particle i aligns its orientation with the mean orientation of its surrounding particles. In [49], Degond and Motsch reformulated this model in terms of a time continuous dynamical system, which reads

$$\begin{aligned} \mathrm{d}X_i(t) &= c\omega_i(t)\,\mathrm{d}t, \\ \mathrm{d}\omega_i(t) &= P_{\omega_i^\perp} \circ \left(\nu\bar{\omega}_i(t)\,\mathrm{d}t + \sqrt{2D}\,\mathrm{d}B_i^t\right), \\ \text{with} \quad \bar{\omega}_i(t) = \frac{J_i(t)}{|J_i(t)|}, &\quad J_i(t) = \sum_{j,|X_j - X_i| \le R} \omega_j \end{aligned}$$

for all particles $i \in \{1, \dots, N\}$. Here, $P_{\omega_i^\perp}$ denotes the orthogonal projection onto the subspace orthogonal to ω_i and $(B_i^t)_{i=1,\dots,N}$ represents independent Brownian motions. The equation describing the orientation's evolution must be understood in the Stratonovich sense, which is indicated by '$\circ$'. This guarantees that ω_i stays on the sphere $\mathbb{S}^2$ for all times. The parameter $\nu > 0$ gives the strength of alignment, and the parameter $R > 0$ gives the radius of interaction of the particles.

1.1.2 Mesoscopic Description

As the number of particles N for the microscopic dynamics increases, it becomes infeasible and computationally expensive to track the individual trajectories of all the particles. Moreover, since the process $(X_i(t), V_i(t))_{i=1}^N$ evolves in a space of dimension $2dN$, taking the limit $N \to \infty$ will be challenging. Hence, it becomes both unnecessary and inefficient to retain full microscopic details. To obtain a reduced statistical description of the model, we assume that the evolution of each particle depends only on its current state (Markov property) and that all particles are indistinguishable. Furthermore, we introduce the empirical measure $f^N(t, x, v) \in \mathcal{P}(\mathbb{R}^d \times \mathbb{R}^d)$, defined by

$$f^N(t, x, v) := \frac{1}{N} \sum_{i=1}^{N} \delta_{(X_i(t), V_i(t))}(x, v).$$

Here, $\delta_{(X_i(t),V_i(t))}(x, v) = \delta_{X_i(t)}(x)\delta_{V_i(t)}(v)$ represents the Dirac delta distribution on $\mathbb{R}^d \times \mathbb{R}^d$ located at $(X_i(t), V_i(t))$ at time t. Although f^N is a random measure, it belongs to the common space of probability measures $\mathcal{P}(\mathbb{R}^d \times \mathbb{R}^d)$ for all N.

As already mentioned, we want to compute the limit $N \to \infty$, i.e., the mean-field limit, in order to coarse-grain the microscopic system and obtain an averaged statistical model, namely, the kinetic equation. In terms of the empirical random measure f^N, this corresponds to determining its limit, provided it exists. Therefore, we consider a sequence of deterministic initial empirical measures $f_0^N = f^N(0, x, v)$ such that $f_0^N \to f_0$ as $N \to \infty$ for some deterministic probability density $f_0 = f(0, x, v)$. Then, the mean-field limit for this sequence holds true if and only if for almost all $t > 0$

$$f^N(t, x, v) \to f(t, x, v) \qquad \text{as } N \to \infty,$$

where $f = f(t, x, v)$ denotes the solution of the corresponding kinetic equation with initial condition f_0. The function $f(t, x, v)\,\mathrm{d}x\,\mathrm{d}v$ gives the proportion of particles located at the space

element $\mathrm{d}x\,\mathrm{d}v$ at time t.

To formally derive the corresponding kinetic equation, one considers an arbitrary test function, which is smooth with compact support, i.e., $\varphi(x,v) \in C_c^\infty(\mathbb{R}^d \times \mathbb{R}^d)$, and computes

$$\frac{\mathrm{d}}{\mathrm{d}t}\langle \varphi, f_t^N \rangle, \qquad \text{where } \langle \varphi, f^N \rangle := \int_{\mathbb{R}^{2d}} \varphi(x,v)\,\mathrm{d}f^N.$$

Then, by applying Itô's formula to the microscopic system, substituting $\mathrm{d}X_i$, $\mathrm{d}V_i$ and reformulating the resulting expression in weak form, one obtains a closed equation for f^N. Eventually, passing formally to the limit $N \to \infty$ leads to the desired kinetic equation of the mesoscopic system. A concrete example of such a kinetic equation is given by

$$\partial_t f(t,x,v) + \nabla_x \cdot (F(t,x,v)f(t,x,v)) + \nabla_v \cdot (F(t,x,v)f(t,x,v)) = D\Delta_v f(t,x,v).$$

Hereinafter, we provide the mesoscopic description of the Vicsek model.

Vicsek model - kinetic formulation. In [49], Degond and Motsch not only formulated the Couzin-Vicsek algorithm in terms of a time continuous SDE but also derived a mesoscopic description. The corresponding kinetic equation for the particle distribution function $f = f(t,x,\omega)$ reads

$$\partial_t f + c\omega \cdot \nabla_x f = D\Delta_\omega f - \nabla_\omega \cdot (Ff),$$

where F and $\bar{\omega}$ are defined as

$$\begin{aligned} F(t,x,\omega) &= \nu(\cos\bar{\theta})P_{\omega^\perp}\bar{\omega}(t,x,\omega), \quad \cos\bar{\theta} = \omega\cdot\bar{\omega}, \\ \bar{\omega}(t,x,\omega) &= \frac{J(t,x)}{|J(t,x)|}, \quad J(t,x) = \int_{y\in\mathbb{R}^3, v\in\mathbb{S}^2} K(|x-y|)vf(t,y,v)\,\mathrm{d}y\,\mathrm{d}v. \end{aligned}$$

The operator $\nabla_\omega\cdot$ is the divergence on the 2-dimensional unit sphere $\mathbb{S}^2$ and Δ_ω the Laplace operator on $\mathbb{S}^2$. Moreover, $K(|x|)$ is the observation kernel typically given by the indicator function of a ball centred at the origin with radius R.

Additionally, we state that the second term on the left side of the mean-field limit represents a transport term and thus accounts for free motion in direction ω with constant speed c. The right-hand side of the equation describes changes in the orientation ω. More precisely, the divergence term containing F features the alignment interactions, and the diffusion term with diffusion constant D arises from the Brownian motion and thus accounts for random motion.

1.1.3 Macroscopic Description

By passing from the microscopic description of the particle system to the mesoscopic kinetic formulation, we have already reduced the level of detail contained in the model. We seek to further coarse-grain the model, as we want to describe macroscopic observables, i.e., averaged quantities such as the particle density $\rho_t = \rho(t,x)$ and the mean velocity $\bar{v}_t = \bar{v}(t,x)$, capturing emergent phenomena at large scales. These macroscopic quantities are moments of the distribution function $f = f(t,x,y)$

$$\rho(t,x) = \int_{\mathbb{R}^d} f(t,x,v)\,\mathrm{d}v, \quad \rho(t,x)\bar{v}(t,x) = \int_{\mathbb{R}^d} vf(t,x)\,\mathrm{d}v.$$

To derive their evolution equations, we will focus on a formal derivation from the kinetic equation via dimensional scaling, performing the hydrodynamic limit $\varepsilon \to 0$ and moment-closure methods. First, we perform a dimensional analysis to obtain a dimensionless form of the kinetic equation. Thus, we introduce some microscopic reference length x_0 and time t_0 such that $\tilde{x} = \frac{x}{x_0}, \tilde{t} = \frac{t}{t_0}$, where $\tilde{x}$ and $\tilde{t}$ denote the dimensionless microscopic variables for space and time, and all other variables, parameters and functions become dimensionless as well.
Next, we scale either space and time or some modelling parameters by some $\varepsilon > 0$ in order to carry out the hydrodynamic limit. This procedure can lead, for instance, to hydrodynamic-type equations or diffusion limits, depending on the form of the kinetic operator and the scaling regime under consideration. In particular, considering a hyperbolic scaling for space and time, the dimensionless kinetic equation is rewritten in terms of the new macroscopic variables $\hat{x} := \varepsilon\tilde{x}$ and $\hat{t} := \varepsilon\tilde{t}$. This means that a small change in space or time at the macroscopic level will become a large change in space or time at the microscopic level. Hence, such a scaling can also be interpreted as zooming out of space and speeding up time in order to capture the macroscopic behaviour of the system compared to its microscopic dynamics.

Considering a hyperbolic scaling in space and time for the generic dimensionless kinetic equation stated in the paragraph on the mesoscopic description can then be expressed, for example, as

$$\partial_{\hat{t}} f^\varepsilon + \hat{v} \cdot \nabla_{\hat{x}} f^\varepsilon = \frac{1}{\varepsilon} Q(f^\varepsilon),$$

with $f^\varepsilon := \hat{f}(\hat{t}, \hat{x}, \hat{v})$ and where $Q(f^\varepsilon) = \hat{D}\Delta_{\hat{v}} f^\varepsilon - \nabla_{\hat{v}} \cdot (\hat{F}(\hat{t}, \hat{x}, \hat{v}) f^\varepsilon)$ is the so called collision operator, which carries the information on the changes in the velocity $\hat{v}$. As we formally perform the hydrodynamic limit, i.e., $\varepsilon \to 0$ and thus $Q(f^\varepsilon) = 0$, we assume that $f^\varepsilon \to f_0 \in \ker Q$. Hence, the characterisation of the local equilibrium f_0 is essential to derive the macroscopic equations. For a general Fokker-Planck-type collision operator (as given above), the elements of the kernel and thus the equilibria are given by $f_0 = \rho(\hat{t}, \hat{x}) M(\hat{v}, \bar{v})$. Here, $M(\hat{v}, \bar{v})$ is a normalised distribution and its particular shape (such as a Maxwellian or von Mises-Fisher distribution) depends on the collision operator and thus the microscopic interactions.

As mentioned in the beginning, these macroscopic observables $\rho(\hat{t}, \hat{x})$ and $\bar{v}(\hat{t}, \hat{x})$ are defined via the first and second moments of f. The corresponding evolution equations for these quantities are derived by integrating the kinetic equation with respect to $\hat{v}$. Hence, multiplying the kinetic equation by 1 and $\hat{v}$, integrating with respect to $\hat{v}$ and applying suitable moment-closure techniques (e.g., standard conservation laws or the method of Generalised Collision Invariants) gives rise to the mass and momentum balance equations.

Especially in the case of collective motion or alignment-based models, standard conservation laws might be insufficient and hence, e.g., mass but not momentum will be conserved by the collision operator Q, i.e., $\int_{\mathbb{R}^2} \hat{v}\, Q(f_0)\, \mathrm{d}\hat{v} \neq 0$. To overcome this, Degond and Motsch [49] introduced the concept of Generalised Collision Invariants (GCI), which we will employ in Section 2. By this concept, the classical notion of collision invariants is extended to be applied to particular models of collective dynamics.

To close this section, we state the macroscopic description of the Vicsek model.

The Vicsek model - continuum model. The formal derivation of the hydrodynamic limit and thus the large-scale system, often referred to as the Self-Organised Hydrodynamics (SOH) system, from the kinetic equations has been obtained via the method of the Generalised Collision Invariant by Degond and Motsch in [49]. The limit f_0 is given by $f_0 = \rho M_\Omega$ with $\rho(t, x) \geq 0$ and

$M_\Omega(\omega)$ being the according von Mises-Fisher distribution. We have that the particle density ρ is given by $\rho = \int_{\mathbb{S}^2} f_0(t,x,\omega)\,\mathrm{d}\omega$ as well as the mean orientation Ω by $\Omega(t,x) = {}^{J}/_{|J|}$ with $J = \int_{\mathbb{S}^2} \omega f_0(t,x,\omega)\,\mathrm{d}\omega$. Thus, the continuum model reads

$$\begin{aligned} \partial_t \rho + \nabla_x \cdot (c_1 \rho \Omega) &= 0, \\ \rho\left(\partial_t \Omega + c_2(\Omega \cdot \nabla_x)\Omega\right) + \lambda P_{\Omega^\perp} \nabla_x \rho &= 0, \end{aligned}$$

where c_1, c_2 and λ are constants determined in the course of the derivation. The first equation ensures mass conservation, and the flux term describes how the density ρ flows along the mean orientation Ω with constant speed c_1. The second equation expresses the evolution of the mean orientation Ω over time. The material derivative, i.e., the first two terms of the equation, describes the alignment process moving along the flow. The last term of the equation indicates the influence with intensity λ of the density gradient on the reorientation of the collective flow. Here, $P_{\Omega^\perp}$ again ensures that Ω stays on the unit sphere, that is $|\Omega| = 1$.
These macroscopic equations capture well the emergence of collective behaviour, such as the flocking of birds or schooling of fish, which arises from the interplay of the particles at the microscopic level. In Figure 1.2, we give a visual overview of the three different levels of description of the Vicsek model.

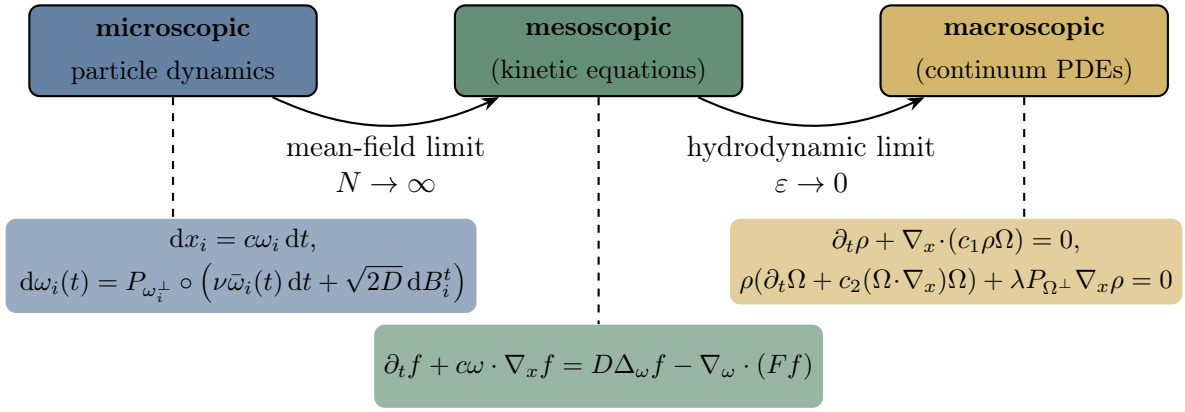

Figure 1.2: Illustration of the relation of the different levels of descriptions and their corresponding equations for the Vicsek model. The curved arrows indicate the mean-field limit ($N \to \infty$) and the hydrodynamic limit ($\varepsilon \to 0$), which link the levels and provide the mathematical tools for deriving the corresponding equations.

1.2 Outline and Contribution of the Thesis

A central challenge in the study of emergent phenomena is to construct models that both capture the essential features of the underlying microscopic dynamics and remain mathematically and computationally tractable at large scales. On the one hand, deriving mesoscopic and macroscopic equations from individual-based dynamics is not straightforward and often involves approximations whose appropriateness must be carefully assessed. On the other hand, efficient simulation of such models, particularly when involving complex network structures or non-linear interactions, poses significant numerical difficulties. This thesis addresses these challenges through three distinct projects. In Chapter 2, we model a system of particles that interact through volume exclusion interactions. Specifically, we study anisotropic particles interacting via a Gaussian-

type repulsive potential. We not only perform numerical simulations on this discrete system but also derive the corresponding mesoscopic and macroscopic equations formally. In Chapter 3, we consider a model for network formation, such as blood vessels or leaf venation, and propose a novel simulation strategy based on the fast Fourier transform (FFT) for solving the governing PDE. In Chapter 4, we revisit the kinetic model of fiber networks, based on the continuum model of Degond et al. [39], and provide a modified formal derivation that incorporates fiber repulsion to account for volume exclusion effects. Together, these projects advance the understanding of multiscale modelling by combining numerics, extensions of existing kinetic frameworks, and new derivations that connect microscopic rules to macroscopic behaviour. Hereinafter, we will provide a brief overview of each of these topics and state how they complement current research.

1.2.1 A Repulsive Potential Model to Account for Volume Exclusion Interactions

Volume exclusion interactions play a crucial role in a wide range of physical and biological systems and are essential to the emergence of collective behaviour such as swarming [103] and the spontaneous alignment of anisotropic particles [51], including, for example rice corns [88], liquid crystals [97] or certain types of cells [73]. Nevertheless, many models of collective dynamics forgo explicit volume exclusion interactions and instead prescribe alignment forces directly, see e.g., [45, 46, 49]. As a consequence, these models neglect the influence of volume exclusion interactions on particle positions and treat alignment as an imposed mechanism rather than an emergent effect.

In Chapter 2, we adopt a more direct approach. We investigate how a Gaussian-type repulsive potential, which encodes volume exclusion interactions at the microscopic level, affects not only the directional but also the spatial evolution of anisotropic particles across different modelling scales (from microscopic to macroscopic). This framework enables us to study alignment that naturally emerges from volume exclusion interactions, rather than as an externally prescribed rule. Our goal is to especially explore the influence of the repulsion potential on the particle density at the macroscopic level, since in classical models, the alignment potential affects only the orientations and does not modify the particle positions.

Because steric interactions, such as volume exclusion interactions, strongly depend on particle shape, we introduce a model for anisotropic particles whose geometry explicitly enters the interaction potential. In dimension two, the particles are represented as ellipses with ℓ and d defining the lengths of the major and minor axes, while in dimension three, we consider either oblate or prolate spheroids. A schematic illustration of the two-dimensional particle shape is shown in Figure 1.3.

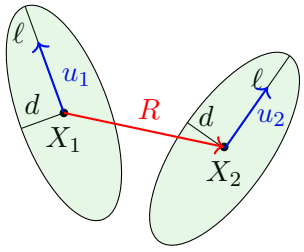

Figure 1.3: Two anisotropic particles (ellipses) with their centres X_1, X_2, the distance between the centres $R := X_2 - X_1$ and their directions given by the principal axes u_1, u_2 respectively.

We define the following first-order dynamics for N identical particles with centres $X_i \in \mathbb{R}^2$

and directions of their main axis $u \in \mathbb{S}^{n-1}$, where $\mathbb{S}^{n-1}$ is the $(n-1)$-dimensional unit sphere, for all $i \in \{1, \dots N\}$

$$\begin{aligned} \mathrm{d}X_i &= -\mu \frac{1}{N} \sum_{j=1}^{N} \nabla_{X_i} V(u_i, u_j, X_j - X_i)\, \mathrm{d}t + \sqrt{2D_x}\, \mathrm{d}B_i^t, \\ \mathrm{d}u_i &= -\lambda \frac{1}{N} \sum_{j=1}^{N} \nabla_{u_i} V(u_i, u_j, X_j - X_i)\, \mathrm{d}t + P_{u_i^\perp} \circ \sqrt{2D_u}\, \mathrm{d}\tilde{B}_i^t, \end{aligned} \tag{1.2.1a}$$

where ∇_{u_i} is the gradient on $\mathbb{S}^{n-1}$ and $P_{u_i}^\perp$ the orthonormal projection onto the orthonormal space to $u_i \in \mathbb{S}^{n-1}$. Note that equation (1.2.1a) must be understood in the Stratonovich sense, which is indicated by '$\circ$'. This guarantees that $u_i \in \mathbb{S}^{n-1}$ for all times within the existence interval of the solution. Moreover, the constants μ, λ, D_x, D_u are positive and $B_i^t, \tilde{B}_i^t$ are independent Brownian motions acting on the position and direction of particle $i \in 1, \dots N$. The weighted Gaussian repulsive potential V takes the form

$$V(u_1, u_2, R) := (4\pi)^{-n/2} \det(\Sigma)^{1/2} \exp\left(-R^T \Sigma^{-1} R\right),$$

with $\Sigma = \gamma_1 + \gamma_2$ and $\gamma_i = (\ell^2 - d^2) u_i \otimes u_i + d^2 \mathrm{Id}, i \in \{1, 2\}$. Here, $\ell > 0$ and $d > 0$ denote the length of the minor and major axes of a particle, Id is the $(n \times n)$-dimensional identity matrix, and $u \otimes u := (u_m u_k)_{m,k \in \{1,\dots,n\}}$. The repulsive potential V acts on the distance between two particles $X_j - X_i$ and their directions u_i, u_j.

We not only perform the mean-field limit $N \to \infty$ but also the hydrodynamic limit $\varepsilon \to 0$ of the system and analyse the emergent effects of the anisotropic repulsive potential on the particle density and the particles' mean direction. Not only at the macroscopic level, but also already in the kinetic equation, we can observe the effects of nematic alignment on the system arising from the weighted Gaussian potential. By applying the formalism presented in Section 1.1 for the coarse-graining process, in the simplest setup, we obtain the following complex system of macroscopic equations for the particle density $\rho = \rho(t, x)$ and the mean direction $\Omega = \Omega(t, x)$

$$\begin{aligned} &\partial_t \rho = D_x \Delta_x \rho + \mu \nabla_x \cdot (K(\eta(\rho)) \rho \nabla_x \rho), \\ &\partial_t \Omega + \mu \Pi_2(\rho)(\nabla_x \rho \cdot \nabla_x)\Omega + \mu \left(\frac{D_u}{\lambda} - \frac{D_x}{\mu} \right) P_{\Omega^\perp} \Delta_x \Omega = 0, \end{aligned} \tag{1.2.2a}$$

where K is the non-linear diffusion term for the density equation. Note that the equation for the particle density ρ does not depend on the mean direction Ω of the particles, but on their anisotropy via the factor K. The term $\eta = \eta(\rho)$ is a function given implicitly. The presence of K results in a slowdown of the non-linear diffusion for increasing anisotropy of the particles.

The key concept in deriving the evolution equation for Ω builds upon recent advancements in the field of Generalised Collision Invariants by Degond et al. [41]. We eventually obtain dynamics for the mean direction that involve complex transport and diffusion processes, which are also influenced by the particles' positions. Hence, the second term of equation (1.2.2a) represents the transport of Ω in the direction of $\nabla_x \rho$. Note that Π_2 arises from the anisotropic repulsive potential acting on the positions and would vanish if $\mu = 0$. Furthermore, the third term is the diffusion in the direction Ω. Note, that $P_{\Omega^\perp}$ ensures Ω to stay on the sphere. Moreover, we observe that in the case of $\mu = 0$, i.e., the repulsive potential is not acting on the positions at the discrete level, the diffusion of Ω only arises from the Brownian motion acting on the particles'

positions. Thus, $\mu D_u/\lambda$ establishes an anti-diffusion effect.

Alongside these analytical results, we additionally investigate the microscopic particle dynamics numerically. We not only obtain numerical boundaries for the non-linear diffusion constant K for the equation of ρ, but also investigate the effects of different interaction potentials (e.g., the normalised Gaussian potential or the Berne-Pechukas potential [19]) on the system. Furthermore, we study the influence of the anisotropy on the evolution of the particles' positions and directions, as well as how different values of the diffusion constants D_x and D_u affect the system.

A key conclusion that we draw from this chapter is that a purely anisotropic repulsive potential — motivated by volume exclusion interactions of elongated particles — can naturally lead to nematic alignment and a non-trivial spatial organisation of the particles influenced by the shape of the particles. In particular we observe that for two different particle shapes (oblate and prolate) different behaviour emerges and, interestingly, the well-posedness of the equation constraints the possible values of the parameters.

Future work of this project will include the investigation of other types of anisotropic repulsive potentials, e.g., the Lennard-Jones potential [82], as well as compactly supported volume exclusion potentials. Additionally, we will perform numerical experiments on the presented macroscopic system.

1.2.2 A Spectral-Based Method for Network-Formation PDEs

Understanding the formation and adaptation of biological transport networks is a fundamental problem in mathematical biology. Examples of such biological networks are leaf venation in plants [35, 85] or blood circulation in mammalians [94]. Since these networks are critical for the survival and functionality of living organisms, it is vitally important to gain an in-depth understanding of these networks. One approach to do so are mathematical models and their numerical simulations, and it still remains a challenge to accurately simulate the dynamics of such models describing network formation. Hence, Chapter 3 is dedicated to the numerical investigation of a continuum model for biological network formation in porous media, which has been explored in a series of papers (e.g., [2, 3, 9, 66, 67]) and is based on the discrete model for biological transport networks introduced by Hu and Cai [78]. The PDE model describes the evolution of the hydraulic conductivity $m = m(t, x, y) \in \mathbb{R}^2$ via an activation term, a reaction term, and a diffusive term. The parabolic equation for m is further constrained by an elliptic Poisson equation for the fluid pressure $p = p(t, x, y) \in \mathbb{R}$, which describes the local mass conservation. Hence, considering time $t \in [0, \infty)$ and the space variables $x, y \in \mathbb{R}$, the continuum model is given by the following system of equations

$$-\nabla \cdot [((m \otimes m) + r\mathrm{Id})\, \nabla p] = S, \tag{1.2.3}$$

$$\partial_t m - D^2 \Delta m - c^2 (m \cdot \nabla p) \nabla p + |m|^{2(\gamma-1)} m = 0. \tag{1.2.4}$$

Note, that we define the tensor product $\otimes$ as $m \otimes m := (m_i m_j)_{i,j\in\{1,2\}}$ and Id is the (2×2)-identity matrix. Moreover, $r(x, y) \geq r_0 > 0$ is the isotropic background permeability of the medium, $\gamma \in \mathbb{R}$ the exponent of the metabolic term, $D > 0$ the diffusive constant and $c > 0$ the activation parameter. Furthermore, the source and sinks in the medium are represented by $S = S(x, y)$. Compared to previous studies, we consider the system to be defined with periodic boundary conditions (before homogeneous Neumann and Dirichlet boundary conditions were

investigated) on a bounded rectangular domain $\Omega \in \mathbb{R}^2$ with smooth initial condition for m.

In Chapter 3 we propose a new numerical method for (1.2.3)-(1.2.4) that exploits the advantages of the fast Fourier transform (FFT) not only to solve the elliptic Poisson equation for p via the Conjugate Gradient (CG) method but also to compute the derivatives of m and p in the splitting method for the evolution equation of m. Note that in the right setting, the FFT is much faster compared to other methods with a reduced computational cost of just $\mathcal{O}(N \log N)$ for N grid points. In particular, compared to existing methods (mostly based on finite elements and implicit methods), this method is simple – it avoids the assembly/inversion of large sparse matrices –, delivers high accuracy, and is scalable to three dimensions, which is the dimension relevant for many applications, such as vascularisation.

To showcase our method, we illustrate its efficiency by capturing the characteristic branching and adaptation behaviour of the network. We recover previous results on the influence of the critical modelling parameters of the system: the diffusive constant D, the activation parameter c and the exponent of the metabolic cost term γ. Specifically, the experiments demonstrate that an increase in c enhances branching and increases the density of the network. Smoother and simpler networks result from larger D and smaller values of γ, which induce tree-like branching patterns. Additionally, we study the effects of different initial conditions for m as well as different setups for the source and sink term S, which lead to the evolution of diverse network morphologies.

Overall, the proposed numerical method successfully captures the complex dynamics of the investigated biological network formation model. Notably, the convergence results we provide in this work suggest a high order of convergence, attributed to the application of FFT. However, some challenges remain open: the method is not unconditionally energy-stable and retains a time step restriction due to stiffness, some of which could be improved with better preconditioners for the CG method or using an adaptive time step.

1.2.3 Derivation of a Kinetic Equation for a Fiber Network

Understanding the emergence and evolution of fiber networks in the extracellular matrix (ECM) is essential for explaining tissue mechanics and function, particularly in fibrous tissues such as adipose tissue, where fiber–cell interactions can shape tissue development [90]. Chapter 4 is dedicated to the formal derivation of the kinetic equation for a fiber network model introduced by Degond et al. in [39], in which fibers are considered to be built out of fiber unit elements of fixed length. The fiber elements are subject to a linking and unlinking process. By the linking process, longer fibers are created; by unlinking, longer fibers break down into smaller ones. The linking and unlinking process models the remodelling of the fiber network. Moreover, when fibers link, they tend to align – this models the fiber networks' resistance to bending. In a nutshell, the fiber network captures the following features: variation in length, branching off, breakage of fibers, resistance to bending and random movement in position and orientation of the fiber elements.

Importantly, the interactions among the fibers are not based on their relative distance but on an evolving network of links. This makes the mean-field limit difficult. Our goal is to recast the proof presented in [39], where the derivation is based on heuristic counting and conditional-probability arguments. In our proof, we aim to use solely empirical objects: the empirical fiber distribution and the empirical link measure. This viewpoint clarifies the structure of the limit and the assumptions needed to make it rigorous.

We will now briefly state the discrete system for the evolution of the fiber network. Let us consider N rod-like fiber elements of fixed length L characterised by their centres $X_i \in \mathbb{R}^2$ and orientations $\theta_i \in [-\pi, \pi)$ for all $i \in \{1, \dots N\}$, for a cartoon of the fibers see Figure 1.4. Then

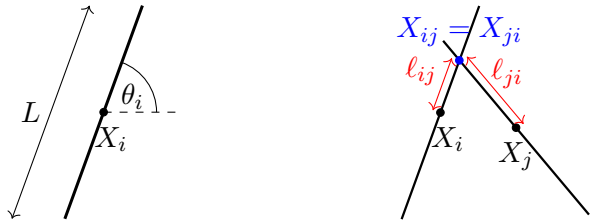

Figure 1.4: Left: a fiber unit element with centre X_i, orientation θ_i and length L. Right: Two linked fibers i, j with centres X_i, X_j, linking point $X_{ij} = X_{ji}$ and the distances from their centres to the linking point ℓ_{ij} and ℓ_{ji}.

the motion of the fibers is described by the second-order system of the following SDEs

$$\begin{aligned} \mathrm{d}X_i &= -\mu \nabla_{X_i} \left(W_{links} + W_{align} + W_{rep}\right) \mathrm{d}t + \sqrt{2D_x}\, \mathrm{d}B_i^t, \\ \mathrm{d}\theta_i &= -\lambda \partial_{\theta_i} \left(W_{links} + W_{align} + W_{rep}\right) \mathrm{d}t + \sqrt{2D_\theta}\, \mathrm{d}\tilde{B}_i^t. \end{aligned}$$

These dynamics correspond to a gradient flow that drives the system toward minimising the total potential energy given by the sum of W_{links}, W_{align}, W_{rep}. W_{links} corresponds to the linking force while W_{align} denotes the nematic alignment force between linked fibers and W_{rep} represents a repulsive potential. Moreover, the strength of the potentials is parameterised by the positive coefficients $\mu, \lambda > 0$. Furthermore, $(B_i^t)_{i=1,\dots,N}$ and $(\tilde{B}_i^t)_{i=1,\dots,N}$ denote independent Brownian motions and $D_x \geq 0$, $D_\theta \geq 0$ represent their diffusive constants.

In addition to this system of evolution equations for the fibers' position and orientation, we consider a linking and unlinking process, each given by a Poisson process with according linking and unlinking rates. The rate for link creation depends on the capability to form a link, i.e., the closeness, of two fibers.

We formally compute the mean-field limit for the deterministic part of the dynamics, based on the formalism presented in Section 1.1.2. Therefore, we obtain, considering the diffusions D_x and D_θ to be zero, i.e., $D_x = D_\theta = 0$, and a time interval during that no linking and unlinking of fibers takes place, for the fiber's probability density $f = f(t, x, \theta)$ and the linking measure $g = g(t, x, \theta_x, \ell_x, y, \theta_y, \ell_y)$ the following system of kinetic equations

$$\partial_t f - \nabla_x \cdot F_1 - \partial_\theta F_2 + \mu \nabla_x \cdot (\nabla_x \psi^R * f) + \lambda \partial_\theta (\partial_\theta \psi^R * f) = 0,$$

where '*' denotes a convolution and

$$\begin{aligned} \frac{dg}{dt} - \Big(\nabla_x \cdot \big(\frac{g}{f(t,x,\theta_x)} F_1(t,x,\theta_x)\big) + \mu \nabla_x \cdot \big(g(\nabla_x \psi^R * f)(t,x,\theta_x)\big) \\ + \nabla_y \cdot \big(\frac{g}{f(t,y,\theta_y)} F_1(t,y,\theta_y)\big) + \mu \nabla_y \cdot \big(g(\nabla_y \psi^R * f)(t,y,\theta_y)\big) \\ - \Big(\partial_{\theta_x} \big(\frac{g}{f(t,x,\theta_x)} F_2(t,x,\theta_x)\big) + \lambda \partial_{\theta_x} \cdot \big(g(\partial_{\theta_x} \psi^R * f)(t,x,\theta_x)\big) \\ + \partial_{\theta_y} \big(\frac{g}{f(t,y,\theta_y)} F_2(t,y,\theta_y)\big) + \lambda \partial_{\theta_y} \cdot \big(g(\partial_{\theta_y} \psi^R * f)(t,y,\theta_y)\big) = 0. \end{aligned}$$

We denote $g/f(x,\theta_x) = 0$ if $f(x, \theta_x) = 0$. Here, F_1 arises from the linking potential acting on the position and F_2 from the linking and alignment potentials acting on the orientations of the fibers. Moreover, ψ^R represents the repulsive potential. The linking measure $g = g(t, x, \theta_x, \ell_x, y, \theta_y, \ell_y)$

is proportional to the probability of finding a link between (x, θ_x, ℓ_x) and (y, θ_y, ℓ_y) at time t.

A key outcome of deriving the kinetic equation by solely employing the empirical fiber distribution and the empirical link measure is the clear identification of assumptions which are critical for the rigorous mean-field limit, such as the existence of a bijection between labels and fiber positions (heuristically supported by repulsion). In future work, we will investigate ways to establish a rigorous proof of this result and its connection to the theory of graphons.

1.3 Declaration of Authorship

Chapter 2 consists of joint work with Sara Merino Aceituno, Steffen Plunder, and Havva Yoldaş. It was published in Mathematical Models and Methods in Applied Sciences, Vol. 35, No. 10, pp. 2129-2179 (2025) [86]. Chapter 3 contains a manuscript in preparation for submission of results of ongoing collaboration with Pedro Aceves Sanchez, Pierre Degond and Sara Merino Aceituno. Finally, Chapter 4 states results of ongoing research with Sara Merino Aceituno. The material presented in all three sections is the result of discussions and exchanges of ideas with the respective co-authors.

2 Macroscopic Effects of an Anisotropic Gaussian-Type Repulsive Potential: Nematic Alignment and Spatial Effects

This chapter has been published as *Macroscopic effects of an anisotropic gaussian-type repulsive potential: Nematic alignment and spatial effects, S. Merino-Aceituno, S. Plunder, C. Wytrzens, H. Yoldaş, Mathematical Models and Methods in Applied Sciences, 35(10):2129–2179, 2025.* and is reprinted with permission from the publisher.

Contents

Abstract

Elongated particles in dense systems often exhibit alignment due to volume exclusion interactions, leading to packing configurations. Traditional models of collective dynamics typically

impose this alignment phenomenologically, neglecting the influence of volume exclusion on particle positions. In this paper, we derive nematic alignment from an anisotropic repulsive potential, focusing on a Gaussian-type potential and first-order dynamics for the particles. By analyzing larger particle systems and performing a hydrodynamic limit, we uncover the effects of anisotropy on both particle density and direction. Our findings reveal that while particle density evolves independently of direction, anisotropy slows down nonlinear diffusion. The direction dynamics are affected by the particles' position and involve complex transport and diffusion processes, with different behaviors for oblate and prolate particles. The key to obtaining these results lies in recent advancements in Generalized Collision Invariants offered by Degond, Frouvelle and Liu (KRM 2022) in [41].

2.1 Introduction

Volume exclusion interactions play a central role in many physical and biological systems. In particular, they are fundamental in explaining emergent patterns like swarming [103], and spontaneous alignment of anisotropic particles [51]. The latter is called *nematic alignment*. The term *nematic* indicates that the alignment takes place in a given direction (not necessarily in a given orientation): if u_1, $u_2 \in \mathbb{R}^n$ are such that $|u_1| = |u_2| = 1$, we say that the two vectors are *nematically* aligned if $u_1 = \pm u_2$. Nematic alignment is sometimes referred to as *apolar* alignment since it is in contrast to *polar* alignment which requires $u_1 = u_2$. Some examples of nematic alignment can be found in suspensions of rod-like particles in high-densities [17], and biological systems like myxobacteria [46].

2.1.1 Volume Exclusion and Nematic Alignment

Various volume exclusion models have been proposed to investigate cell dynamics, such as the vertex model [6, 58, 76] and other packing systems [40]. However, most agent-based models consider the agents as point-particles and impose phenomenological behavior that is assumed to be caused by volume exclusion interactions. Particularly, in most of these mathematical models for collective dynamics, the particle alignment is imposed via a force term without dealing with the contact interactions directly, see, e.g., [45, 46, 49].

Typical models for collective dynamics with nematic alignment take the following shape: agents move at a constant speed and try to align their direction of motion with one of their neighbors up to some noise. Specifically, we consider N agents who are identified by their positions $X_i \in \mathbb{R}^n$, $n \in \{2, 3\}$ and their directions $u_i \in \mathbb{S}^{n-1}$ on the $n-1$-dimensional sphere. Then their dynamics are governed by

$$\mathrm{d}X_i = v_0 u_i \,\mathrm{d}t, \tag{2.1.1a}$$

$$\mathrm{d}u_i = \frac{1}{N}\sum_{j=1}^{N} K(|X_i - X_j|)\nabla_{u_i} V_{\mathrm{nem}}(u_i, u_j)\,\mathrm{d}t + P_{u_i^\perp} \circ \sqrt{2D_u}\,\mathrm{d}B_i, \tag{2.1.1b}$$

$$V_{\mathrm{nem}}(u_i, u_j) := \lambda(u_i \cdot u_j)^2, \tag{2.1.1c}$$

where ∇_{u_i} is the gradient on the sphere, $V_{\mathrm{nem}}(u_i, u_j)$ is the potential producing nematic alignment, $P_{u_i^\perp}$ is the orthonormal projection onto the orthonormal space to $u_i \in \mathbb{S}^{n-1}$, and $(B_i)_{i=1,\dots,N}$ are independent Brownian motions for $i = 1, \dots, N$. The stochastic differential equation (2.1.1b) must be understood in the Stratonovich sense. This is indicated with the symbol '$\circ$' and it ensures that u_i remains on the sphere for all times where the solution is defined.

The constant v_0 in (2.1.1a) is the speed of the particles and $D_u > 0$ in (2.1.1b) is the diffusion constant of the directions. Moreover, the function $K \geq 0$ is an interaction kernel measuring the influence of the potential force depending on the distance between particles. The constant $\lambda > 0$ describes the strength of the alignment force, which is expressed as the gradient flow dynamics of the potential $V_{\text{nem}} = V_{\text{nem}}(u_i, u_j)$. One can easily check that, indeed, the maximizer of this potential corresponds to $u_i = \pm u_j$, i.e., when two particles are *nematically* aligned. In this regard, we say that the model (2.1.1a)-(2.1.1c) imposes alignment for the particles. We refer the reader to, e.g., [42, 45–47, 72, 89], for models that use this approach or a similar one.

In the present work, we follow a different approach. We do not wish to impose alignment directly, but to investigate how it might emerge naturally from volume exclusion interactions. In particular, we study how volume exclusion interactions affect *both* the directions and the positions of the particles.

However, deriving continuum equations from agent-based models that undergo contact interactions is mathematically extremely challenging, see, e.g., [25, 26]. This is why up-to-date there is no rigorous coarse-graining for excluded volume dynamics starting from the first principles. Even in the widely-studied Boltzmann equation, the derivation from discrete dynamics (a particle system undergoing elastic collisions) is still unknown for large times [21]. For this reason, contact interactions are often approximated by using soft interaction potentials, like repulsive potentials, that produce active forces when two agents get closer than a given distance [22,29,48].

In this article, we focus on a particular repulsive potential that is used for simulating the interactions of anisotropic particles: the Gaussian repulsive potential [19] for elliptic (dimension $n = 2$) or spheroidal (dimension $n = 3$) particles, see Figure 2.1. For related works in the biophysics literature see, e.g., [17, 18].

Our goal is to investigate for which shape of the Gaussian potential we obtain an alignment force for the continuum equation, and what is the effect of this force on the positions of the particles. The reason for the last point is that in classical models for nematic alignment, the potential only modifies the direction of motion of the agents, but not their positions. One can expect that, from interaction forces, agents may *push* each other modifying their positions. The question of interest here is what effect this *pushing* has on the positions of the particles.

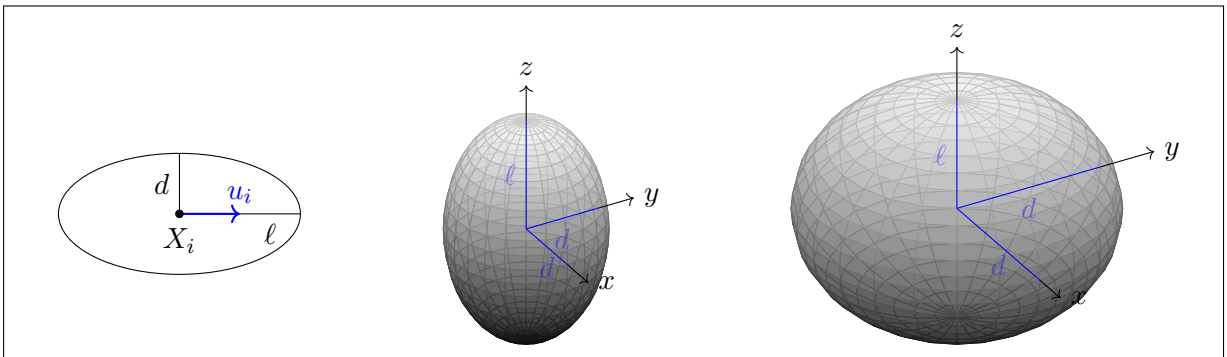

(a) Ellipse $d < \ell$ $(n = 2)$ (b) Prolate spheroid, $d < \ell$ $(n = 3)$ (c) Oblate spheroid, $d > \ell$ $(n = 3)$

Figure 2.1: Spheroids are obtained by rotating an ellipse, shown in (a), around one of its principal axes. If the revolution is around the major axis, the spheroid is called prolate (b); if it is around the minor axis, it is called oblate (c).

2.1.2 A Discrete Model for Anisotropic Particles

In this article, we study particles with either elliptic shape in the case of dimension $n = 2$ or spheroidal shape for dimension $n = 3$ (see Figure 2.1). In both cases, the particles are identical and are identified by their center $X \in \mathbb{R}^n$, the direction of one of the axes specified by a unit vector $u \in \mathbb{S}^{n-1}$, and the lengths of the major and minor axes. In dimension $n = 2$, u denotes the direction of the major axis whose length is $\ell \geq 0$ and the length of the minor axis is denoted by $d \geq 0$. In dimension $n = 2$, the *main axis* is the principal axis, i.e., the axis with longer length; whereas in dimension $n = 3$, the main axis is the axis of rotation.

We define the constant χ to characterize the shape of ellipses and spheroids,

$$\chi := \frac{\ell^2 - d^2}{\ell^2 + d^2}, \tag{2.1.2}$$

which measures the anisotropy of particles. In dimension $n = 2$, we have that $\chi \in [0, 1]$. In this case, $\chi = 0$ and $\chi = 1$ correspond to circular and rod-shaped particles, respectively. In dimension $n = 3$, we have $\chi \in [-1, 1]$. In this case, the negative values of χ correspond to oblate particles (rotation around the minor axis), and the positive values of χ correspond to prolate particles (rotation around the major axis); see Figure 2.1. In particular, $\chi = 0$ corresponds to spheres; $\chi = -1$ to infinitely flat disks; and $\chi = 1$ to infinitely thin rods.

We consider N identical particles identified by their centers $X_i \in \mathbb{R}^n$ and the direction of their main axes $u_i \in \mathbb{S}^{n-1}$ (notice that this is not uniquely defined as u_i and $-u_i$ prescribe the same direction) for $i = 1, \dots, N$. Two particles (X_i, u_i), (X_j, u_j) are said to be (nematically) aligned when $u_i = \pm u_j$. For simplicity, here we consider only inert particles, i.e, $v_0 = 0$. However, this could be easily extended.

We assume that the repulsive potential V_b acts on the distance between the centers of two particles $X_j - X_i$ and the directions of their main axes u_i, u_j, i.e., $V_b(u_i, u_j, X_j - X_i)$. The model follows the steepest gradient descent of the potential V_b together with some noise both in the positions of the centers and in the directions of the main axes and it is given by

$$\mathrm{d}X_i = -\mu \frac{1}{N} \sum_{j=1}^{N} \nabla_{X_i} V_b(u_i, u_j, X_j - X_i)\, \mathrm{d}t + \sqrt{2D_x}\, \mathrm{d}B_i, \tag{2.1.3a}$$

$$\mathrm{d}u_i = -\lambda \frac{1}{N} \sum_{j=1}^{N} \nabla_{u_i} V_b(u_i, u_j, X_j - X_i)\, \mathrm{d}t + P_{u_i^\perp} \circ \sqrt{2D_u}\, \mathrm{d}\tilde{B}_i, \tag{2.1.3b}$$

where ∇_{u_i} and $P_{u_i^\perp}$ are the same as before, $B_i, \tilde{B}_i$ are independent Brownian motions for $i = 1, \dots, N$; and μ, λ, D_x, D_u are positive constants. The potential V_b corresponds to an anisotropic repulsive potential. In [24], the authors propose a model to describe the motion of spheroidal particles that are suspended in an incompressible fluid. The system (2.1.3a)-(2.1.3b) can be seen as the overdamped regime for these equations when there is no fluid.

In particular, notice that the potential V_b acts also on the distance between the centers of the particles. This effect does not appear in the classical nematic-alignment model (2.1.1a)-(2.1.1c). Our goal is to investigate how this potential affects the mean-nematic direction and the positions of the particles. To carry this out, we derive a kinetic equation (see Section 2.1.3) for system (2.1.3a)-(2.1.3b) as a first step and subsequently we obtain continuum equations from the kinetic equation (see Section 2.2).

Let us have a closer look at the interaction potential. We describe the binary interactions between identical particles (ellipses for $n = 2$, or spheroids for $n = 3$, see Figures 2.1 and 2.2)

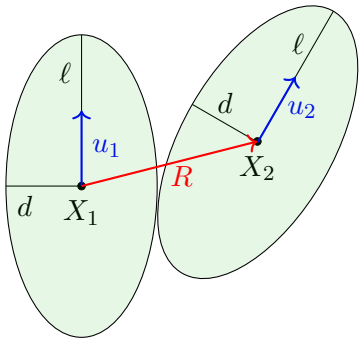

Figure 2.2: Two ellipses with their centers X_1, X_2, the distance between the centers R and their principal axes u_1, u_2 respectively.

via an anisotropic Gaussian-type potential V_b of the form

$$V_b(u_1, u_2, R) = (4\pi)^{-n/2} b(u_1, u_2) \exp\left(-R^T \Sigma^{-1} R\right), \tag{2.1.4}$$

where $b(u_1, u_2) \geq 0$ is a scaling factor, $R = X_2 - X_1$ is the vector between the centers of two particles, and the over index 'T' denotes the vector transpose. The matrix Σ is given by

$$\Sigma = \gamma_1 + \gamma_2,$$

where

$$\gamma_i = (\ell^2 - d^2) u_i \otimes u_i + d^2 \mathrm{Id}, \qquad i \in \{1, 2\}.$$

Our particular choice of the scaling factor b is given by

$$b_{\mathrm{WG}}(u_1, u_2) := \left(1 - \chi^2 (u_1 \cdot u_2)^2\right)^{1/2} = \det(\Sigma)^{1/2}. \tag{2.1.5}$$

Using the scaling factor (2.1.5), the weighted Gaussian potential (2.1.4) takes the following form:

$$V_{b_{\mathrm{WG}}}(u_1, u_2, R) := (4\pi)^{-n/2} \det(\Sigma)^{1/2} \exp\left(-R^T \Sigma^{-1} R\right). \tag{2.1.6}$$

We dedicate Section 2.3.1 to a detailed explanation of repulsive potentials and some numerical simulations to show their effect on the dynamics of interacting particles. This section also includes a more detailed motivation for our particular choice of the scaling factor (2.1.5). Before we explain the kinetic equation arising from the particle dynamics, we make the following remark:

Remark 2.1.1. *In [19], Berne and Pechukas considered the potential U for a single spheroid with its center x and direction of its main axis u:*

$$U(x) := \exp(-x^T \gamma^{-1} x),$$

where $\gamma = (\ell^2 - d^2) u \otimes u + d^2 Id$. Using the potential $U = U(x)$, they introduced the anisotropic Gaussian-type potential (2.1.4) *to describe the binary repulsive interactions. The level sets where U is constant correspond to ellipsoids of revolution about the axis u, i.e., spheroids concentric to the original (x, u)-spheroid, and they remain so even if the potential U is multiplied by a factor that could potentially depend on u. For this reason, introducing the scaling factor $b = b(u_1, u_2)$ does not change the intrinsic properties of the potential. On the other hand, this offers some simplifications for mathematical analysis, see Section 2.3.1 for more details.*

2.1.3 Kinetic Equation and Macroscopic Quantities

In this section, we write the mean-field equation (or large-particle limit) of the particle system (2.1.3a)-(2.1.3b). We consider a system of $N \geq 0$ identical particles in $\mathbb{R}^n$ for $n \in \{2, 3\}$, identified by the positions of their centers and the directions of their main axes $(X_i, u_i)_{i=1,\dots,N}$ that follow the dynamics given by the system (2.1.3a) -(2.1.3b). As $N \to \infty$, the particle system is described by the probability distribution function $f = f(t, x, u)$ of particles at position x with the main axis in direction u at time t. Obtaining the equation for f, at least formally, uses standard tools from kinetic theory, which we will not detail here but refer the reader to, e.g., [100].

We start with defining an empirical measure f^N of the particles given by

$$f^N(t, x, u) = \frac{1}{N} \sum_{i=1}^{N} \delta_{(X_i(t), u_i(t))}(x, u), \tag{2.1.7}$$

where $\delta_{(X_i(t),u_i(t))}(x, u)$ is the Dirac delta distribution at $(X_i(t), u_i(t))$. The formal mean-field limit of the kinetic equation for the empirical distribution under the assumption that $f^N \to f$ as $N \to \infty$ solves

$$\partial_t f - \mu \nabla_x \cdot ((\nabla_x V_f)\, f) - \lambda \nabla_u \cdot ((\nabla_u V_f)\, f) - D_x \Delta_x f - D_u \Delta_u f = 0, \tag{2.1.8}$$

where

$$V_f(t, x_1, u_1) := \int_{\mathbb{S}^{n-1}} \int_{\mathbb{R}^n} V_b(u_1, u_2, x_2 - x_1) f(t, x_2, u_2)\, \mathrm{d}x_2\, \mathrm{d}u_2.$$

Next, we define the macroscopic quantities associated to $f = f(t, x, u)$, namely the spatial (or mass) density of the particles $\rho_f(t, x)$ and the mean-nematic direction $\Omega_f(t, x)$ at time $t \geq 0$ at position $x \in \mathbb{R}^n$. Our goal is to derive equations for $\rho_f(t, x)$ and $\Omega_f(t, x)$ from $f = f(t, x, u)$.

The mass density $\rho_f(t, x)$ is defined by

$$\rho_f(t, x) := \int_{\mathbb{S}^{n-1}} f(t, x, u)\, \mathrm{d}u.$$

To define $\Omega_f(t, x)$, we need to consider the following:

$$(\rho_f Q_f)(t, x) := \int_{\mathbb{S}^{n-1}} \left(u_2 \otimes u_2 - \frac{1}{n} \mathrm{Id} \right) f(t, x, u_2)\, \mathrm{d}u_2. \tag{2.1.9}$$

where $Q_f(t, x)$ is a matrix associated to the distribution $f = f(t, x, u)$ and it is called *Q-tensor* in the literature of liquid crystals see, e.g., [11, 101]. Note that Q_f is a symmetric, trace-free matrix satisfying $Q_f \geq -\frac{1}{n}\mathrm{Id}$.

The principal eigenvector of $Q_f(t, x)$ gives the direction that corresponds to the mean-nematic direction of the particles located at $x \in \mathbb{R}^n$ at time $t \geq 0$ (see, e.g., page 15 of [43] for an explanation). We denote the principal eigenvector by $\Omega_f(t, x) \in \mathbb{S}^{n-1}$ as long as it is unique (up to a change of sign). We have, in particular, that $\Omega_f = \Omega_f(t, x)$ maximizes over $\mathbb{S}^{n-1}$ the quantity (see page 37 of [43]),

$$u \mapsto u \cdot (\rho_f Q_f) u = \int_{\mathbb{S}^{n-1}} \left((u \cdot u_2)^2 - \frac{1}{n} \right) f(t, x, u_2)\, \mathrm{d}u_2.$$

This can also be seen as a consequence of the Courant-Fisher theorem, or the min-max theorem, see, e.g., [98]. Indeed, notice that if $f = f^N$ is the empirical measure (2.1.7), the previous expression implies that Ω_f maximizes

$$u \mapsto \frac{1}{N}\sum_{j=1}^{N}(u \cdot u_j)^2,$$

which is analogous to maximizing

$$\frac{1}{N}\sum_{j=1}^{N} V_{\mathrm{nem}}(u, u_j),$$

where V_{nem} is the potential given in Equation (2.1.1c). Thus, Ω_f defined in this way is indeed the mean-nematic direction.

In this article, we derive equations for the spatial density $\rho = \rho_f(t,x)$ of particles and their mean-nematic direction $\Omega = \Omega_f(t,x)$. Before delving into the details in the next section, we end this introductory part with some comments on the continuum equations. For the density ρ, we obtain an equation of the form

$$\partial_t \rho = D_x \Delta_x \rho + \mu \nabla_x \cdot (K(\rho)\rho \nabla_x \rho)\,,$$

where K is a functional that depends on ρ. Notice that the particle density does not depend on the mean-nematic direction Ω. However, the effect of the repulsive potential is present through the functional K, which depends, particularly, on the anisotropy parameter χ^2 (defined in (2.1.2)).

The equation for Ω is a combination of transport and diffusion, with a cross-diffusion term in ρ. Intriguingly, the well-posedness of the equation imposes a constraint on the parameters. Particularly, we require that

$$\frac{D_x}{\mu} > \frac{D_u}{\lambda}. \tag{2.1.10}$$

However, this constraint is not required at the particle level. We discuss in detail possible explanations for this constraint in Section 2.2.3. Our main result is given in Theorem 2.2.10 and its interpretation is given in Section 2.2.3.

Structure of the paper. In Section 2.2, we state our main result, Theorem 2.2.10, after some preliminary definitions and results. Theorem 2.2.10 is followed by an extensive interpretation section, Section 2.2.3, where we comment on each component of our continuum equations. In Section 2.3.1, we motivate our choice of the Gaussian-type repulsive potential (2.1.6) by comparing it with similar interaction potentials used in the literature. Section 2.3.2 is dedicated to numerical simulations of the stochastic particle system (2.1.3a)-(2.1.3b). Here, we conduct a detailed parameter study and a numerical comparison of the effect of different repulsive potentials on the global alignment of the particles. We dedicate Section 2.4 to the proof of Theorem 2.2.10. Finally, the paper is complemented with some concluding remarks and perspectives in Section 2.5, followed by appendices.

2.2 Continuum Equations

In this section, we derive continuum equations, namely the equations for the mass density $\rho_f(t,x)$ and the mean-nematic direction $\Omega_f(t,x)$ from the kinetic equation (2.1.8). We start with non-dimensionalizing the kinetic equation (2.1.8). To this end, we introduce a scaling parameter $0<\varepsilon\ll 1$ and denote by f^ε the solution of the scaled kinetic equation.

Non-dimensionalization. Introducing the units of space x_0 and time t_0, we define the dimensionless variables,

$$\tilde{x}=\frac{x}{x_0},\quad \tilde{t}=\frac{t}{t_0},\quad \tilde{f}=fx_0^n,$$

and the dimensionless parameters,

$$\tilde{\mu}=\mu\frac{t_0}{x_0^2},\quad \tilde{\lambda}=t_0\lambda,\quad \tilde{D}_u=t_0D_u,\quad \tilde{D}_x=\frac{D_xt_0}{x_0^2},\quad \tilde{\ell}=\frac{\ell}{x_0},\quad \tilde{d}=\frac{d}{x_0}.$$

We remark that the anisotropy factor χ and the potential V_b are already dimensionless. Thus, we have

$$\tilde{\chi}=\chi,\quad \tilde{V_b}=V_b,\quad \tilde{V_f}=V_f.$$

Using these dimensionless quantities, dropping the tildes for the sake of simplicity, we obtain exactly the same equation as before, i.e., we end up with Equation (2.1.8). But now all the variables and parameters are without units.

Scaling. Considering a scaling parameter $0<\varepsilon\ll 1$, we introduce the primed variables below,

$$\ell=\varepsilon\ell',\quad d=\varepsilon d',\quad \mu=\varepsilon^{-n}\mu',\quad \lambda=\varepsilon^{-(n+a)}\lambda',\quad D_u=\varepsilon^{-a}D_u',$$

where $a\in(0,2]$ is a constant. Notice that the scaling in ℓ and d combined with the scaling of the potential by $\varepsilon^nV_f^\varepsilon=V_f$ produces a localization in space of the potential V_f (for details, see Lemma 2.2.1). The choice of a has an influence on the resulting macroscopic equation (see Remark 2.2.1). Notice also that the diffusion constant D_x stays of order 1. We obtain the following rescaled kinetic equation (skipping the primes for simplicity):

$$\partial_tf^\varepsilon-\mu\nabla_x\cdot((\nabla_xV_{f^\varepsilon}^\varepsilon)f^\varepsilon)-D_x\Delta_xf^\varepsilon=\frac{1}{\varepsilon^a}\left(\lambda\nabla_u\cdot((\nabla_uV_{f^\varepsilon}^\varepsilon)f^\varepsilon)+D_u\Delta_uf^\varepsilon\right).$$

Next, we further expand the potential V_f.

Lemma 2.2.1 (Expansion of the potential)**.** *Considering $\ell=\varepsilon\ell'$ and $d=\varepsilon d'$ we have the following expansion V_f^ε of the scaled weighted Gaussian potential V_f (defined by using* (2.1.6)*):*

$$\begin{aligned}V_f^\varepsilon(t,x_1,u_1):=&\frac{1}{\varepsilon^n}V_f(t,x_1,u_1)\\&=\int_{\mathbb{S}^{n-1}}\left(1-\chi^2(u_1\cdot u_2)^2\right)f(t,x_1,u_2)\,\mathrm{d}u_2\\&\quad+\frac{\varepsilon^2}{4}\int_{\mathbb{S}^{n-1}}\left(1-\chi^2(u_1\cdot u_2)^2\right)\Sigma(u_1,u_2):\mathrm{D}_x^2f(t,x_1,u_2)\,\mathrm{d}u_2+\mathcal{O}(\varepsilon^3)\\&=W_f(t,x_1,u_1)+\varepsilon^2B_f(t,x_1,u_1)+\mathcal{O}(\varepsilon^3),\end{aligned}\tag{2.2.1}$$

where D_x^2 *is the Hessian, i.e., a* $n\times n$*-matrix with components* $(\mathrm{D}_x^2)_{ij} = \partial_{x_i}\partial_{x_j}$*, ':' denotes the double contraction, i.e.,* $A : B := \sum_{i,j} A_{ij}B_{ij}$*,* W_f *and* B_f *are defined as*

$$W_f(t,x_1,u_1) := \int_{\mathbb{S}^{n-1}} \left(1-\chi^2(u_1\cdot u_2)^2\right) f(t,x_1,u_2)\,\mathrm{d}u_2, \tag{2.2.2}$$

$$B_f(t,x_1,u_1) := \frac{1}{4}\int_{\mathbb{S}^{n-1}} \left(1-\chi^2(u_1\cdot u_2)^2\right) \Sigma(u_1,u_2) : \mathrm{D}_x^2 f(t,x_1,u_2)\,\mathrm{d}u_2. \tag{2.2.3}$$

Proof. The proof can be found in Appendix 2.6.1. ∎

Nematic alignment potentials analogous to W_f appear in the literature of collective dynamics, e.g., in a model for nematic alignment of fibers [39], in a model for body attitude coordination [43], and in a model of pure nematic alignment [47].

Finally, using the expansion for the scaled weighted Gaussian potential V_f^ε in Lemma 2.2.1 we obtain:

$$\partial_t f^\varepsilon - \mu\nabla_x\cdot((\nabla_x W_{f^\varepsilon})f^\varepsilon) - D_x\Delta_x f^\varepsilon - \varepsilon^{2-a}\lambda\nabla_u\cdot((\nabla_u B_{f^\varepsilon})f^\varepsilon) = \frac{D_u}{\varepsilon^a}C(f^\varepsilon) + \mathcal{O}(\min(\varepsilon^2,\varepsilon^{3-a})), \tag{2.2.4}$$

with $a\in(0,2]$ and where

$$C(f) := \frac{\lambda}{D_u}\nabla_u\cdot((\nabla_u W_f)f) + \Delta_u f.$$

Remark 2.2.1 (Motivation for the scaling factor a)**.** *The scaled kinetic equation with* $a=2$ *can also be equivalently obtained by just scaling space and time by* $x' = \sqrt{\varepsilon}x$ *and* $t' = \varepsilon t$*, which is a more natural scaling choice. However, we also consider an alternative scaling where the term* B_f *vanishes in the macroscopic limit. The term* B_f *is specific to the Gaussian repulsive potential, and it acts as a correction to the primary nematic alignment potential* W_f*. As we will see, the term* B_f *is unique in the sense that it gives different behavior for prolate and oblate particles (see term* Π_3 *in the macroscopic limit* (2.2.21)*). In the specific case where* $a\in(0,2)$*, the term* B_f *disappears in the limit. The two scaling factors that we consider highlight the differences in the dynamics with and without the term* B_f*. Thus,* $a=2$ *can be viewed as a diffusive scaling, while* $a\in(0,2)$ *represents a generalized scaling law distinct from hyperbolic scaling.*

Our goal is to derive equations for the time evolution of the mass density $\rho_f = \rho_f(t,x)$ and the mean-nematic direction $\Omega_f = \Omega_f(t,x)$. For this reason, we rewrite the kinetic equation in terms of the Q-tensor Q_f. First, using that $(u\cdot v)^2 = u^T(v\otimes v)u$ and that $\rho_f = \int_{\mathbb{S}^{n-1}} f\,\mathrm{d}u$, we rewrite W_f in (2.2.2) as follows:

$$W_f(t,x_1,u_1) = -\chi^2 u_1^T(\rho_f Q_f)u_1 - \left(\frac{\chi^2}{n}-1\right)\rho_f. \tag{2.2.5}$$

With this new expression for W_f and using that $\nabla_u\rho_f = 0$, the kinetic equation (2.2.4) becomes

$$\begin{aligned}\partial_t f^\varepsilon + \mu\chi^2\nabla_x\cdot(\nabla_x(\,u^T(\rho_{f^\varepsilon}Q_{f^\varepsilon})u\,)f^\varepsilon) + \mu\left(\frac{\chi^2}{n}-1\right)\nabla_x\cdot((\nabla_x\rho_{f^\varepsilon})f^\varepsilon)\\ - \lambda\varepsilon^{2-a}\nabla_u\cdot((\nabla_u B_f)f^\varepsilon) - D_x\Delta_x f^\varepsilon = \frac{D_u}{\varepsilon^a}C(f^\varepsilon) + \mathcal{O}(\min(\varepsilon^2,\varepsilon^{3-a})),\end{aligned} \tag{2.2.6}$$

where

$$C(f) = \nabla_u \cdot \left(\nabla_u f - \frac{\lambda}{D_u} f \nabla_u \left(\chi^2 u^T (\rho_f Q_f) u \right) \right). \tag{2.2.7}$$

In the next section, we give some preliminary definitions and concepts to analyze the operator C in detail.

2.2.1 Properties of the Operator C

From Equation (2.2.6), we can already observe that, at least formally, if f^ε converges to some function f^0 as $\varepsilon \to 0$, then it must hold that f^0 belongs to the kernel of the operator C, i.e., $C(f_0) = 0$. Fortunately, the equilibria for C have already been studied in [41] and in this section we summarize the results presented there. Therefore, this section mainly follows some results of [41] omitting their proofs.

In particular, we are interested in stable equilibria of the operator C (for an exact notion of stability see [41]). The key result, containing the characterization of the stable equilibria of C, is given in Lemma 2.2.7, which can be found at the end of this section.

Remark 2.2.2. *The operator C defined in* (2.2.7) *is equivalent to the one presented in Equation (39) in [41] for*

$$\alpha := \frac{\chi^2 \lambda}{D_u}. \tag{2.2.8}$$

Next, we introduce some preliminaries.

Definition 2.2.2 (Uniaxial tensor)**.** Given $\Omega \in \mathbb{S}^{n-1}$, the normalized, uniaxial, trace-free tensor A_Ω in the direction of Ω is defined by

$$A_\Omega = \Omega \otimes \Omega - \frac{1}{n} \mathrm{Id}. \tag{2.2.9}$$

The tensor A_Ω is symmetric with principal eigenvalue $\frac{n-1}{n}$. It is called *uniaxial* since it has only two eigenvalues and one of them is simple. The normalized eigenvectors associated to the simple eigenvalue are $\pm\Omega$.

Next, we define the Gibbs distributions of uniaxial tensors.

Definition 2.2.3 (Gibbs distribution of an uniaxial tensor)**.** Given $\eta > 0$ and the tensor A_Ω, the Gibbs distribution $G_{\eta A_\Omega}$ associated to ηA_Ω is defined as

$$G_{\eta A_\Omega}(u) = \frac{1}{Z_\eta} e^{\eta (u \cdot \Omega)^2}, \quad \text{where} \quad Z_\eta = \int_{\mathbb{S}^{n-1}} e^{\eta (u \cdot \Omega)^2} \, \mathrm{d}u. \tag{2.2.10}$$

Finally, the order parameter associated to a Gibbs distribution is defined as follows.

Definition 2.2.4 (Order parameter)**.** The order parameter associated to $G_{\eta A_\Omega}$ is denoted by $S_2 = S_2(\eta)$ and given by

$$S_2(\eta) := \frac{n}{n-1} \Omega^T Q_{G_{\eta A_\Omega}} \Omega = \frac{n}{n-1} \int_{\mathbb{S}^{n-1}} \left((u \cdot \Omega)^2 - \frac{1}{n} \right) G_{\eta A_\Omega} \, \mathrm{d}u, \tag{2.2.11}$$

where $Q_{G_{\eta A_\Omega}}$ is the Q-tensor associated to $G_{\eta A_\Omega}$.

Remark 2.2.3. *Using the change of variables* (2.4.1)*, the order parameter* $S_2(\eta)$ *can be written as*

$$S_2(\eta) = \frac{n}{n-1}\int_0^\pi \left(\cos^2\theta - \frac{1}{n}\right) g_\eta(\theta)\sin^{n-2}\theta\,\mathrm{d}\theta. \tag{2.2.12}$$

where the function g_η *is given in* (2.4.2)*.*

Notice that $S_2(\eta)$ is actually independent of Ω and it satisfies the following:

Lemma 2.2.5 (Proposition 2 in [41])**.** *It holds that*

$$Q_{G_{\eta A_\Omega}} = S_2(\eta)A_\Omega.$$

Moreover, $S_2 : (0,\infty) \to (0,1)$ *is non-decreasing with* $S_2 \to 0$ *as* $\eta \to 0$ *and* $S_2 \to 1$ *as* $\eta \to \infty$*.*

Next, we define the function $\eta = \eta(\rho)$ implicitly through the following equation:

Proposition 2.2.6 (Implicit definition of $\eta = \eta(\rho)$, Proposition 3 in [41])**.** *The equation*

$$\frac{\eta}{\alpha\rho} = S_2(\eta) \tag{2.2.13}$$

has at least a root η *if and only if* $\rho \in (\rho_*, +\infty)$*,* $\rho_* > 0$*. Moreover,* (2.2.13) *has at most two roots. Choosing the largest root, we can define a smooth, non-decreasing function* $(\rho_*, +\infty) \to (\eta^*, +\infty)$*,*
$\rho \mapsto \eta(\rho)$*, where* $\eta^* = \lim_{\rho\to\rho_*}\eta(\rho) \geq 0$*.*

Finally, with all the definitions above, we can state the main result regarding the equilibria of C:

Lemma 2.2.7 (Stable equilibria of C, Lemma 4.4 in [41])**.** *Let* $n \in \{2,3\}$*. For* ρ_* *given in Proposition 2.2.6 the following holds:*

(i). If $\rho < \rho_*$*, then* $f = \rho$ *(the uniform equilibrium) is the only stable equilibrium of the operator* C*.*

(ii). If $\rho > \rho_*$*, then the only stable equilibria of the operator* C *are of the form*

$$f = \rho G_{\eta(\rho)A_\Omega}.$$

In particular, we have

$$Q_f = S_2(\eta(\rho))A_\Omega, \tag{2.2.14}$$

where S_2 *and* $\eta = \eta(\rho)$ *are defined in* (2.2.11) *and* (2.2.13) *respectively. Equation* (2.2.14) *is referred to as* "consistency relation" *and can be written, using* (2.2.13)*, equivalently as*

$$\alpha\rho Q_{G_{\eta(\rho)A_\Omega}} = \eta(\rho)A_\Omega. \tag{2.2.15}$$

Remark 2.2.4. *The operator* C *is analogous to the operator that appears for models of nematic alignment where the nematic alignment is imposed, see, e.g., [47]. However, in [47] the potential*

is written in a so-called, 'mean-field force' form rather than a binary force. Here, we have the term

$$\varphi_1(u) := u^T \rho_f Q_f u = \int_{\mathbb{S}^{n-1}} \left((u \cdot u_2)^2 - \frac{1}{n} \right) f(t, x, u_2) \, \mathrm{d}u_2,$$

while in [47] this operator is replaced by

$$\varphi_2(u) := u^T A_{\Omega_f} u = (u \cdot \Omega_f)^2 - \frac{1}{n},$$

where Ω_f corresponds to the mean-nematic direction (that is why it is called 'mean-field force'). We expect that both cases lead to nematic alignment. Already in the case φ_2 we see that $u = \pm\Omega_f$ is the maximizer. In the first case, we also know that Ω_f corresponds to the principal eigenvector of Q_f, gives the mean-nematic direction and maximizes φ_1. However, it is not guaranteed that the principal eigenvalue has only multiplicity 1. This adds an extra degree of difficulty to the analysis. Lemma 2.2.7 demonstrates that this leads to phase transitions in the macroscopic limit, with spatial regions of disordered dynamics, i.e., the dynamics where a well-defined principal eigenvector does not exist, and thus, particles do not align. This takes place in the regions of low density, i.e., $\rho < \rho_*$.

Remark 2.2.5. *Given the matrix Q_f, suppose that $\Omega_f \in \mathbb{S}^{n-1}$ is the principal eigenvector (assumed to be unique up to a change in sign). Then, it holds that A_{Ω_f} also has a principal eigenvector Ω_f. So, both Q_f and A_{Ω_f} give the same mean-nematic direction. However, $Q_f \neq A_{\Omega_f}$ in general. In particular, the principal eigenvalue of A_{Ω_f} is always $\frac{n-1}{n}$, while for Q_f the eigenvalues have $\frac{n-1}{n}$ as an upper bound (see [47]). In particular (see [41]), to measure the degree of nematic alignment one considers the following order parameter γ_f:*

$$\gamma_f = \frac{n}{n-1} \beta_f \in (0, 1], \tag{2.2.16}$$

where β_f is the largest eigenvalue of Q_f. If f is uniformly distributed on the sphere (particles are fully misaligned), then γ_f is close to 0. On the contrary, if f is close to $\frac{1}{2}(\delta_\Omega + \delta_{-\Omega})$, i.e., particles are fully aligned and $Q_f = A_{\Omega_f}$, then $\gamma_f = 1$. So the case $Q_f = A_{\Omega_f}$ is an extreme case that corresponds to having all particles nematically aligned in the direction Ω_f.

In fact, the function $S_2 = S_2(\eta)$ is the order parameter of $G_{\eta A_\Omega}$.

Remark 2.2.6. *As $\eta \to 0$, $G_{\eta A_\Omega}$ converges to the uniform probability distribution on $\mathbb{S}^{n-1}$ and S_2 converges to 0. As $\eta \to \infty$, $G_{\eta A_\Omega}$ converges to two Dirac delta distributions $\frac{1}{2}(\delta_\Omega + \delta_{-\Omega})$ which accounts for fully aligned distribution in the direction of Ω and thus also S_2 converges to 1. Therefore, as η increases, S_2 increases too (see also Figure 2.10b), and $G_{\eta A_\Omega}$ shows increasing order of alignment.*

Now, we are ready to state our main result in the next section.

2.2.2 The Macroscopic Limit

Assumption 2.2.8. *We assume throughout that all the functions are as smooth as needed so that all the limits exist and the convergences are as strong as needed.*

Next, we introduce the following definition which we will use in the theorem below.

Definition 2.2.9. Let A be a 5-tensor and B a 4-tensor in $\mathbb{R}^n$, then we define the following operation between tensors:

$$([A:B]_{[2,3,4,5:1,2,3,4]})_p := \sum_{j,k,l,m=1}^{n} A_{pjklm}B_{jklm}, \quad p=1,\dots,n,$$

The contraction with the subscript $[2,3:1,2]$ is analogously defined.

We give our main result in the following theorem:

Theorem 2.2.10. *Let $n \in \{2,3\}$, $a \in (0,2]$, and $f^\varepsilon = f^\varepsilon(t,x,u)$ be the solution to the kinetic equation (2.2.6). Suppose that Assumption 2.2.8 holds and that $f^\varepsilon(t,x,u) \to f^0(t,x,u)$ as $\varepsilon \to 0$. Consider (t,x) such that $\int_{\mathbb{S}^{n-1}} f^0 du > \rho_*$ (where ρ_* is given in Proposition 2.2.6). Then, in this domain, it holds that $f^0 = \rho(t,x) G_{\eta(\rho)A_\Omega}$ with $\rho(t,x) = \int_{\mathbb{S}^{n-1}} f^0 du > \rho_*$, where $A_\Omega, G_{\eta(\rho)A_\Omega}, \eta(\rho)$ are given in (2.2.9), (2.2.10) and (2.2.13) respectively. Moreover, the mass density $\rho(t,x)$ and the mean-nematic direction of the particles $\Omega(t,x)$ satisfy the following system of equations*

$$\partial_t \rho = D_x \Delta_x \rho + \mu \nabla_x \cdot (K(\eta(\rho))\rho \nabla_x \rho), \tag{2.2.17a}$$
$$\partial_t \Omega + \mu \Pi_2(\rho)(\nabla_x \rho \cdot \nabla_x)\Omega + \mu(\sigma-\nu) P_{\Omega^\perp} \Delta_x \Omega = \mathbb{1}_{a=2} \lambda \Pi_3(\Omega,\rho). \tag{2.2.17b}$$

where

$$K(\eta(\rho)) := 1 - \frac{\chi^2}{n} - \sigma \frac{n-1}{n} S_2(\eta(\rho))\eta'(\rho), \tag{2.2.18}$$

and

$$\sigma := \frac{D_u}{\lambda}, \qquad \nu := \frac{D_x}{\mu}.$$

Moreover, Π_2 is given by

$$\Pi_2(\rho) = \frac{\sigma - 2\nu}{\rho} + \frac{\chi^2}{n} - 1 + 2\frac{\eta'(\rho)}{\eta(\rho)}(\sigma-\nu) + \eta'(\rho)\left(2(\sigma-\nu)\frac{c_{3,2}(\rho)}{c_{1,2}(\rho)} - d_{2,0}(\rho)(\sigma-2\nu) - \frac{\sigma}{n}\right),$$

where, for $k,p \in \mathbb{N} \cup \{0\}$, $c_{k,p} = c_{k,p}(\rho)$ and $d_{k,p} = d_{k,p}(\rho)$ are given by

$$c_{k,p}(\rho) := \int_0^\pi \cos^k\theta\, g_{\eta(\rho)}(\theta) h_{\eta(\rho)}(\cos\theta) \sin^{n-2+p}\theta \,\mathrm{d}\theta, \tag{2.2.19}$$
$$d_{k,p}(\rho) := \int_0^\pi \cos^k\theta\, g_{\eta(\rho)}(\theta) \sin^{n-2+p}\theta \,\mathrm{d}\theta, \tag{2.2.20}$$

where the function h_η is defined in Proposition 2.4.5 and the function g_η is given in (2.4.2). It holds that $\frac{c_{3,2}}{c_{1,2}} \geq 0$ and $d_{2,0} \geq 0$.

In the case of $a = 2$, the right hand side of (2.2.17b) does not vanish and Π_3 is given by

$$\frac{8c_{1,2}(\rho)\eta(\rho)}{(n-1)}\Pi_3(\Omega,\rho) = (\ell^2-d^2)[(H_2^r : (D_x^2\rho))]_{[2,3:1,2]} - 2\chi^2 d^2 [H_2^r : \Delta_x(\rho H_2)]_{[2,3:1,2]}$$
$$- \chi^2(\ell^2-d^2)\left([H_4^r : (D_x^2 \otimes (\rho H_2))]_{[2,3,4,5:1,2,3,4]} + [H_2^r \otimes D_x^2 : (\rho H_4)]_{[2,3,4,5:1,2,3,4]}\right) \tag{2.2.21}$$

where in the case of dimension $n = 2$ we have that

$$H_2 = d_{2,0}(\Omega \otimes \Omega) + d_{0,2}(\Omega^\perp \otimes \Omega^\perp), \tag{2.2.22}$$

$$H_2^r = d_{2,2}\Omega^\perp \otimes \Big((\Omega^\perp \otimes \Omega) + (\Omega \otimes \Omega^\perp)\Big), \tag{2.2.23}$$

$$H_4 = d_{4,0}(\Omega \otimes \Omega \otimes \Omega \otimes \Omega) + d_{2,2}S_{2\Omega,2\Omega^\perp}(\Omega, \Omega^\perp) + d_{0,4}(\Omega^\perp \otimes \Omega^\perp \otimes \Omega^\perp \otimes \Omega^\perp), \tag{2.2.24}$$

$$H_4^r = \Omega^\perp \otimes \Big(d_{4,2}S_{3\Omega,\Omega^\perp}(\Omega, \Omega^\perp) + d_{2,4}S_{\Omega,3\Omega^\perp}(\Omega, \Omega^\perp)\Big), \tag{2.2.25}$$

with

$$\begin{aligned} S_{2\Omega,2\Omega^\perp}(\Omega, \Omega^\perp) := (\Omega \otimes \Omega^\perp + \Omega^\perp \otimes \Omega) \otimes (\Omega \otimes \Omega^\perp + \Omega^\perp \otimes \Omega) \\ + \Omega \otimes \Omega \otimes \Omega^\perp \otimes \Omega^\perp + \Omega^\perp \otimes \Omega^\perp \otimes \Omega \otimes \Omega, \end{aligned}$$

and

$$S_{3\Omega,\Omega^\perp}(\Omega, \Omega^\perp) := (\Omega \otimes \Omega) \otimes (\Omega \otimes \Omega^\perp + \Omega^\perp \otimes \Omega) + (\Omega \otimes \Omega^\perp + \Omega^\perp \otimes \Omega) \otimes (\Omega \otimes \Omega)$$

and $S_{\Omega,3\Omega^\perp}$ is defined analogously as $S_{3\Omega,\Omega^\perp}$ (by exchanging the values of Ω and $\Omega^\perp$).

In dimension $n \geq 3$, the values of H_2, H_2^r, H_4, H_4^r are more complex and are given in Proposition 2.2.11 below.

Proposition 2.2.11 (Dimension $n \geq 3$)**.** *For $n \geq 3$ the functions H_2, H_2^r, H_4, H_4^r are given by*

$$H_2(\eta, \Omega, \Omega^\perp) = d_{2,0}(\Omega \otimes \Omega) + \frac{d_{0,2}}{n-1}P_{\Omega^\perp} \tag{2.2.26}$$

$$H_2^r(\eta, \Omega, \Omega^\perp) = \frac{d_{2,2}}{n-1}\left(P_{\Omega^\perp} \otimes \Omega + [P_{\Omega^\perp} \otimes \Omega \otimes P_{\Omega^\perp}]_{:24}\right) \tag{2.2.27}$$

$$\begin{aligned} H_4(\eta, \Omega, \Omega^\perp) = {} & d_{4,0}(\Omega \otimes \Omega \otimes \Omega \otimes \Omega) + \frac{d_{0,4}}{(n-1)(n+1)}\Gamma \\ & + \frac{d_{2,2}}{n-1}\Big(P_{\Omega^\perp} \otimes \Omega \otimes \Omega + \Omega \otimes P_{\Omega^\perp} \otimes \Omega + \Omega \otimes \Omega \otimes P_{\Omega^\perp} \\ & + [P_{\Omega^\perp} \otimes \Omega \otimes P_{\Omega^\perp} \otimes \Omega]_{:24} + [P_{\Omega^\perp} \otimes \Omega \otimes \Omega \otimes P_{\Omega^\perp}]_{:25} \\ & + [\Omega \otimes P_{\Omega^\perp} \otimes \Omega \otimes P_{\Omega^\perp}]_{:35}\Big) \\ H_4^r(\eta, \Omega, \Omega^\perp) = {} & \frac{d_{2,4}}{(n-1)(n+1)}T + \frac{d_{4,2}}{n-1}\Big(P_{\Omega^\perp} \otimes \Omega \otimes \Omega \otimes \Omega + [P_{\Omega^\perp} \otimes \Omega \otimes P_{\Omega^\perp} \otimes \Omega \otimes \Omega]_{:24} \\ & + [P_{\Omega^\perp} \otimes \Omega \otimes \Omega \otimes P_{\Omega^\perp} \otimes \Omega]_{:25} + [P_{\Omega^\perp} \otimes \Omega \otimes \Omega \otimes \Omega \otimes P_{\Omega^\perp}]_{:26}\Big), \end{aligned}$$

Where Γ is symmetric order-4 tensor defined by

$$\Gamma = 3Sym(P_{\Omega^\perp} \otimes P_{\Omega^\perp}). \tag{2.2.28}$$

In Cartesian coordinates Γ is given by

$$\Gamma_{ijkl} = (P_{\Omega^\perp})_{ij}(P_{\Omega^\perp})_{kl} + (P_{\Omega^\perp})_{ik}(P_{\Omega^\perp})_{jl} + (P_{\Omega^\perp})_{il}(P_{\Omega^\perp})_{jk}.$$

Also, T is a 5-tensor with components

$$T_{ijklp} = \tilde{S}_{ijkl}\Omega_p + \tilde{S}_{ijkp}\Omega_l + \tilde{S}_{ijpl}\Omega_k + \tilde{S}_{ipkl}\Omega_j \tag{2.2.29}$$

where

$$\tilde{S}_{iiii} = 3\Gamma_{iiii}, \quad \tilde{S}_{iijj} = \Gamma_{iijj}, \quad \tilde{S}_{ijij} = \Gamma_{ijij}, \quad \tilde{S}_{ijji} = \Gamma_{ijji},$$

for $i, j \in \{1, ..., n\}$ *such that* $i \neq j$*, otherwise* $\tilde{S}_{ijkl}$ *is zero. Above we used the notation*

$$[P_{\Omega^\perp} \otimes \Omega \otimes P_{\Omega^\perp}]_{:24}$$

to denote a 3-tensor whose (i, j, k) *component is given by*

$$\Big([P_{\Omega^\perp} \otimes \Omega \otimes P_{\Omega^\perp}]_{:24}\Big)_{ijk} = \sum_{p=1}^{n} (P_{\Omega^\perp})_{ip} \Omega_j (P_{\Omega^\perp})_{pk},$$

i.e., in this case we contract the full tensor $P_{\Omega^\perp} \otimes \Omega \otimes P_{\Omega^\perp}$*, which is a 5-tensor, by summing over the second and the forth indices (that is why we have the sub-index notation* $: 24$*). One defines the other contractions analogously.*

The proof of the Proposition 2.2.11 is given in Section 2.4.4.
Moreover, from Theorem 2.2.10 we can deduce the following:

Corollary 2.2.12 (Isotropic regime)**.** *Let* $n \in \{2, 3\}$ *and* $a \in (0, 2]$*. Suppose that* $f^\varepsilon \to \rho$ *as* $\varepsilon \to 0$*, then it holds that*

$$\partial_t \rho - D_x \Delta_x \rho + \mu \left(\frac{\chi^2}{n} - 1 \right) \nabla_x \cdot (\rho \nabla_x \rho) = 0. \tag{2.2.30}$$

Proof. The proof of the corollary directly follows the steps of the proof of Theorem 2.2.10 to obtain the equation for ρ. ∎ The proof of Theorem 2.2.10 is postponed to Section 2.4. Next, we

comment on Theorem 2.2.10, particularly on Equations (2.2.17a) and (2.2.17b).

2.2.3 Comments on the Continuum Equations

In this section we discuss the macroscopic equations for the mass density and the mean-nematic direction (2.2.17a) and (2.2.17b), respectively.

The Equation for the Mass Density

Equation (2.2.17a) is a diffusion-type equation in divergence form and hence the total mass $\int_{\mathbb{R}^n} \rho \, \mathrm{d}x$ is preserved over time. The equation is formed by the sum of a linear diffusion and a non-linear diffusion term. The purely diffusive term with the diffusion constant D_x arises from the Brownian motion at the particle level. The second term on the right-hand-side resembles a porous medium equation, but with a diffusion coefficient K that depends also on the density ρ. Numerical experiments indicate that $K(\eta(\rho))$, as given in Equation (2.2.18), is non-negative, see Remark 2.2.7.

Effect of particle anisotropy. Interestingly, the equation for the mass density is independent of the mean-nematic direction Ω. However, the anisotropy of the particles modifies Equation (2.2.17a). To understand the effect of particle anisotropy, characterised by χ and defined in (2.1.2), we first consider spherical particles. For spherical particles, $\chi = 0$, and the

potential V_b becomes isotropic, i.e.,

$$V_b(x_2 - x_1) = (4\pi)^{-n/2} \exp\left(-\frac{|x_2 - x_1|^2}{2d^2}\right).$$

In this case, particles' positions and directions are completely decoupled in the discrete system (2.1.3) since $\nabla_u V_b = 0$ and $\nabla_x V_b$ is independent of u. Moreover, one straightforwardly obtains the following equation for ρ (by directly integrating equation (2.2.4) and noting that $W_f = \rho$ in this case):

$$\partial_t \rho = D_x \Delta_x \rho + \mu \nabla_x \cdot (\rho \nabla_x \rho), \qquad \text{for} \quad \chi = 0,$$

which is the porous medium equation with linear diffusion. Notice that it corresponds to Equation (2.2.30), where we assumed that $f^\varepsilon \to \rho$ as $\varepsilon \to 0$. Therefore, the difference between the isotropic and the anisotropic cases is encapsulated in the non-linear diffusion coefficient $K(\eta) \neq 1$.

Now, notice that

$$K(\eta) \leq 1 - \frac{\chi^2}{n},$$

since $S_2(\eta) \in (0, 1)$ and η is non-decreasing (see also Figure 2.10).

Remark 2.2.7 (Non-negativity of the diffusion coefficient K)**.** *Even though, we do not have an analytical guarantee that K is non-negative, numerical simulations suggest that K actually has a lower bound $1-\chi^2 \geq 0$. Figure 2.3a shows the evolution of K as $\eta \geq 0$ varies for different values of χ. The dashed lines in matching colors represent the numerical lower bound for K and the dotted lines display the upper bound $1 - \frac{\chi^2}{n}$ for K. Moreover, in Figure 2.3b, the gray area shows the range of K values with respect to χ when other parameters, i.e. σ, also vary. Here, we can numerically further confirm that the lower bound for observed K values is $1-\chi^2$, denoted by the blue dashed line. Note also that, in dimension $n = 3$, χ can take negative values, i.e., $\chi \in [-1, 1]$. However, this does not change the value of K since only χ^2 is involved in the computation of K. That is why we only display $\chi \in [0, 1]$ in Figure 2.3b and naturally it would be symmetric for $\chi \in [-1, 0]$. Moreover, our numerical experiments include how K changes with respect to ρ for various $\chi \in (0, 1)$ values, see Figure 2.10c, where, again, K remains non-negative.*

Assuming that $K \geq 0$, the particle anisotropy contributes to a slowdown in the non-linear diffusion. In dimension $n = 3$, when the particles are rods ($\chi = 1$) or flat disks ($\chi = -1$) we have that $K(\eta) \leq 2/3$; thus, the original speed of diffusion μ is reduced to at least two-thirds of the anisotropic case. One may hypothesize that this effect is due to anisotropic particles being able to pack and occupy less volume when aligned, so they produce less diffusion. Indeed, our numerical investigations regarding the effect of particle anisotropy on the global alingment also confirm that particles with higher anisotropy reach total global alignment faster. We observe that the particles which are closer to perfect circle in shape ($\chi \approx 0$) and low in density do not reach alignment by the end of the simulation time, whereas particles which are more elongated ellipses ($\chi \approx 1$) with higher densities align globally in a shorter time frame, see, e.g., Figure 2.7. We refer to Section 2.3.2 for a detailed discussion.

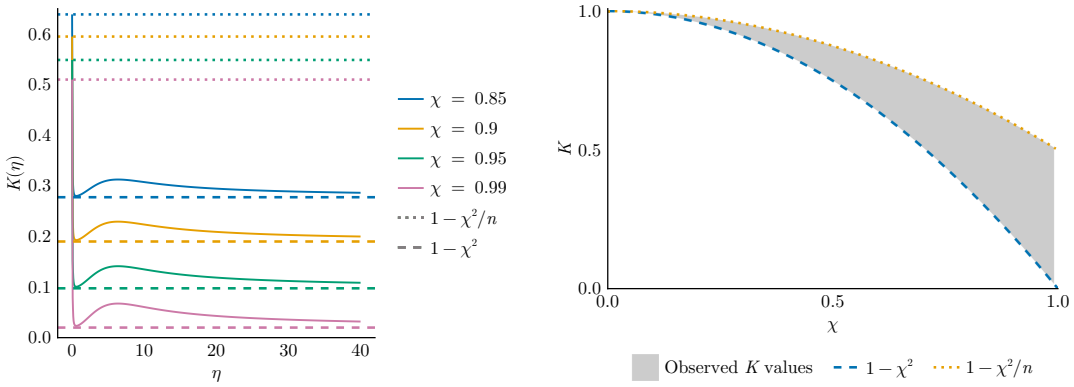

(a) Evolution of $K(\eta)$ with respect to η.

(b) Range of $K(\eta)$ with respect to χ.

Figure 2.3: (a) Time evolution of the diffusion coefficient $K(\eta)$ with respect to η with different χ values. The dotted lines and the dashed lines correspond to $1-\chi^2/n$ (upper bound for K) and $1-\chi^2$ (lower bound for K), respectively, for the matching color χ values. (b) The range of $K(\eta)$ for $\chi \in (0,1)$ and $\sigma \in [2^{-8}, 2^8]$. The dotted and the dashed lines show the upper and the (numerical) lower bound for K, respectively.

The Equation for the Mean-nematic Direction

First, we remark that the equation for the mean-nematic direction Ω, Equation (2.2.17b), is non-conservative. It can be verified that $|\Omega|(t)$ remains constant over time, as all the terms lie within the space spanned by $\Omega^{\perp}$. Consequently, Ω stays on the sphere at all times.

The term Π_2 corresponds to transport of Ω in the direction $\nabla_x \rho$. However, the sign of $\Pi_2(\rho)$ is not immediately clear, or it is uncertain if it changes sign during the dynamics. Notably, Π_2 would vanish if $\mu = 0$, indicating that this term arises from the repulsive potential acting on particle positions.

The last term on the left-hand side of (2.2.17b) corresponds to diffusion in the direction Ω. The projection term $P_{\Omega^{\perp}}$ ensures that Ω remains on the sphere. One can check that when particles are spherical, there is no equation for Ω, which is expected since the direction Ω does not influence the dynamics in this case. If $\mu = 0$, the diffusion constant reduces to D_x, meaning that, in this case, the diffusion originates only from the Brownian motion of the positions of the particles. Intriguingly, the constant $\mu\sigma$ introduces an anti-diffusion effect.

The case $a \in (0,2)$. When $a \in (0,2)$, the right-hand side of (2.2.17b) vanishes. In this case, the dynamics for ρ and Ω are identical for prolate and oblate particles with the same values of χ^2. Consequently, at the macroscopic level, the equations do not differentiate between these two types of particles.

The Case $a = 2$

When $a = 2$, the term Π_3, given by Equation (2.2.21), does not vanish. This term gives the effect of the repulsive potential on the directionality of the particles. Specifically, from Lemma 2.2.1, the potential V_f^{ε} expands as

$$V_f^{\varepsilon} = W_f + \varepsilon^2 B_f + \mathcal{O}(\varepsilon^3),$$

where W_f is a nematic-alignment force, and the term B_f - which generates Π_3 - arises from the specific form of the repulsive potential V_b considered. The term Π_3 involves either second-order differential operators or products of first-order differential operators.

Interpreting Π_3 is not straightforward, but it is clearly distinct from the other terms in Equation (2.2.17b). Notably, Π_3 is the only term where the distinction between oblate ($\ell < d$) and prolate ($\ell > d$) particles matter. Specifically, oblate and prolate particles exhibit opposite signs for the first and last two terms of Π_3. If the diffusion constants are positive for prolate particles, they will be negative for oblate particles, and vice versa. As a result, the qualitative behavior of oblate and prolate particles will differ significantly.

Notice that the second term in Π_3 is solely influenced by the length d. If $d = 0$ (i.e., if the particles are rod-shaped), this term disappears.

To simplify the interpretation of Π_3, in the next two paragraphs we focus only on dimension $n = 2$.

Anisotropic equilibrium ($d_{2,0} \neq d_{0,2}$). One can expand the contractions in Π_3 further considering expressions (2.2.22)-(2.2.25). For example, for the second term in (2.2.21) we have that:

$$\begin{aligned}[H_2^r : (\Delta_x(\rho H_2))]_{[2,3:1,2]} = {} & 2d_{2,2}d_{2,0}\Omega^\perp \left(\rho(\Omega^\perp \cdot \Delta_x\Omega) + 2\Omega^\perp \cdot [(\nabla_x\rho \cdot \nabla_x)\Omega]\right) \\ & + 2d_{2,2}d_{0,2}\Omega^\perp \left(\rho(\Omega \cdot \Delta_x\Omega^\perp) + 2\Omega \cdot [(\nabla_x\rho \cdot \nabla_x)\Omega^\perp]\right).\end{aligned}$$

For these equations, it is critical that $d_{2,0} \neq d_{0,2}$, since, if they were the same, then H_2 would be equal to the identity and this would imply that

$$[H_2^r : (\Delta\rho\mathrm{Id})]_{[2,3:1,2]} = 0,$$

since $(\Omega \otimes \Omega^\perp) : \mathrm{Id} = \Omega \cdot \Omega^\perp = 0$. Moreover, if $d_{2,0} = d_{0,2}$, then the third term of (2.2.21) would become:

$$[H_4^r : D_x^2 \otimes \rho\mathrm{Id}]_{[2,3,4,5:1,2,3,4]} = d_{2,0}(d_{2,4} + d_{4,2})\Omega^\perp[(\Omega \otimes \Omega^\perp + \Omega^\perp \otimes \Omega) : (D_x^2\rho)].$$

Therefore, the fact that $d_{2,0} \neq d_{0,2}$ creates an anisotropy that produces derivatives in Ω and $\Omega^\perp$. If $G_{\eta(\rho)A_\Omega}$ was the uniform distribution (i.e., if $\ell = d$), then we would have that $d_{2,0} = d_{0,2}$. Thus, this effect is linked to the anisotropy of the particles.

Cross-diffusion term. The term of Π_3 containing the second derivatives of ρ is

$$b(\rho)\rho\Omega^\perp[(\Omega \otimes \Omega^\perp + \Omega^\perp \otimes \Omega) : D_x^2\rho],$$

where

$$b(\rho) := \frac{n-1}{8\eta(\rho)c_{1,2}}(\ell^2 - d^2)\left(d_{2,2} - \chi^2(d_{4,2}d_{2,0} + d_{2,4}d_{0,2}) - 2\chi^2 d_{2,2}^2\right).$$

This term makes the system (2.2.17a)-(2.2.17b) of a cross-diffusion type. In dimension $n = 3$, it is clear that if the diffusion coefficient $b(\rho)$ is positive for prolate particles then it is negative for oblate particles (and vice versa). This will particularly complicate the study of the well-posedness of the equations, which we leave for future work.

2.2.4 Parameter Regime for the Validity of the Continuum Equations

It remains an open question to determine for which parameter regime the macroscopic equations (2.2.17a)-(2.2.17b) are well-posed. In particular, the consistency relation (2.2.14) imposes a major constraint on the dynamics. Particularly, when $\rho < \rho_*$, the macroscopic equations lose their validity. In this section, we illustrate this effect with a couple of examples.

Diffusion term in Ω. For the well-posedness of the equations, we require the diffusion constant in Ω, given by $\mu(\nu - \sigma)$, (see the left-hand side of (2.2.17b)), to be positive. This is equivalent to the condition:

$$\frac{\mu}{D_x} < \frac{\lambda}{D_u}.$$

This condition establishes a balance between the noise intensities D_x, D_u and the intensity of the alignment interactions μ, λ. If $\mu = \lambda$, then we must have $D_u < D_x$ (i.e., the noise intensity in the directions must be smaller than in the positions). If $D_x = D_u$, then $\mu < \lambda$ must hold (i.e., the intensity of the potential must be stronger for the directions than for the positions). Additionally, for well-posedness, it is required that $D_x > 0$. These parameter constraints suggest that there are certain aspects of the microscopic dynamics that the macroscopic equations fail to capture. Moreover, in Section 2.3.2, we present some numerical tests on this condition at the microscopic level, simulating the stochastic particle system (2.1.3). The results indicate that when the continuum equations are ill-posed, i.e., when $\sigma \geq \nu$, the particles do not reach any type of alignment. This can be observed particularly in Figures 2.4 and 2.5. For further details, we refer the reader to Section 2.3.2.

The critical case $\nu = \sigma$. Let us consider the critical case where $\nu = \sigma$. In this case the diffusive term in Ω vanishes. We explore this scenario in more detail.
Notice that we can rewrite the kinetic equation (2.2.6) (for $a \in (0, 2)$) as:

$$\partial_t f^\varepsilon - D_x \nabla_x \cdot \left(\nabla_x f^\varepsilon - \frac{\chi^2 \mu}{D_x} f^\varepsilon \nabla_x \left(u^T (\rho_f Q_f) u \right) \right) + \mu \left(\frac{\chi^2}{n} - 1 \right) \nabla_x \cdot ((\nabla_x \rho_{f^\varepsilon}) f^\varepsilon) = \frac{D_u}{\varepsilon} C(f^\varepsilon) + \mathcal{O}(\varepsilon^2), \quad (2.2.31)$$

where, we recall,

$$C(f) = \nabla_u \cdot \left(\nabla_u f - \frac{\chi^2 \lambda}{D_u} f \nabla_u \left(u^T (\rho_f Q_f) u \right) \right).$$

Notice that the second term in (2.2.31) has the same shape as the operator C except that the derivatives are in x and the parameter values differ.

If $\nu = \sigma$, i.e., $\frac{D_x}{\mu} = \frac{D_u}{\lambda}$, the second term in (2.2.31) can be rewritten as

$$-D_x \nabla_x \cdot \left(G_{\alpha \rho_f Q_f} \nabla_x \left(\frac{f^\varepsilon}{G_{\alpha \rho_f Q_f}} \right) \right), \quad \text{with } \alpha = \frac{\chi^2}{\sigma}. \quad (2.2.32)$$

By Lemma 2.2.7, when $f^\varepsilon \to \rho G_{\eta(\rho) A_\Omega}$, we have that $G_{\alpha \rho_f Q_f} \to G_{\eta(\rho) A_\Omega}$ and in the limit (2.2.32) becomes

$$-D_x \nabla_x \cdot \left(G_{\eta(\rho) A_\Omega} \nabla_x \rho \right).$$

Integrating (2.2.31), and using the fact that $\int G_{\eta(\rho)A_\Omega}\,\mathrm{d}u = 1$, we obtain Equation (2.2.30), which is the equation obtained in the isotropic regime corresponding to $f^\varepsilon \to \rho$ as $\varepsilon \to 0$. A possible explanation for this is that when $\mu = \sigma$ the density ρ declines rapidly below the critical density ρ_* due to the diffusive processes involved.

In conclusion, we emphasize two main takeaways on the validity of the continuum equations. Firstly, the macroscopic limit does not hold for arbitrary parameter values. Secondly, the macroscopic equation ceases to be valid when $\rho < \rho_*$ (at the points where Equation (2.2.30) holds and we enter the isotropic regime). However, we have no prior information on the specific points in space or the times at which this may occur.

We finish with a remark concerning the validity of the continuum equations for higher dimensions.

Remark 2.2.8 (Higher dimensions)**.** *The macroscopic limit presented in this paper only holds for $n \in \{2, 3\}$ since in Lemma 2.2.7 we only obtain stable equilibria for these dimensions. Existence of stable equilibria for $n \geq 4$ is an open problem. However, if Lemma 2.2.7 holds for $n \geq 4$, we could conjecture that Theorem 2.2.10 would also hold for $n \geq 4$.*

2.3 Repulsive Potentials and Particle Simulations

In this section, we comment on the different Gaussian-type repulsive potentials, motivate our choice (2.1.6) and present numerical simulations for particles following the dynamics (2.1.3a)-(2.1.3b).

2.3.1 Gaussian-Type Anisotropic Repulsive Potentials

Earlier, we described the binary interactions between identical particles via an anisotropic potential V_b given by Equation (2.1.4). We comment on two particular choices of the scaling factor $b \geq 0$ in (2.1.4).

The Berne-Pechukas potential. One of the first soft anisotropic potentials that appeared in the literature is that of a soft repulsive potential between two spheroids using the Gaussian potential. It was first introduced by Berne and Pechukas in [19]. In [19], the scaling factor $b(u_1, u_2)$ is given by

$$b_{\mathrm{BP}}(u_1, u_2) := (1 - \chi^2(u_1 \cdot u_2)^2)^{-1/2} = \det(\Sigma)^{-1/2}, \tag{2.3.1}$$

where χ is defined by (2.1.2). This is a very natural choice for the scaling factor b, as it guarantees that V_b is a multivariate Gaussian distribution in the variable R with a covariance matrix given by $\Sigma/2$.

The non-scaled Gaussian potential. Berne and Pechukas in [19] considered a scaling factor b such that the potential (2.1.4) is normalized, i.e., $\int_{\mathbb{R}^d} V_{b_{\mathrm{BP}}}(u_1, u_2, R)\,\mathrm{d}R = 1$. However, one could choose to work directly with the potential without normalization, i.e., consider the scaling factor

$$b_{\mathrm{NR}}(u_1, u_2) := (4\pi)^{n/2}. \tag{2.3.2}$$

Notice that both, the potential $V_{b_{\mathrm{BP}}}$ and the potential without normalization $V_{b_{\mathrm{NR}}}$, have the same level sets in space (up to scaling). The level sets in directions, however, are different and this has important consequences.

Motivation for the Interaction Potential

We focus on the non-scaled Gaussian potential for two reasons. Firstly, the Berne-Pechukas potential does not produce nematic alignment at first order, see below item (ii). Secondly, we want to avoid the modification in the directions introduced by the scaling. However, considering a system interacting via this potential is mathematically challenging to study, and, therefore, we consider a modified version of the non-scaled Gaussian potential, retaining the similar properties, this was explained in Remark 2.1.1. Instead of (2.3.2), we work with (2.1.6), as introduced earlier. This simplification resembles to the simplification done when considering the Maier-Saupe potential $b_{\mathrm{MS}}(u,u') := (u \cdot u')^2$ instead of the Onsager potential $b_{\mathrm{O}}(u,u') := |u \cdot u'|$, see, [102]. Both potentials have the same minimizer, but b_{MS} is easier to study mathematically.

Moreover, using (2.1.6), we then observe that the leading term of the expansion (2.2.1) is given by

$$W_f(t,x_1,u_1) := \int_{\mathbb{S}^{n-1}} \left(1-\chi^2(u_1\cdot u_2)^2\right) f(t,x_1,u_2)\,\mathrm{d}u_2.$$

The function inside the integrand $\varphi(u_1,u_2) := \left(1-\chi^2(u_1\cdot u_2)^2\right)$ resembles that of the Maier-Saupe potential [102] and motivates our choice for the rescaling factor b. In particular,

(i). if we consider $b \equiv 1$ (i.e., without scaling of the potential), we obtain

$$\tilde{W}_f(t,x_1,u_1) := \int_{\mathbb{S}^{n-1}} \left(1-\chi^2(u_1\cdot u_2)^2\right)^{1/2} f(t,x_1,u_2)\,\mathrm{d}u_2,$$

with $\tilde{\varphi}(u_1,u_2) := \left(1-\chi^2(u_1\cdot u_2)^2\right)^{1/2}$. Even though the potential with φ and the potential with $\tilde{\varphi}$ have the same minimizers in terms of u_1, u_2, W_f is more straightforward to analyze since we can rewrite it as

$$W_f(t,x_1,u_1) = u_1^T \left(\int_{\mathbb{S}^{n-1}} (\mathrm{Id} - \chi^2(u_2\otimes u_2)) f(t,x_1,u_2)\,\mathrm{d}u_2 \right) u_1,$$

i.e., we can decouple the variables u_1 and u_2 and recast W_f in terms of Q_f (see Equations (2.1.9) and (2.2.5)). As previously mentioned, a similar simplification is done when, instead of considering the Onsager potential $b_{\mathrm{O}}(u_1,u_2) = |u_1\cdot u_2|$, one considers the Maier-Saupe potential $b_{\mathrm{MS}}(u_1,u_2) = (u_1\cdot u_2)^2$, see [102] for more details.

(ii). If we consider the Berne-Pechukas scaling b_{BP} in (2.3.1), then the corresponding potential takes the form

$$W_f^{\mathrm{BP}}(t,x_1) = \int_{\mathbb{S}^{n-1}} f(t,x_1,u_2)\,\mathrm{d}u_2 = \rho(t,x_1). \tag{2.3.3}$$

Since the total integral of $V_{b_{\mathrm{BP}}}$ is one, we do not obtain a nematic alignment potential at the leading order.

In Section 2.3.2, we provide a numerical comparison of stochastic particle systems interacting via these different potentials. Indeed, we observe that particles interacting via the Berne-Pechukas potential do not align, see Figure 2.9.

2.3.2 Numerical Simulations

This section is dedicated to the numerical simulations of the stochastic particle system (2.1.3), particularly to compare the particle-level dynamics at longer times with our analytical predictions on the macroscopic dynamics.

We start with the study of how the central assumption for well-posedness (2.1.10) at the macroscopic level affects the particle dynamics. Subsequently, we investigate the impact of the anisotropy of the particles (measured by χ defined in (2.1.2)) and the particle density on the particle interaction dynamics. We finish the numerical simulations section with a comparison between the different types of interaction potentials mentioned in Section 2.3.1.

The source code for the particle simulations is provided at

https://github.com/cwytrzens/anisotropic_particles.

Numerical Implementation

We simulate the discrete particle dynamics in dimension $n = 2$, governed by the stochastic differential equations (2.1.3a) and (2.1.3b) on a periodic domain. The simulations use an explicit Runge-Kutta Milstein method of strong order 1 with adaptive time stepping. This numerical method is part of the Julia package `StochasticDiffEq.jl`, see [92]. Since we want to study a wide range of model parameters, it is crucial to use an adaptive time-stepping method, as the stiffness of the system strongly depends on the model parameters and differs across the parameter range that we investigate. We use default tolerance parameters $\texttt{reltol} = 10^{-2}$ and $\texttt{abstol} = 10^{-2}$. Moreover, in order to allow faster numerical evaluations of the interaction forces, we truncate the potential V_b as defined in Equation (2.1.4) for $R = |X_j - X_i| \geq 8 \max(\ell, d)$.

For the particle simulations, we consider a square domain of size $[0, L_x] \times [0, L_y]$ with $L_x = L_y = 100$ and fix the number of particles at $N = 10^5$. The initial positions X_i and directions u_i of the particles are taken uniform and random for $i = 1, ..., N$. Moreover, we set $t_{\text{end}} = 1.5 \times 10^5$, the time at which the simulations stop.

We perform an extensive parameter study for each remaining parameter pair, namely, the diffusion constants in space D_x and direction D_u; the strength factors of the repulsive force, μ and λ; the anisotropy parameter χ, and the particle density $\bar{\rho}$ which we define as

$$\bar{\rho} := \frac{\pi \ell d N}{L_x L_y}, \tag{2.3.4}$$

and it represents the ratio of the total volume of all particles to the domain size. The parameters χ and $\bar{\rho}$ determine d and ℓ uniquely (by solving (2.1.2) and (2.3.4) for d and ℓ).

Parameter Study

For the parameter study, we focus on capturing the regime of parameter values at which the global alignment is reached versus those at which the particles fail to align globally. As the dynamics depend on many parameters and the balance between them, capturing all interesting parameter combinations is very challenging; thus, out of the scope of this numerical study. To measure alignment, we compute the order parameter γ_f which is given in (2.2.16). If not stated otherwise, all the simulations use the default parameters given in Table 2.1.

To capture the transition to alignment, we typically vary one or two parameters while keeping the others fixed. This approach allows for a direct comparison between our numerical results and the theoretical prediction that the condition $\sigma < \nu$ is necessary for well-posedness of the

Parameter	Value
χ	0.9
$\overline{\rho}$	1
D_x	2^{-4}
D_u	2^{-11}
λ	2^8
μ	2^{13}
N	10^5
L_x, L_y	100
t_{end}	1.5×10^5

Table 2.1: Default model parameters for the simulations of the particle system.

continuum equations, see (2.1.10). Recalling that $\sigma = \frac{D_u}{\lambda}$ and $\nu = \frac{D_x}{\mu}$, we study the trajectories of the order parameter γ_f by varying D_u relative to D_x, and λ relative to μ, while keeping the remaining parameters constant.

Another primary feature of our particle system is the global alignment induced by the anisotropy of the particles. To investigate this feature, we conduct a parameter study of χ versus $\bar{\rho}$. Specifically, we study the impact of the anisotropy parameter χ on global alignment by defining the parameters ℓ and d implicitly in terms of χ and $\bar{\rho}$.

For each parameter pair (D_x, D_u), (λ, μ), and $(\chi, \bar{\rho})$, we present three plots:

(a) The expected trajectories of the mean global alignment γ_f, obtained by varying one parameter while keeping the others constant.

(b) A similar plot for the second parameter of the pair.

(c) A heatmap of the mean order parameter γ_f at the final simulation time t_{end}, obtained by varying both parameters simultaneously. The heatmap highlights the transition to alignment with the transition front ($\sigma = \nu$) marked by a red line.

For each parameter combination, we collect 8 simulation samples to estimate the trajectory of the mean global alignment, where the matching color bands show the standard deviation.

Simulation Results

In this section, we present the results of our numerical experiments.

We start with the study of our first parameter pair, diffusion constants D_x and D_u, presented in Figure 2.4. Figure 2.4a displays the trajectories of the order parameter γ_f over time for different values of $D_x = 2^{-k}$ for $k = 2, \dots, 7$ and D_u fixed at 0. Hence, there is no noise present in the particle directions u. We observe that the smaller the value of D_x, the slower the emergence of the global alignment. We fix $D_x = 2^{-4}$ as the default value and look at various D_u values in Figure 2.4b.

We observe an opposite effect for D_u. In Figure 2.4b, varying D_u shows that less angular noise leads to quicker alignment and too large noise might prevent reaching alignment all-together.

Finally, in Figure 2.4c, we display the order parameter γ_f at the final simulation time t_{end} as a heatmap of varying D_x versus D_u. Here, we observe the parameter range leading to alignment

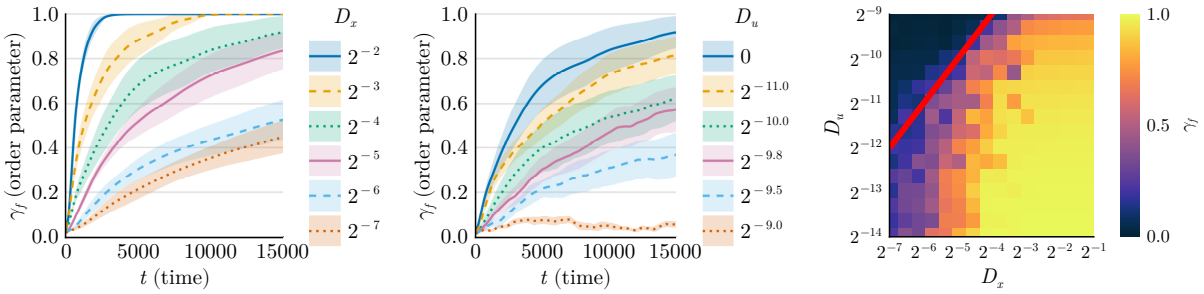

(a) $D_u = 0$ and D_x varying (b) $D_x = 2^{-4}$ and D_u varying (c) Heatmap of γ_f: D_x vs. D_u.

Figure 2.4: Parameter study for (D_x, D_u). Trajectories of the order parameter γ_f are plotted for fixed $D_u = 0$ and varying D_x in Figure 2.4a; for fixed $D_x = 2^{-4}$ and varying D_u in Figure 2.4b. Figure 2.4c displays a heatmap of γ_f at time $t_{\text{end}} = 1.5 \times 10^5$ while both D_u and D_x vary simultaneously. The red line depicts where $\nu = \sigma$.

and a transition along level sets of D_x versus D_u. At the particle level, the heatmap can be interpreted as follows. Increasing the positional noise facilitates interactions among a greater variety of particles, as neighboring particles change quickly, which contributes to reaching global alignment. On the contrary, increasing the directional noise drives the system away from global alignment, which is, in particular, critical if particles only interact with their nearest neighbors. Consequently, we observe a lack of alignment in the top left corner of the heatmap, where positional noise is low and directional noise is high.

Note that the red line displays where $\nu = \frac{D_x}{\mu} = \frac{D_u}{\lambda} = \sigma$. This indicates the interface at which the macroscopic equation (2.2.17b) for the mean-nematic direction Ω_f becomes ill-posed, see the discussion on well-posedness in Section 2.2.4. Crucially, the right-hand side of this red line is the parameter regime $(\sigma < \nu)$ where the macroscopic equations remain well-posed, and it is exactly in this parameter regime that we observe the onset of particle alignment.

In Figure 2.5, we investigate how the forces acting on positions X_i and directions u_i affect the alignment of particles. The strength factors of these forces are determined by the positive constants μ and λ in front of the interaction terms in Equations (2.1.3a) and (2.1.3b).

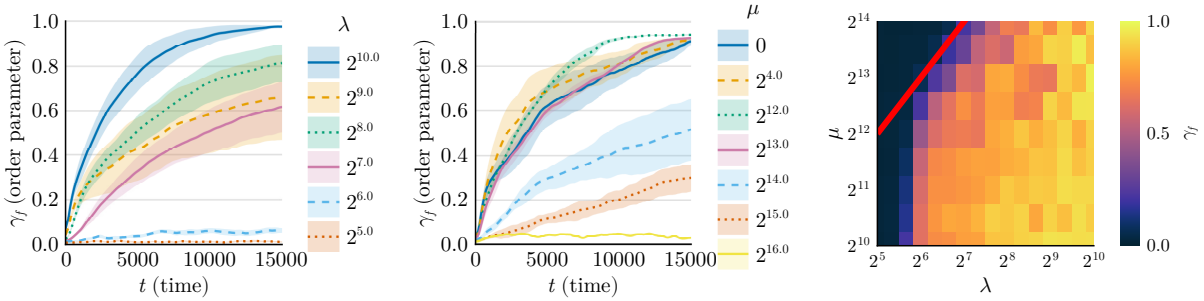

(a) $\mu = 2^{13}$ and λ varying. (b) $\lambda = 2^8$ and μ varying. (c) Heatmap of γ_f: λ vs. μ.

Figure 2.5: Parameter study for (λ, μ). Trajectories of the order parameter γ_f are plotted for fixed $\mu = 2^{13}$ and varying λ in Figure 2.5a; for $\lambda = 2^8$ and varying μ in Figure 2.6a. Figure 2.5c displays the heatmap of γ_f at time $t_{\text{end}} = 1.5 \times 10^5$ while both λ and μ vary simultaneously. The red line depicts where $\nu = \sigma$.

Figure 2.5a shows the trajectories of the order parameter γ_f over time for fixed $\mu = 2^{13}$ and varying values of λ from 2^5 to 2^{10}. We observe that for $\lambda \leq 2^6$, the system is in total chaos, with γ_f close to 0, indicating that the force acting on the particles' directions is not strong enough to drive the system towards alignment. Additionally, we deduce that as λ increases, γ_f appears to increase accordingly.

Next, we fix $\lambda = 2^8$ and vary μ from 0 to 2^{16} to study how the strength of the potential V_b affects the alignment through the force acting on the particles' positions. In Figure 2.5b, we observe that μ must be sufficiently large to have a significant impact on the particle dynamics. As μ increases, the particles lose their alignment, see, e.g., when $\mu = 2^{16}$, γ_f is very close to 0.

Lastly, we present a heatmap of the order parameter γ_f in Figure 2.5c, similar to Figure 2.4c, but for λ versus μ. Similarly, the red line displays the interface of the analytical well-posedness condition $\nu = \sigma$, see Equation (2.1.10). Again, we observe that global alignment only occurs inside the parameter range where the macroscopic equations are well-posed ($\sigma < \nu$), located on the right-hand side of the red line.

As for our last parameter pair, in Figure 2.6 we study the effects of the anisotropy χ and the density of particles $\bar{\rho}$ on the global alignment. In Figure 2.6a, we present a plot of the trajectories of γ_f when $\bar{\rho} = 1$ and the anisotropy parameter χ is varying from 0.6 to 1. We can clearly deduce that a certain degree of anisotropy is required for particles to reach global alignment.

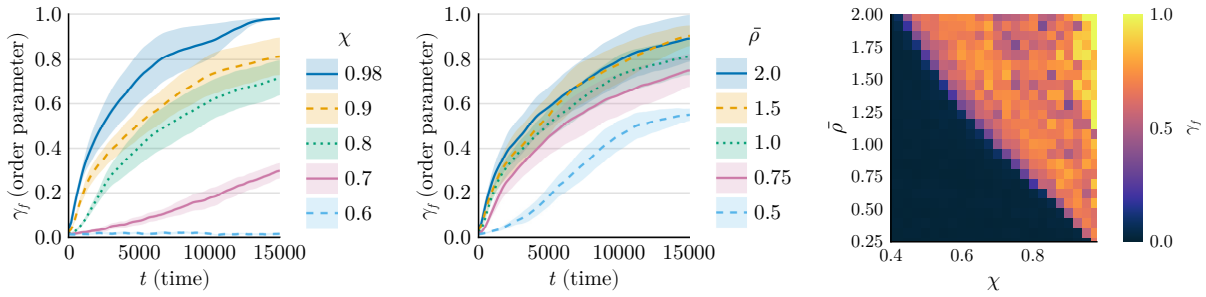

(a) $\bar{\rho} = 1$ and χ varying. (b) $\chi = 0.9$ and $\bar{\rho}$ varying. (c) Heatmap of γ_f: χ vs. $\bar{\rho}$.

Figure 2.6: Parameter study for $(\chi, \bar{\rho})$. Trajectories of the order parameter γ_f are plotted for fixed $\bar{\rho} = 1$ and varying χ in Figure 2.6a; for fixed $\chi = 0.9$ and varying $\bar{\rho}$ in Figure 2.6b. Figure 2.6 displays the heatmap of γ_f at time $t_{\text{end}} = 1.5 \times 10^5$ while both χ and $\bar{\rho}$ vary simultaneously.

In Figure 2.6b, we fix $\chi = 0.9$ and vary $\bar{\rho}$ from 0.5 to 2 (recall that $\bar{\rho}$ is computed using (2.3.4)) and plot the trajectories of γ_f. We observe that the particle density must also be sufficiently high for particles to align, otherwise, if the particles are too far apart, the repulsive potential is not strong enough to induce alignment. Figure 2.6c presents a heatmap illustrating the effect of both χ and $\bar{\rho}$ on the transition towards a higher-order alignment. Here, we also observe a clear linear progression, moving from a chaotic state, where γ_f is close to 0, to a well-ordered system, characterized by global alignment with $\gamma_f \approx 1$.

Moreover, to further investigate the effect of the shape of the particles on the global alignment of the system, we present in Figure 2.7 another heatmap of γ_f with the same dataset as in Figure 2.6c. However, in Figure 2.7 we compare the effect of varying the lengths of the major and the minor axes of the ellipses, i.e., ℓ and d, on global alignment rather than with respect to χ and $\bar{\rho}$. Notice that depending on ℓ and d, both χ and $\bar{\rho}$ vary across the heatmap accordingly. The

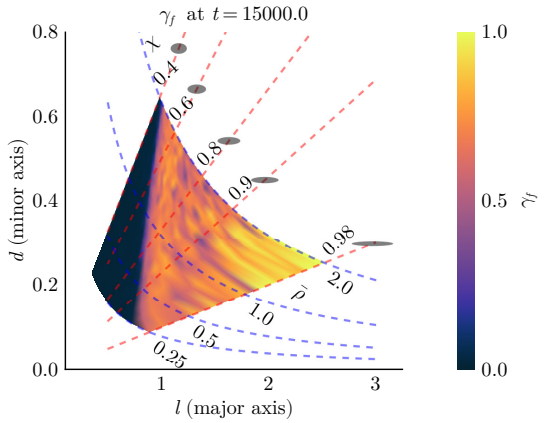

Figure 2.7: Heatmap of γ_f: χ versus $\bar{\rho}$. The dashed red lines display the anisotropy parameter χ for the corresponding lenghts of the major and minor axes of the ellipses, ℓ and d respectively. Ellipses with corresponding χ are pictured in gray. The dashed blue lines are the constant density curves $\bar{\rho}$ corresponding to ℓ and d, computed using (2.3.4).

red dashed lines display the constant χ curves, and similarly the blue dashed lines represent the constant $\bar{\rho}$ curves. This figure also confirms that the larger the particle anisotropy, the easier global alignment is achieved.

We remark that these numerical findings are in total agreement with our analytical conclusions. More precisely, at the macroscopic level, this behavior is also evident since the repulsive potential V_b ultimately gives rise to the nematic alignment potential with the factor $1 - \chi^2(u \cdot u_2)^2$ in Equation (2.2.2). Consequently, when particles are circular ($\chi = 0$), no alignment is observed at the macroscopic level. Also the effect of the potential is less for smaller values of χ.

We end this section with several snapshots of a particle simulation. In Figure 2.8, we start with a completely random state on the upper left figure and run the simulation using the default parameters in Table 2.1. Above each snapshot, we display the time at which the snapshot was captured with together with the value of the order parameter γ_f of the system at that time. The colors represent the nematic direction of the particles.

The particles start to align over time and hence, the also the order parameter γ_f increases in time. Finally, the bottom right snapshot in Figure 2.8 shows that the system reaches a globally aligned state with $\gamma_f = 0.92$, displayed in uniform colors, at the final simulation time t_{end}.

Numerical Comparison of the Potentials

Another prediction we draw from our mathematical analysis in Section 2.3.1 is the lack of alignment in the case of the Berne-Pechukas potential (2.3.3). To test this hypothesis numerically, we consider an interpolation between the weighted Gaussian potential and the Berne-Pechukas potential,

$$V_\xi(u_1, u_2, R) := (4\pi)^{-n/2} \det(\Sigma)^{\frac{1}{2}-\xi} \exp(-R^T \Sigma^{-1} R),$$

where $\xi \in [0, 1]$ and recalling that $\det(\Sigma) = 1 - \chi^2(u_1 \cdot u_2)^2$. Notice that V_ξ corresponds to

- the weighted Gaussian potential, given by $V_{b_{\text{WG}}}$ (2.1.6), when $\xi = 0$,
- the non-scaled Gaussian potential $V_{b_{\text{NR}}}$, obtained by using the scaling factor (2.3.2), when $\xi = \frac{1}{2}$,
- the Berne-Pechuckas potential $V_{b_{\text{BP}}}$, obtained by using the scaling factor (2.3.3), when $\xi = 1$.

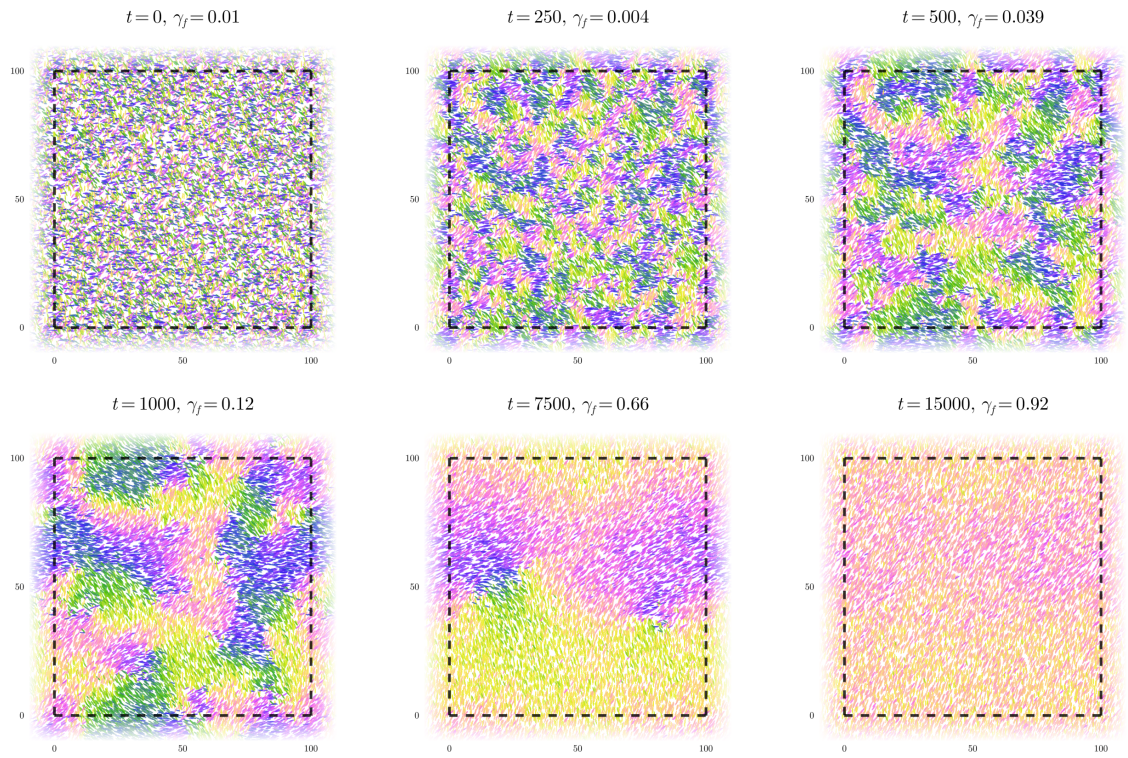

Figure 2.8: Snapshots of a particle simulation at different times using the default parameters given in Table 2.1. Different colors represent the different nematic directions of the particles. For the corresponding movie and movies for other cases see link https://doi.org/10.6084/m9.figshare.27117136.v1.

We remark that with increasing ξ, the scale of the potential might change, since we have

$$\frac{V_\xi}{V_{b_{\mathrm{WG}}}} = \frac{(1-\chi^2(u_1\cdot u_2)^2)^{\frac{1}{2}-\xi}}{(1-\chi^2(u_1\cdot u_2)^2)^{\frac{1}{2}}} \leq \frac{1}{(1-\chi^2)^\xi}.$$

In Section 2.3.2, we observed (see Figure 2.5) that increasing λ increases the order parameter γ_f; thus, has a positive effect on the global alignment. Therefore, we consider the scaling $\lambda = ((1-\chi^2)^{2\xi})\lambda'$ so that increasing ξ increases λ' and speeds up the alignment. Notice that here we chose the exponent 2ξ instead of just ξ to promote even stronger alignment for larger ξ values. For the simulations we use the default parameters listed in Table 2.1.

Figure 2.9 displays the trajectories of the order parameter γ_f for different values of ξ. We clearly observe a sharp transition from higher ordered states to a disordered state (where γ_f is nearly 0) as we increase $\xi = 0$ (the weighted Gaussian potential) to $\xi = 1$ (the Berne-Pechukas potential). Moreover, we also obtain global alignment for $\xi = \frac{1}{2}$ (the non-scaled Gaussian potential). Thus, our numerical study of the potentials strongly supports our analytical predictions in Section 2.3.1.

Summary of the numerical studies.

In this section, we conducted comprehensive numerical parameter studies on various parameter pairs: (D_x, D_u), (λ, μ), and $(\chi, \bar{\rho})$. We also compared different interaction potentials by simulating the stochastic particle system (2.1.3). Given the complex dynamics governed by

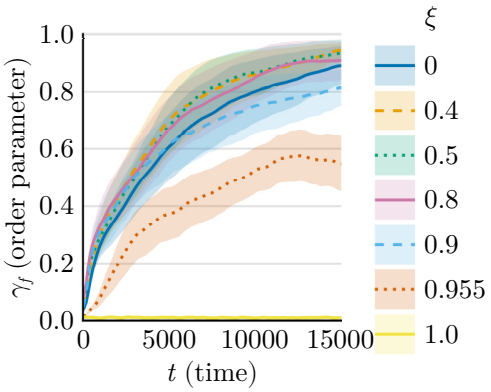

Figure 2.9: Trajectories of the order parameter γ_f are plotted for varying ξ and the remaining parameters are fixed at their default values given in Table 2.1. For $\xi = 0$, $\xi = 1/2$ and $\xi = 1$, V_ξ corresponds to the weighted Gaussian potential $V_{b_{\mathrm{WG}}}$, the non-scaled Gaussian potential $V_{b_{\mathrm{NR}}}$ and the Berne-Pechuckas potential $V_{b_{\mathrm{BP}}}$, respectively.

(2.1.3), it is numerically very challenging to determine all the interesting parameter regimes. Hence, we focused on the transitional ranges where global alignment breaks down. While the observed trends can be intuitively explained at the particle level, they are closely linked to our analytical results in the following ways:

- Global alignment fails to emerge for parameters where the macroscopic equation for the mean-nematic alignment Ω is ill-posed, as characterized by the well-posedness condition (2.1.10). This effect is evident in Figures 2.4c and 2.5c.
- Particle shape and density significantly influence the phase transition towards global alignment. As predicted by the macroscopic equations, spherical particles and low densities result in slower rates of alignment or a complete lack thereof.
- Our numerical tests confirm that the Berne-Pechukas potential does not lead to global alignment at the particle level, which aligns with the macroscopic perspective presented in Section 2.3.1.

2.4 Proof of Theorem 2.2.10

This section is dedicated to the proof of our main result, Theorem 2.2.10. First we give some preliminary tools that will be used later in the proof.

2.4.1 Preliminaries

Change of variables. In the sequel, we apply repeatedly the following change of variables $u \mapsto (\theta, v)$ where $u \in \mathbb{S}^{n-1} \setminus \{\pm\Omega\}$ and $(\theta, v) \in (0, \pi) \times \mathbb{S}^{n-2}$ defined by

$$\begin{aligned} u &= (u \cdot \Omega)\Omega + P_{\Omega^\perp}(u) = \cos\theta\Omega + \sin\theta v, \\ \mathrm{d}u &= \sin^{n-2}\theta \,\mathrm{d}\theta \,\mathrm{d}v, \end{aligned} \tag{2.4.1}$$

where $\mathbb{S}^{n-2}$ is identified as $\mathbb{S}^{n-1} \cap \Omega^\perp$. For simplicity, we assume that the measure $\mathrm{d}u$ is such that the total mass of the sphere is 1, i.e., $\int_{\mathbb{S}^{n-1}} \mathrm{d}u = 1$. In the course of the proof, we will also apply this change of variables to the Gibbs distribution $G_{\eta(\rho)A_\Omega}$ as stated in (2.2.10). Hence, we

define

$$g_\eta(\theta) := \frac{e^{\eta(\rho)\cos^2\theta}}{Z_\eta}, \quad \text{where} \quad Z_\eta = \int_0^\pi e^{\eta(\rho)\cos^2\theta'}\,\mathrm{d}\theta'. \tag{2.4.2}$$

as the transformed Gibbs distribution. Indeed, notice that the value of the normalizing factor Z_η does not depend on Ω, but it depends on $\eta = \eta(\rho)$. For more details on this change of variables see [47].

Derivatives and integrals. Since we will use various derivatives of $G_{\eta(\rho)A_\Omega}$, we collect them below in the following Lemma:

Lemma 2.4.1. *Let $G_{\eta(\rho)A_\Omega}$ be the Gibbs distribution defined in* (2.2.10)*. Then the following holds,*

$$\begin{aligned}
\frac{\partial G_{\eta(\rho)A_\Omega}}{G_{\eta(\rho)A_\Omega}} &= \eta'(\rho)(\partial\rho)\left((u\cdot\Omega)^2 - d_{2,0}(\rho)\right) + 2\eta(\rho)(u\cdot\Omega)(u\cdot\partial\Omega),\\
\frac{\nabla_x G_{\eta(\rho)A_\Omega}}{G_{\eta(\rho)A_\Omega}} &= \eta'(\rho)(\nabla_x\rho)\left((u\cdot\Omega)^2 - d_{2,0}(\rho)\right) + 2\eta(\rho)(u\cdot\Omega)(u\cdot\nabla_x\Omega),\\
\frac{\partial^2 G_{\eta(\rho)A_\Omega}}{G_{\eta(\rho)A_\Omega}} &= \partial^2\eta\left((u\cdot\Omega)^2 - d_{2,0}(\rho)\right) + \partial\eta\left(4(u\cdot\Omega)(u\cdot\partial\Omega) - \partial d_{2,0}(\rho)\right)\\
&\quad + 2\eta(u\cdot\partial\Omega)^2 + 2\eta(u\cdot\Omega)(u\cdot\partial^2\Omega) + \left(\partial\eta((u\cdot\Omega)^2 - d_{2,0}(\rho)) + 2\eta(u\cdot\Omega)(u\cdot\partial\Omega)\right)^2,
\end{aligned} \tag{2.4.3}$$

where ∂ denotes the partial derivative with respect to time or with respect to one of the spatial components, i.e., $\partial = \partial_t$, or $\partial = \partial_{x_i}$, $i = 1,\dots,n$; $\nabla_x\Omega$ is a matrix such that $(\nabla_x\Omega)_{ij} = \partial_{x_j}\Omega_i$ and thus $(u\cdot\nabla_x\Omega)_i = u\cdot\partial_{x_i}\Omega$ and $(\partial^2\Omega)_i = \partial^2\Omega_i$.

Proof. The proof follows directly from straightforward computations. ∎

Lemma 2.4.2. *Let h_η be any odd function, $w\in\mathbb{R}^n$, and $k\in\mathbb{N}\cup 0$. Then the following holds for $\boldsymbol{\psi}(u) := h_\eta(u\cdot\Omega)\,P_{\Omega^\perp}u$:*

$$\int_{\mathbb{S}^{n-1}} (u\cdot\Omega)^k\, G_{\eta(\rho)A_\Omega}\boldsymbol{\psi}(u)\,\mathrm{d}u = 0, \tag{2.4.4}$$

$$\int_{\mathbb{S}^{n-1}} (u\cdot w)(u\cdot\Omega)^k\, G_{\eta(\rho)A_\Omega}\boldsymbol{\psi}(u)\,\mathrm{d}u = \frac{c_{k,2}}{n-1}P_{\Omega^\perp}w, \tag{2.4.5}$$

$$\int_{\mathbb{S}^{n-1}} (u\cdot\Omega)^k\,\partial G_{\eta(\rho)A_\Omega}\boldsymbol{\psi}(u)\,\mathrm{d}u = \eta(\rho)\frac{2c_{k+1,2}}{n-1}\partial\Omega, \tag{2.4.6}$$

$$\begin{aligned}
\int_{\mathbb{S}^{n-1}} (u\cdot w)(u\cdot\Omega)^k\,\partial G_{\eta(\rho)A_\Omega}\boldsymbol{\psi}(u)\,\mathrm{d}u &= \\
\eta'(\rho)(\partial\rho)(c_{k+2,2} - d_{2,0}c_{k,2})\frac{1}{n-1}w &\quad \text{for } w\perp\Omega,
\end{aligned} \tag{2.4.7}$$

$$\int_{\mathbb{S}^{n-1}} (u\cdot\Omega)^{2k}(u\cdot w)^2\, G_{\eta(\rho)A_\Omega}\boldsymbol{\psi}(u)\,\mathrm{d}u = 0 \quad \text{for } w\perp\Omega, \tag{2.4.8}$$

$$\begin{aligned}
\int_{\mathbb{S}^{n-1}} \partial^2 G_{\eta(\rho)A_\Omega}\boldsymbol{\psi}(u)\,\mathrm{d}u &= \frac{4}{n-1}\left(c_{1,2} + \eta(\rho)(c_{3,2} - d_{2,0}c_{1,2})\right)\partial\eta\partial\Omega\\
&\quad + \frac{2c_{1,2}}{n-1}\eta(\rho)P_{\Omega^\perp}\partial^2\Omega,
\end{aligned} \tag{2.4.9}$$

where the partial derivatives are with respect to time or space, i.e., $\partial = \partial_t, \partial_{x_i}$ with x_i being the i-th component of x and the coefficients $c_{k,p}$, $d_{k,p}$ are given in (2.2.19) *and* (2.2.20)*. Moreover, it also holds that*

$$d_{k,p} = 0 \quad \text{for } k \text{ odd} \qquad \text{and} \qquad c_{k,p} = 0 \quad \text{for } k \text{ even.}$$

Proof. The proof of this lemma can be found in Appendix 2.6.2. ∎

Finally, notice that

$$\partial\Omega \perp \Omega$$

for $\partial = \partial_t, \partial_{x_i}$ (since $\Omega \cdot \partial\Omega = \partial|\Omega|^2/2 = 0$). Therefore, it holds that

$$P_{\Omega^\perp}\partial\Omega = \partial\Omega. \tag{2.4.10}$$

Next, we consider the following integrals with respect to $v \in \mathbb{S}^{n-2}$.

Lemma 2.4.3 (Lemma 4.1 in [47])**.** *Let $n \geq 2$ and $v \in \mathbb{S}^{n-2}$. Then, we have*

$$\int_{\mathbb{S}^{n-2}} v^{\otimes(2k+1)} \,\mathrm{d}v = 0, \quad \forall k \in \mathbb{N}, \tag{2.4.11}$$

$$\int_{\mathbb{S}^{n-2}} v \otimes v \,\mathrm{d}v = \frac{1}{n-1} P_{\Omega^\perp}, \tag{2.4.12}$$

$$\int_{\mathbb{S}^{n-2}} v \otimes v \otimes v \otimes v \,\mathrm{d}v = \frac{1}{(n-1)(n+1)} \Gamma, \tag{2.4.13}$$

where Γ is given in (2.2.28)*.*

The proof of Lemma 2.4.3 can be found in Lemma 4.1 of [47]. Thus, we skip it here.

Now, with these preliminary results, we first present the limit of f^ε as $\varepsilon \to 0$.

2.4.2 Limit for f^ε

Lemma 2.4.4 (Limit of f^ε and $\rho_{f^\varepsilon} Q_{f^\varepsilon}$)**.** *Let f^ε be the solution of Equation* (2.2.4)*. Under Assumption 2.2.8, we have that*

$$f^\varepsilon(t,x,u) \to \rho(t,x) G_{\eta(\rho)A_\Omega}(t,x) \quad \text{as } \varepsilon \to 0,$$

for any (t,x) such that $\rho(t,x) > \rho_*$, for ρ_* as given in Proposition 2.2.6. Moreover, in this same regime of (t,x), it also holds that

$$\rho_{f^\varepsilon} Q_{f^\varepsilon} \to \frac{\eta(\rho)}{\alpha} A_\Omega, \quad \text{as } \varepsilon \to 0, \tag{2.4.14}$$

where α is given in (2.2.8)*, $\eta = \eta(\rho)$ is given in* (2.2.13)*, and A_Ω is given in* (2.2.9)*.*

Proof. By Assumption 2.2.8, f^ε converges to some function f^0 as $\varepsilon \to 0$. At the same time, from Equation (2.2.6) we have that $C(f^\varepsilon) = \mathcal{O}(\varepsilon^a)$ with $a \in (0,2]$ and thus, taking the limit, $C(f^0) = 0$ as $\varepsilon \to 0$. Therefore, the limit f^0 must belong to the kernel of the operator C, which was characterized in Lemma 2.2.7. Therefore, we conclude that $f^0 = \rho(t,x) G_{\eta(\rho)A_\Omega}(t,x)$ for

any (t,x) such that $\rho(t,x) > \rho_*$ and for some $\Omega \in \mathbb{S}^{n-1}$. Finally, the limit (2.4.14) is a direct consequence of (2.2.15) in Lemma 2.2.7. ∎

2.4.3 Derivation of Equation (2.2.17a)

Integrating the kinetic equation (2.2.6) with respect to u, and using Lemma 2.4.4 in the limit $\varepsilon \to 0$, we obtain

$$\partial_t \rho + \frac{\mu\chi^2}{\alpha}\nabla_x \cdot \left(\rho \int_{\mathbb{S}^{n-1}} \left(\nabla_x \left(u \cdot (\eta(\rho)A_\Omega)u\right) G_{\eta(\rho)A_\Omega}\right) \mathrm{d}u\right) + \mu\left(\frac{\chi^2}{n} - 1\right)\nabla_x \cdot (\rho \nabla_x \rho) - D_x \Delta_x \rho = 0. \tag{2.4.15}$$

Notice that, above, we used the facts that the term in B_f vanishes and $\int_{\mathbb{S}^{n-1}} C(f^\varepsilon) du = 0$ for all $\varepsilon > 0$, both thanks to the divergence theorem.

Next, we compute the integral in the second term of (2.4.15),

$$\begin{aligned}
&\int_{\mathbb{S}^{n-1}} \nabla_x \left(\eta(\rho) u \cdot A_\Omega u\right) G_{\eta(\rho)A_\Omega} \,\mathrm{d}u \\
&\quad = \int_{\mathbb{S}^{n-1}} \nabla_x \left(\eta(\rho)\left[(u\cdot\Omega)^2 - \frac{1}{n}\right]\right) G_{\eta(\rho)A_\Omega} \,\mathrm{d}u \\
&\quad = \int_{\mathbb{S}^{n-1}} \nabla_x \eta(\rho) \left((u\cdot\Omega)^2 - \frac{1}{n}\right) G_{\eta(\rho)A_\Omega} \,\mathrm{d}u + \int_{\mathbb{S}^{n-1}} 2\eta(\rho)(u\cdot\Omega)(u\cdot\nabla_x\Omega) G_{\eta(\rho)A_\Omega} \,\mathrm{d}u \\
&\quad = \frac{n-1}{n} S_2(\eta)\, \nabla_x \eta(\rho),
\end{aligned}$$

where in the last equality we used the fact that the second integral is zero. This can be computed similarly as for the integral in Equation (2.4.5) for $k = 1$ and $w = \partial\Omega$ with $\partial\Omega \perp \Omega$ (remembering that the matrix $\nabla_x\Omega$ is such that component-wise it corresponds to $(\nabla_x\Omega)_{ij} = \partial_{x_j}\Omega_i$).

Finally, substituting this last expression into (2.4.15) and using that $\nabla_x \eta(\rho) = \eta'(\rho)\nabla_x\rho$, we can combine the terms and obtain Equation (2.2.17a) for the mass density ρ.

2.4.4 Derivation of Equation (2.2.17b).

Classically, to obtain macroscopic equations from kinetic equations, one needs to find functions $\psi = \psi(u)$ that are collision invariant for the operator C, i.e., functions ψ such that, for all f, the following holds:

$$\int_{\mathbb{S}^{n-1}} C(f)\psi(u) \,\mathrm{d}u = 0.$$

The collision invariants correspond to conserved quantities. Typically, the number of macroscopic equations we obtain is the same as the number of collision invariants. For example, in our case, if ψ is a constant, then ψ is a collision invariant, which is related to the conservation of mass. Therefore, to obtain an equation of the mean-nematic direction Ω, we would like to find its associated collision invariant(s). However, Ω does not have any associated conserved quantity, i.e., one can check that the only collision invariants for our operator C, given in (2.2.7), are the constants [41].

To overcome this difficulty, the concept of Generalized Collision Invariant (GCI) was introduced in [49] for a model of collective dynamics where the momentum is not preserved. This idea, then, has been applied to other models of collective dynamics, see, e.g., [43, 47]. Moreover, the GCI for the operator C was already computed in [41]. Next, we state the main result regarding the GCI that we will be using in the sequel. The original source [41] contains a full proof of it.

Proposition 2.4.5 (Generalized Collision Invariant defined in [41] and Proposition 9 in [41])**.** *Let*
$f\colon \mathbb{S}^{n-1} \to \mathbb{R}$ *be twice continuously differentiable such that* $Q_f \neq 0$ *and* Q_f *is the Q-tensor. Since* Q_f *is a symmetric matrix, all its eigenvalues are real. Suppose that the largest eigenvalue of* Q_f *is unique and denote* Ω_f *as the associated normalized eigenvector (which is unique up to sign). Then it holds that*

$$\int_{\mathbb{S}^{n-1}} C(f)\,\boldsymbol{\psi}_{\eta_f,\Omega_f}\,\mathrm{d}u = 0, \qquad \text{for} \qquad \boldsymbol{\psi}_{\eta_f,\Omega_f} := h_{\eta_f}(u\cdot\Omega_f)P_{\Omega_f^\perp}u,$$

where h_η *is the unique solution of*

$$-(1-r^2)^{\frac{n-1}{2}}e^{\eta r^2}(2\eta\, r^2+n-1)h_\eta + \frac{\mathrm{d}}{\mathrm{d}r}\left[(1-r^2)^{\frac{n+1}{2}}e^{\eta r^2}\frac{\mathrm{d}h}{\mathrm{d}r}\right] = r(1-r^2)^{\frac{n-1}{2}}e^{\eta r^2},$$

in the functional space

$$\mathcal{H} = \left\{ h : (-1,1)\to\mathbb{R} \;\middle|\; \int_{-1}^{1}(1-r^2)^{\frac{n-1}{2}}|h(r)|^2\,\mathrm{d}r < \infty,\ \int_{-1}^{1}(1-r^2)^{\frac{n+1}{2}}\left|h'(r)\right|^2\,\mathrm{d}r < \infty \right\}.$$

Moreover, h_η *is an odd function with* $h_\eta(r)\le 0$ *for* $r\ge 0$.

A characterization of the GCI is given by the following definition and can be found in [41]:

Definition 2.4.6. Let $(\eta,\Lambda)\in(0,\infty)\times\mathcal{U}_n^0$. Then, we define the function $\psi_{\eta\Lambda}\colon \mathbb{S}^{n-1}\to\mathbb{R}^n$ as the unique solution (in $H^1(\mathbb{S}^{n-1}) = \left\{k\in H(\mathbb{S}^{n-1}) \middle| \int_{\mathbb{S}^{n-1}} k(u)\,\mathrm{d}u = 0\right\}$) of the following equation:

$$\nabla_u\cdot(G_{\eta\Lambda}(u)\nabla_u\psi_{\eta\Lambda}) = (u\cdot\Omega_\Lambda)P_{\Omega_\Lambda^\perp}u\,G_{\eta\Lambda}(u) \qquad \forall u\in\mathbb{S}^{n-1},$$

where $\mathcal{U}_n^0$ is the set of symmetric trace-free $n\times n$-matrices whose principal eigenvalue is equal to $\frac{n-1}{n}$ and is simple.

Thanks to the GCI for the collision operator C we can now derive an equation for the mean-nematic direction Ω. Therefore, we multiply the kinetic equation given in (2.2.4) by $\psi_{\eta\Omega_f}$ and integrate with respect to u. Then, the term in C vanishes by the previous proposition. Therefore, we state the following result:

Proposition 2.4.7. *Under the assumptions of Theorem 2.2.10, it holds that*

$$\int_{\mathbb{S}^{n-1}} \mathcal{F}_u(\rho G_{\eta(\rho)A_\Omega})\boldsymbol{\psi}(u)\,\mathrm{d}u = 0, \qquad \text{for} \qquad \boldsymbol{\psi}(u) = h_{\eta(\rho)}(u\cdot\Omega)P_{\Omega^\perp}u, \tag{2.4.16}$$

where $\eta=\eta(\rho)$ *is given by* (2.2.13), $h_\eta = h_{\eta(\rho))}(u\cdot\Omega)$ *is defined in Proposition 2.4.5 and* $\mathcal{F}_u(f)$ *is defined as*

$$\mathcal{F}_u(f) = \partial_t f + \mu\chi^2 \nabla_x \cdot (\nabla_x (u^T \rho_f Q_f u) f) + \mu \left(\frac{\chi^2}{n} - 1 \right) \nabla_x \cdot ((\nabla_x \rho_f) f) - \lambda \mathbb{1}_{a=2} \nabla_u \cdot ((\nabla_u B_f) f) - D_x \Delta_x f.$$

Proof. The proof is a direct consequence of Assumption 2.2.8, Lemma 2.4.4 and Proposition 2.4.5. ∎

Limit of the Terms not Involving B_f

Now, we have all the ingredients to derive the macroscopic equation for Ω in a straightforward way. We apply Lemma 2.4.4 in the limit as $\varepsilon \to 0$ and rewrite Equation (2.4.16) as

$$I_1 + \mu\sigma I_2 + \mu \left(\frac{\chi^2}{n} - 1 \right) I_3 - \lambda \mathbb{1}_{a=2} I_4 - D_x I_5 = 0, \tag{2.4.17}$$

where

$$\begin{aligned}
I_1 &= \int_{\mathbb{S}^{n-1}} \partial_t \left(\rho G_{\eta(\rho) A_\Omega} \right) \boldsymbol{\psi}(u) \, \mathrm{d}u, \\
I_2 &= \int_{\mathbb{S}^{n-1}} \nabla_x \cdot \left(\nabla_x \left(u \cdot \eta(\rho) A_\Omega u \right) \rho G_{\eta(\rho) A_\Omega} \right) \boldsymbol{\psi}(u) \, \mathrm{d}u, \\
I_3 &= \int_{\mathbb{S}^{n-1}} \nabla_x \cdot \left((\nabla_x \rho) \, \rho G_{\eta(\rho) A_\Omega} \right) \boldsymbol{\psi}(u) \, \mathrm{d}u, \\
I_4 &= \int_{\mathbb{S}^{n-1}} \nabla_u \cdot \left(\nabla_u \left(B_{\rho G_{\eta(\rho) A_\Omega}} \right) \rho G_{\eta(\rho) A_\Omega} \right) \boldsymbol{\psi}(u) \, \mathrm{d}u, \\
I_5 &= \int_{\mathbb{S}^{n-1}} \Delta_x \left(\rho G_{\eta(\rho) A_\Omega} \right) \boldsymbol{\psi}(u) \, \mathrm{d}u.
\end{aligned}$$

Notice that while writing I_2 we used (2.2.15). In this section, we will focus only on the terms I_1, I_2, I_3 and I_5 since the term I_4 appears exclusively if we choose $a = 2$. We will compute I_4 in the next section.

Lemma 2.4.8. *The following equalities hold:*

$$\begin{aligned}
I_1 =& \frac{2\eta(\rho) c_{1,2}}{n-1} \, \rho \, \partial_t \Omega, \\
I_2 =& \frac{2\eta(\rho) c_{1,2}}{n-1} \left(2 \frac{\eta'(\rho)}{\eta(\rho)} \rho + 1 + \rho \eta'(\rho) \left(2 \frac{c_{3,2}}{c_{1,2}} - \frac{1}{n} - d_{2,0} \right) \right) (\nabla_x \rho \cdot \nabla_x) \Omega + \frac{2\eta(\rho) c_{1,2}}{n-1} \, \rho P_{\Omega^\perp} \Delta_x \Omega, \\
I_3 =& \frac{2\eta(\rho) c_{1,2}}{n-1} \, \rho (\nabla_x \rho \cdot \nabla_x) \Omega, \\
I_5 =& \frac{2\eta(\rho) c_{1,2}}{n-1} \, \rho P_{\Omega^\perp} \Delta_x \Omega + \frac{2\eta(\rho) c_{1,2}}{n-1} \, 2 \left(\rho \eta' \left(\frac{1}{\eta(\rho)} + \frac{c_{3,2}}{c_{1,2}} - d_{2,0}) \right) + 1 \right) (\nabla_x \rho \cdot \nabla_x) \Omega.
\end{aligned}$$

Proof. We start with computing I_1,

$$I_1 = \int_{\mathbb{S}^{n-1}} \partial_t (\rho G_{\eta(\rho) A_\Omega}) \boldsymbol{\psi}(u) \, \mathrm{d}u = \partial_t \rho \int_{\mathbb{S}^{n-1}} G_{\eta(\rho) A_\Omega} \boldsymbol{\psi}(u) \, \mathrm{d}u + \rho \int_{\mathbb{S}^{n-1}} \partial_t G_{\eta(\rho) A_\Omega} \boldsymbol{\psi}(u) \, \mathrm{d}u.$$

The first integral above on the last part of the equality is of the form (2.4.4) for $k = 0$, so it is

zero. The second integral is of the form (2.4.6) for $k = 0$ and so I_1 becomes

$$I_1 = \frac{2\eta(\rho)c_{1,2}(\rho)}{n-1}\ \rho\,\partial_t\Omega.$$

Next, we compute I_2,

$$\begin{aligned} I_2 &= \int_{\mathbb{S}^{n-1}} \nabla_x \cdot \left(\nabla_x \left(u \cdot \eta(\rho) A_\Omega u\right) \rho G_{\eta(\rho)A_\Omega}\right) \boldsymbol{\psi}(u)\,\mathrm{d}u \\ &= \int_{\mathbb{S}^{n-1}} \Delta_x \left(u \cdot \eta(\rho) A_\Omega u\right) \rho G_{\eta(\rho)A_\Omega} \boldsymbol{\psi}(u)\,\mathrm{d}u + \int_{\mathbb{S}^{n-1}} \nabla_x \left(u \cdot \eta(\rho) A_\Omega u\right) \cdot \nabla_x \rho\ G_{\eta(\rho)A_\Omega} \boldsymbol{\psi}(u)\,\mathrm{d}u \\ &\quad + \rho \int_{\mathbb{S}^{n-1}} \nabla_x \left(u \cdot \eta(\rho) A_\Omega u\right) \cdot \nabla_x G_{\eta(\rho)A_\Omega} \boldsymbol{\psi}(u)\,\mathrm{d}u =: I_2^1 + I_2^2 + I_2^3. \end{aligned}$$

Proceeding further, we compute each I_2^i, $i \in \{1,2,3\}$ separately. Using (2.2.9), we have

$$u \cdot \eta(\rho) A_\Omega u = \eta(\rho) \left((u \cdot \Omega)^2 - \frac{1}{n}\right).$$

The Laplacian of this expression reads

$$\begin{aligned} \Delta_x (u \cdot \eta(\rho) A_\Omega u) =& \Delta_x \eta(\rho) \left((u \cdot \Omega)^2 - \frac{1}{n}\right) + 4 \nabla_x \eta(\rho) \cdot (u \cdot \Omega)(u \cdot \nabla_x \Omega) \\ &+ 2\eta(\rho)(u \cdot \nabla_x \Omega)^2 + 2\eta(\rho)(u \cdot \Omega)(u \cdot \Delta_x \Omega). \end{aligned}$$

Subsequently, using this, we obtain

$$\begin{aligned} I_2^1 &= \int_{\mathbb{S}^{n-1}} \Delta_x \left(u \cdot \eta(\rho) A_\Omega u\right) \rho G_{\eta(\rho)A_\Omega} \boldsymbol{\psi}(u)\,\mathrm{d}u \\ &= \rho \Delta_x \eta(\rho) \int_{\mathbb{S}^{n-1}} \left((u \cdot \Omega)^2 - \frac{1}{n}\right) G_{\eta(\rho)A_\Omega} \boldsymbol{\psi}(u)\,\mathrm{d}u \\ &\quad + 4\eta'(\rho)\rho \sum_{i=1}^{n} \partial_{x_i} \rho \left(\int_{\mathbb{S}^{n-1}} (u \cdot \Omega)(u \cdot \partial_{x_i} \Omega) G_{\eta(\rho)A_\Omega} \boldsymbol{\psi}(u)\,\mathrm{d}u\right) \\ &\quad + 2\eta(\rho)\rho \int_{\mathbb{S}^{n-1}} (u \cdot \nabla_x \Omega)^2 G_{\eta(\rho)A_\Omega} \boldsymbol{\psi}(u)\,\mathrm{d}u + 2\eta(\rho)\rho \int_{\mathbb{S}^{n-1}} (u \cdot \Omega)(u \cdot \Delta_x \Omega) G_{\eta(\rho)A_\Omega} \boldsymbol{\psi}(u)\,\mathrm{d}u. \end{aligned}$$

We further simplify each integral above. The first and the third integrals are equal to zero as they are of the forms (2.4.4) for $k = 2$ and $k = 0$ and (2.4.8) for $k = 2$, respectively. The second and the forth integrals are of the form (2.4.5) with $k = 1$ (and recall (2.4.10)). Combining these we obtain

$$I_2^1 = 4\eta'(\rho)\rho \frac{c_{1,2}}{n-1} (\nabla_x \rho \cdot \nabla_x)\Omega + 2\eta(\rho)\rho \frac{c_{1,2}}{n-1} P_{\Omega^\perp} \Delta_x \Omega.$$

Next, for I_2^2 we have

$$\begin{aligned} I_2^2 &= \nabla_x \rho \cdot \int_{\mathbb{S}^{n-1}} \nabla_x \left(u \cdot \eta(\rho) A_\Omega u\right) \; G_{\eta(\rho)A_\Omega} \boldsymbol{\psi}(u) \, \mathrm{d}u \\ &= |\nabla_x \rho|^2 \eta'(\rho) \int_{\mathbb{S}^{n-1}} \left((u \cdot \Omega)^2 - \frac{1}{n}\right) \; G_{\eta(\rho)A_\Omega} \boldsymbol{\psi}(u) \, \mathrm{d}u \\ &\qquad + 2\eta(\rho) \sum_{i=1}^{n} \partial_{x_i} \rho \left(\int_{\mathbb{S}^{n-1}} (u \cdot \Omega)(u \cdot \partial_{x_i} \Omega) \; G_{\eta(\rho)A_\Omega} \boldsymbol{\psi}(u) \, \mathrm{d}u \right). \end{aligned}$$

Noticing that the first integral above is of the form (2.4.4) with $k = 2$ and $k = 0$ and the second integral is of the form (2.4.5) with $k = 1$ and recalling (2.4.10), we conclude

$$I_2^2 = 2\eta(\rho) \frac{c_{1,2}}{n-1} \left(\nabla_x \rho \cdot \nabla_x\right) \Omega.$$

Similarly, we obtain (here we additionally use (2.4.3) for $\nabla_x G_{\eta(\rho)A_\Omega}$)

$$\begin{aligned} I_2^3 &= \rho \int_{\mathbb{S}^{n-1}} \nabla_x \left(u \cdot \eta(\rho) A_\Omega u\right) \cdot \nabla_x G_{\eta(\rho)A_\Omega} \boldsymbol{\psi}(u) \, \mathrm{d}u \\ &= \rho \eta'(\rho) \sum_{i=1}^{n} \partial_{x_i} \rho \int_{\mathbb{S}^{n-1}} \left((u \cdot \Omega)^2 - \frac{1}{n}\right) \partial_{x_i} G_{\eta(\rho)A_\Omega} \boldsymbol{\psi}(u) \, \mathrm{d}u \\ &\qquad + 2\eta(\rho)\rho \int_{\mathbb{S}^{n-1}} (u \cdot \Omega) \left((u \cdot \nabla_x \Omega) \cdot \nabla_x G_{\eta(\rho)A_\Omega}\right) \boldsymbol{\psi}(u) \, \mathrm{d}u. \end{aligned}$$

The first integral above is of the form (2.4.6) for $k = 2$ and $k = 0$ (for the terms $(u \cdot \Omega)^2$ and $1/n$), respectively; and the second integral is of the form (2.4.7) for $k = 1$, therefore, we have that

$$I_2^3 = 2\rho\eta(\rho)\eta'(\rho) \left(\frac{2c_{3,2} - c_{1,2}/n - d_{2,0}c_{1,2}}{n-1} \right) \left(\nabla_x \rho \cdot \nabla_x\right) \Omega.$$

Combining these we compute I_3 analogously to obtain

$$I_3 = \int_{\mathbb{S}^{n-1}} \nabla_x \cdot \left(\left(\nabla_x \rho\right) \rho G_{\eta(\rho)A_\Omega} \right) \boldsymbol{\psi}(u) \, \mathrm{d}u = 2\rho\eta(\rho) \frac{c_{1,2}}{n-1} (\nabla_x \rho \cdot \nabla_x) \Omega.$$

Finally, for I_5 we have

$$\begin{aligned} I_5 &= \int_{\mathbb{S}^{n-1}} \Delta_x \left(\rho G_{\eta(\rho)A_\Omega} \right) \boldsymbol{\psi}(u) \, \mathrm{d}u \\ &= \Delta_x \rho \int_{\mathbb{S}^{n-1}} G_{\eta(\rho)A_\Omega} \boldsymbol{\psi}(u) \, \mathrm{d}u + 2 \sum_{j=1}^{n} \partial_{x_d} \rho \int_{\mathbb{S}^{n-1}} \partial_{x_d} G_{\eta(\rho)A_\Omega} \boldsymbol{\psi}(u) \, \mathrm{d}u \\ &\qquad + \rho \int_{\mathbb{S}^{n-1}} \Delta_x G_{\eta(\rho)A_\Omega} \boldsymbol{\psi}(u) \, \mathrm{d}u. \end{aligned}$$

The first integral above is of the form (2.4.4) for $k = 0$, so it is zero; the second integral is of the form (2.4.6) for $k = 0$; for the third integral we use (2.4.9) and that $\partial\eta = \eta'(\rho)\partial(\rho)$. Hence,

we conclude

$$I_5 = \frac{2c_{1,2}}{n-1}\eta(\rho)\,\rho P_{\Omega^\perp}\Delta_x\Omega + \frac{4}{n-1}\left(\rho\eta'[c_{1,2}+\eta(c_{3,2}-d_{2,0}c_{1,2})]+\eta(\rho)c_{1,2}\right)(\nabla_x\rho\cdot\nabla_x)\Omega.$$

This completes the proof. ∎

Limit of the Term with B_f

In this section, we compute the remaining integral I_4 in Equation (2.4.17), which includes the term B_f. First, we prove the following lemma:

Lemma 2.4.9. *Let B_f be given by (2.2.3) with $f = \rho G_{\eta(\rho)A_\Omega}$. Then the following holds*

$$\begin{aligned}\int_{\mathbb{S}^{n-1}} \nabla_u\cdot\left(\nabla_u B_{\rho G_{\eta(\rho)A_\Omega}}\ \rho G_{\eta A_\Omega}\right)\ h_\eta(u\cdot\Omega)P_{\Omega^\perp}u\,\mathrm{d}u\\ = \rho\int_{\mathbb{S}^{n-1}} B_{\rho G_{\eta(\rho)A_\Omega}}(u)\,(u\cdot\Omega)P_{\Omega^\perp}u\ G_{\eta A_\Omega}\,\mathrm{d}u.\end{aligned}$$

Proof. Applying integration by parts twice, we rewrite the integral as

$$\begin{aligned}&\int_{\mathbb{S}^{n-1}} \nabla_u\cdot(\nabla_u B_{\rho G_{\eta(\rho)A_\Omega}}\rho G_{\eta A_\Omega})h_\eta(u\cdot\Omega)P_{\Omega^\perp}u\,\mathrm{d}u\\ &\qquad = -\int_{\mathbb{S}^{n-1}}(\nabla_u B_{\rho G_{\eta(\rho)A_\Omega}}\ \rho G_{\eta A_\Omega})\cdot\nabla_u\left[h_\eta(u\cdot\Omega)P_{\Omega^\perp}u\right]\,\mathrm{d}u\\ &\qquad = \rho\int_{\mathbb{S}^{n-1}} B_{\rho G_{\eta(\rho)A_\Omega}}\nabla_u\cdot(G_{\eta A_\Omega}\nabla_u[h_\eta(u\cdot\Omega)P_{\Omega^\perp}u])\,\mathrm{d}u.\end{aligned}$$

We conclude the result since the GCI $\psi = h_\eta(u\cdot\Omega)P_{\Omega^\perp}u$ satisfies

$$\nabla_u\cdot(G_{\eta A_\Omega}\nabla_u\psi) = (u\cdot\Omega)\ P_{\Omega^\perp}u\,G_{\eta A_\Omega}$$

by Definition 2.4.6. ∎

Now, we go back to Equation (2.4.17) to rewrite I_4 using Lemma 2.4.9,

$$I_4 = \rho\int_{\mathbb{S}^{n-1}} B_{\rho G_{\eta(\rho)A_\Omega}}(u)(u\cdot\Omega)P_{\Omega^\perp}uG_{\eta A_\Omega}\,\mathrm{d}u. \tag{2.4.18}$$

First, we recast $B_{\rho G_{\eta(\rho)A_\Omega}} = [B] + [B]_{\text{even}}$, as stated in Equation (2.2.3), by expanding

$$\Sigma(u,u_2) = (\ell^2-d^2)(u\otimes u) + (\ell^2-d^2)(u_2\otimes u_2) + 2d^2\mathrm{Id}$$

and the factor $(1-\chi^2(u\cdot u_2)^2)$. Hence, we obtain

$$\begin{aligned}[B] := &\frac{(\ell^2-d^2)}{4}((u\otimes u):D_x^2)\rho - \frac{\chi^2}{4}(\ell^2-d^2)\int_{\mathbb{S}^{n-1}}(u\cdot u_2)^2((u\otimes u):D_x^2)(\rho G_{\eta(\rho)A_\Omega}(u_2))\,\mathrm{d}u_2\\ &-\frac{\chi^2}{4}(\ell^2-d^2)\int_{\mathbb{S}^{n-1}}(u\cdot u_2)^2\ ((u_2\otimes u_2):D_x^2)(\rho G_{\eta(\rho)A_\Omega}(u_2))\,\mathrm{d}u_2\\ &-\frac{\chi^2}{2}d^2\int_{\mathbb{S}^{n-1}}(u\cdot u_2)^2\Delta_x(\rho G_{\eta(\rho)A_\Omega}(u_2))\,\mathrm{d}u_2.\end{aligned}$$

and

$$[B]_{\text{even}} := \frac{(\ell^2 - d^2)}{4} \int_{\mathbb{S}^{n-1}} \left((u_2 \otimes u_2) : D_x^2\right) (\rho G_{\eta(\rho)A_\Omega}(u_2))\, \mathrm{d}u_2 + \frac{d^2}{2}\Delta_x \rho.$$

Now, using the change of variables (2.4.1) in (2.4.18), we have that

$$I_4 = \rho \int_{\mathbb{S}^{n-2}} v \int_0^\pi B_{\rho G_{\eta(\rho)A_\Omega}}(u(\theta))\, \cos\theta \sin\theta\ g_\eta(\theta)\ \sin^{d-2}\theta\, \mathrm{d}\theta\, \mathrm{d}v.$$

Notice that the terms in $[B]_{\text{even}}$ are independent of u, so they have zero contribution to I_4 (since they give an integrand odd in v). Now, we rewrite I_4 using $[B]$ and the tensor product:

$$\begin{aligned} I_4 = \rho\frac{(\ell^2 - d^2)}{4}[(H_2^r : D_x^2)]_{[2,3:1,2]}\rho - \rho\frac{\chi^2}{4}(\ell^2 - d^2)[H_4^r : (D_x^2 \otimes (\rho H_2)]_{[2,3,4,5:1,2,3,4]} \\ - \rho\frac{\chi^2}{4}(\ell^2 - d^2)[H_2^r \otimes D_x^2 : (\rho H_4)]_{[2,3,4,5:1,2,3,4]} - \rho\frac{\chi^2}{2}d^2[H_2^r : \Delta_x(\rho H_2)]_{[2,3:1,2]}, \end{aligned}$$

where in the second term above, the s-th component of the contraction is defined as

$$\left([H_4^r : (D_x \otimes (\rho H_2)]_{[2,3,4,5:1,2,3,4]}\right)_s = \sum_{i,j,k,p} (H_4^r)_{sijkp}\partial_{x_i}\partial_{x_j}\left(\rho(H_2)_{kp}\right)$$

and analogously for the other contractions; and where

$$\begin{aligned} H_2 = H_2(\eta, \Omega, \Omega^\perp) &= \int_{\mathbb{S}^{n-1}} (u \otimes u) G_{\eta A_\Omega}\, \mathrm{d}u, \\ H_2^r = H_2^r(\eta, \Omega, \Omega^\perp) &= \int_{\mathbb{S}^{n-1}} P_{\Omega^\perp} u \otimes (u \otimes u)(u \cdot \Omega) G_{\eta A_\Omega}\, \mathrm{d}u, \\ H_4 = H_4(\eta, \Omega, \Omega^\perp) &= \int_{\mathbb{S}^{n-1}} (u \otimes u \otimes u \otimes u) G_{\eta A_\Omega}\, \mathrm{d}u, \\ H_4^r = H_4^r(\eta, \Omega, \Omega^\perp) &= \int_{\mathbb{S}^{n-1}} P_{\Omega^\perp} u \otimes (u \otimes u \otimes u \otimes u)(u \cdot \Omega) G_{\eta A_\Omega}\, \mathrm{d}u. \end{aligned}$$

We can now rewrite these terms in such a way that they only depend on Ω, $\Omega^\perp$ and η.

Lemma 2.4.10 (Dimension $n = 2$)**.** *In case of only $n = 2$, we have that H_2, H_2^r, H_4, H_4^r correspond to expressions* (2.2.22)*,* (2.2.23)*,* (2.2.24) *and* (2.2.25)*, respectively.*

The proof of this lemma is based on the change of variables (2.4.1) for $n = 2$, i.e., $u = \cos\theta\Omega + \sin\theta\Omega^\perp$, and the same type of argument as in the proof of Lemma 2.4.2. Thus, we skip it here.

We conclude this section by computing the values of H_2, H_2^r, H_4, H_4^r in dimension $n \geq 3$:

Proof of Proposition 2.2.11. For this proof, we consider the decomposition of $u \in \mathbb{S}^{n-1}$ into

$$u = u_\parallel + u_\perp, \qquad u_\parallel := P_\Omega u = (u \cdot \Omega)\Omega, \quad u_\perp := P_{\Omega^\perp} u,$$

and the change of variables given in (2.4.1) where we have that

$$(u \cdot \Omega) = \cos\theta, \qquad P_{\Omega^\perp} u = \sin\theta v.$$

Then, the proof of this lemma closely the proof of Lemma 4.1 in [47]. There, the authors prove that,

$$\mathcal{A}_{ij} := \int_{\mathbb{S}^{n-1}} \phi(u\cdot\Omega)(u_\perp)_i(u_\perp)_j \,\mathrm{d}u = \frac{1}{n-1}\left(\int_{\mathbb{S}^{n-1}} \phi(u\cdot\Omega)(1-(u\cdot\Omega)^2)\,\mathrm{d}u\right)(P_{\Omega^\perp})_{ij} \tag{2.4.19}$$

where $\phi = \phi(u\cdot\Omega)$ is a given function. The authors also consider

$$S_{ijkl} := \int_{\mathbb{S}^{n-1}} \phi(u\cdot\Omega)(u_\perp)_i(u_\perp)_j(u_\perp)_k(u_\perp)_l \,\mathrm{d}u.$$

and we additionally define

$$C_S := \frac{1}{(n-1)(n+1)}\int_{\mathbb{S}^{n-1}} \phi(u\cdot\Omega)(1-(u\cdot\Omega)^2)^2\,\mathrm{d}u.$$

Notice that the only non-zero terms correspond to

$$S_{iiii} = 3C_S\Gamma_{iiii}, \quad S_{iijj} = C_S\Gamma_{iijj}, \quad S_{ijij} = C_S\Gamma_{ijij}, \quad S_{ijji} = C_S\Gamma_{ijji},$$

where Γ is given in (2.2.28) and $i,j\in\{1,...,n\}$ such that $i\neq j$. With this we are ready to carry out the proof.

The equality for H_2 in (2.2.26) is obtained by proceeding similarly as in the proof of Lemma 2.4.2 and using (2.4.12).

Next, we look at H_2^r to prove (2.2.27). We have that

$$\begin{aligned} H_2^r &= \int_{\mathbb{S}^{n-1}} u_\perp\otimes(u_\perp\otimes u_\parallel)(u\cdot\Omega)G_{\eta(\rho)A_\Omega}\,\mathrm{d}u + \int_{\mathbb{S}^{n-1}} u_\perp\otimes(u_\parallel\otimes u_\perp)(u\cdot\Omega)G_{\eta(\rho)A_\Omega}\,\mathrm{d}u \\ &= \frac{d_{2,2}}{n-1}P_{\Omega^\perp}\Omega + R_2^r. \end{aligned}$$

with $d_{2,2}$ given in Equation (2.2.20).

In the first equality above, the integrands that are odd in $u_\perp$ vanish (analogously to what happens when performing the change of variables (2.4.1): the terms that are odd in v vanish). In the second equality, for the first integral we used (2.4.12) and for the second integral we define

$$\begin{aligned} (R_2^r)_{ijk} &= \int_{\mathbb{S}^{n-1}} (u_\perp)_i(u_\parallel)_j(u_\perp)_k(u\cdot\Omega)G_{\eta(\rho)A_\Omega}\,\mathrm{d}u = \Omega_j\int(u_\perp)_i(u_\perp)_k(u\cdot\Omega)^2G_{\eta(\rho)A_\Omega}\,\mathrm{d}u \\ &= \Omega_j\mathcal{A}_{ik} = \Omega_j\frac{d_{2,2}}{n-1}(P_{\Omega^\perp})_{ik}, \end{aligned}$$

where in the definition of $\mathcal{A}$ we used $\phi(u\cdot\Omega) = (u\cdot\Omega)^2G_{\eta(\rho)A_\Omega}$.

Now consider

$$([P_{\Omega^\perp}\otimes\Omega\otimes P_{\Omega^\perp}]_{:24})_{ijk} = \sum_{p=1}^{n}(P_{\Omega^\perp})_{ip}\Omega_j(P_{\Omega^\perp})_{pk} = \Omega_j(P_{\Omega^\perp})_{ik},$$

where the second equality is a straightforward computation. Therefore, we conclude that

$$R_2^r = \frac{d_{2,2}}{n-1}[P_{\Omega^\perp}\otimes\Omega\otimes P_{\Omega^\perp}]_{:24}.$$

We proceed by focusing on H_4 and expanding it:

$$\begin{aligned}H_4 &= \int_{\mathbb{S}^{n-1}} (u_\perp \otimes u_\perp \otimes u_\perp \otimes u_\perp) G_{\eta(\rho)A_\Omega}\,\mathrm{d}u + \int_{\mathbb{S}^{n-1}} (u_\perp \otimes u_\perp \otimes u_\parallel \otimes u_\parallel) G_{\eta(\rho)A_\Omega}\,\mathrm{d}u \\ &+ \int_{\mathbb{S}^{n-1}} (u_\parallel \otimes u_\parallel \otimes u_\perp \otimes u_\perp) G_{\eta(\rho)A_\Omega}\,\mathrm{d}u + \int_{\mathbb{S}^{n-1}} (u_\parallel \otimes u_\perp \otimes u_\perp \otimes u_\parallel) G_{\eta(\rho)A_\Omega}\,\mathrm{d}u \\ &+ \int_{\mathbb{S}^{n-1}} (u_\perp \otimes u_\parallel \otimes u_\perp \otimes u_\parallel) G_{\eta(\rho)A_\Omega}\,\mathrm{d}u + \int_{\mathbb{S}^{n-1}} (u_\perp \otimes u_\parallel \otimes u_\parallel \otimes u_\perp) G_{\eta(\rho)A_\Omega}\,\mathrm{d}u \\ &+ \int_{\mathbb{S}^{n-1}} (u_\parallel \otimes u_\perp \otimes u_\parallel \otimes u_\perp) G_{\eta(\rho)A_\Omega}\,\mathrm{d}u + \int_{\mathbb{S}^{n-1}} (u_\parallel \otimes u_\parallel \otimes u_\parallel \otimes u_\parallel) G_{\eta(\rho)A_\Omega}\,\mathrm{d}u \\ &=: D_1 + D_2 + D_3 + \ldots + D_8,\end{aligned}$$

where all the terms odd in $u_\perp$ vanished. Considering the change of variables (2.4.1), we deduce from (2.4.13) that

$$D_1 = d_{0,4}\frac{1}{(n-1)(n+1)}\Gamma.$$

From (2.4.12), (2.4.19) and proceeding as before, we have that

$$D_2 = \frac{d_{2,2}}{n-1} P_{\Omega^\perp} \otimes \Omega \otimes \Omega, \qquad D_3 = \frac{d_{2,2}}{n-1} \Omega \otimes \Omega \otimes P_{\Omega^\perp}, \qquad D_4 = \frac{d_{2,2}}{n-1} \Omega \otimes P_{\Omega^\perp} \otimes \Omega.$$

Furthermore, proceeding as in the computation for R_2^r we obtain

$$D_5 = \frac{d_{2,2}}{n-1}[P_{\Omega^\perp} \otimes \Omega \otimes P_{\Omega^\perp} \otimes \Omega]_{:24}, \qquad D_6 = \frac{d_{2,2}}{n-1}[P_{\Omega^\perp} \otimes \Omega \otimes \Omega \otimes P_{\Omega^\perp}]_{:25},$$

$$D_7 = \frac{d_{2,2}}{n-1}[\Omega \otimes P_{\Omega^\perp} \otimes \Omega \otimes P_{\Omega^\perp}]_{:35}.$$

By applying the change of variables (2.4.1) to the last term we directly have that

$$D_8 = d_{4,0}\,\Omega \otimes \Omega \otimes \Omega \otimes \Omega$$

Finally, we split H_4^r into

$$H_4^r = D_9 + D_{10},$$

with

$$\begin{aligned}D_9 = &\int_{\mathbb{S}^{n-1}} \big(u_\perp \otimes (u_\perp \otimes u_\perp \otimes u_\perp \otimes u_\parallel)(u\cdot\Omega) + u_\perp \otimes (u_\perp \otimes u_\perp \otimes u_\parallel \otimes u_\perp)(u\cdot\Omega)\big) G_{\eta(\rho)A_\Omega}\,\mathrm{d}u \\ &+ \int_{\mathbb{S}^{n-1}} \big(u_\perp \otimes (u_\perp \otimes u_\parallel \otimes u_\perp \otimes u_\perp)(u\cdot\Omega) + u_\perp \otimes (u_\parallel \otimes u_\perp \otimes u_\perp \otimes u_\perp)(u\cdot\Omega)\big) G_{\eta(\rho)A_\Omega}\,\mathrm{d}u,\end{aligned}$$

and

$$\begin{aligned}D_{10} = &\int_{\mathbb{S}^{n-1}} \big(u_\perp \otimes (u_\perp \otimes u_\parallel \otimes u_\parallel \otimes u_\parallel)(u\cdot\Omega) + u_\perp \otimes (u_\parallel \otimes u_\perp \otimes u_\parallel \otimes u_\parallel)(u\cdot\Omega)\big) G_{\eta(\rho)A_\Omega}\,\mathrm{d}u \\ &+ \int_{\mathbb{S}^{n-1}} \big(u_\perp \otimes (u_\parallel \otimes u_\parallel \otimes u_\perp \otimes u_\parallel)(u\cdot\Omega) + u_\perp \otimes (u_\parallel \otimes u_\parallel \otimes u_\parallel \otimes u_\perp)(u\cdot\Omega)\big) G_{\eta(\rho)A_\Omega}\,\mathrm{d}u,\end{aligned}$$

where the terms odd in $u_\perp$ vanished. Proceeding as in the computation of R_2^r we have that

$$D_{10} = \frac{d_{4,2}}{n-1}\Big(P_{\Omega^\perp}\otimes\Omega\otimes\Omega\otimes\Omega + [P_{\Omega^\perp}\otimes\Omega\otimes P_{\Omega^\perp}\otimes\Omega\otimes\Omega]_{:24} \\ + [P_{\Omega^\perp}\otimes\Omega\otimes\Omega\otimes P_{\Omega^\perp}\otimes\Omega]_{:25} + [P_{\Omega^\perp}\otimes\Omega\otimes\Omega\otimes\Omega\otimes P_{\Omega^\perp}]_{:26}\Big).$$

To compute D_9, we consider the second component in the first integral as an example. This integral is a 5-tensor. We apply $u_\parallel = (u\cdot\Omega)\Omega$ and look at the components i,j,k,l,m

$$\Big(\int_{\mathbb{S}^{n-1}} u_\perp\otimes(u_\perp\otimes u_\perp\otimes\Omega\otimes u_\perp)(u\cdot\Omega)^2 G_{\eta(\rho)A_\Omega}\,\mathrm{d}u\Big)_{ijklm} \\ = \int_{\mathbb{S}^{n-1}} (u_\perp)_i(u_\perp)_j(u_\perp)_k\Omega_l(u_\perp)_m(u\cdot\Omega)^2 G_{\eta(\rho)A_\Omega}\,\mathrm{d}u = \Omega_l S_{ijkm},$$

where in the definition of S_{ijkm} we have $\phi(u\cdot\Omega) = (u\cdot\Omega)^2 G_{\eta(\rho)A_\Omega}$, which in this case means that $C_S = d_{2,4}$. Putting all the terms of D_9 together and by considering all the combinations of indices we have that

$$D_9 = \frac{d_{2,4}}{(n-1)(n+1)}T,$$

with T given in (2.2.29). This completes the proof. ∎

2.5 Conclusions

In this article, we have explored the effects of an anisotropic repulsive potential on inert particles. We derived both kinetic (2.2.4) and macroscopic equations (2.2.17a)-(2.2.17b) and discussed potential interpretations of the latter. The equation for the particle density ρ is independent of the particles' mean-nematic direction Ω. However, the anisotropy of the particles slows down the non-linear diffusion of the particle density ρ. In contrast, the equation for Ω is more complex and challenging to interpret. It consists of transport and diffusion terms, resulting from the effect of the repulsive potential on the particles' position. Additionally, the repulsive potential acting on the particles' direction creates a complex, diffusive-type operator with different signs for oblate and prolate particles.

Many models for collective dynamics impose an alignment force directly on particle directions. Our main goal in this article was to observe the nematic alignment and the spatial effects of the anisotropic Gaussian-type repulsive potential on the particle dynamics without imposing the alignment directly.

However, when we derived this effect directly from an anisotropic repulsive potential, we observed intriguing phenomena. For instance, we can understand how particle anisotropy influences the evolution of particle density, how particle positions affect their directions, and what the impact of the specific interaction potential considered on the directions is (through the term B_f).

The well-posedness of these equations will be the object of future studies, along with the consideration of other types of anisotropic repulsive potentials, such as generalizations of the Lennard-Jones potential. Another interesting aspect for future research is the study of compactly supported potentials, which may better represent contact interactions.

Acknowledgements

The authors would like to thank Pierre Degond for wonderful and fruitful discussions.

The work of SMA and CW was funded in part by the Austrian Science Fund (FWF) project 10.55776/F65 and in part by the Vienna Science and Technology Fund (WWTF) [10.47379/VRG17014]. CW was funded partly by the Austrian Science Fund (FWF) **W1261-B28**. SP is supported by the KAKENHI Grant-in-Aid for Early-Career Scientists (Grant number 24K16962). HY is supported by the Dutch Research Council (NWO) under the NWO-Talent Programme Veni ENW project MetaMathBio with the project number VI.Veni.222.288. This research was completed while HY was visiting the Okinawa Institute of Science and Technology (OIST) through the Theoretical Sciences Visiting Program (TSVP). SP gratefully acknowledges the hospitality of the TSVP during his stay at OIST.

2.6 Appendix

2.6.1 Proof of Lemma 2.2.1

Proof. Considering the scaling $\ell = \varepsilon\ell'$ and $d = \varepsilon d'$ and a change of variable $z = \frac{x_2 - x_1}{\varepsilon}$, so $\varepsilon^n \,\mathrm{d}z = \mathrm{d}x_2$, we obtain

$$\begin{aligned} V_f(t, x_1, u_1) &= \int_{\mathbb{S}^{n-1}} \int_{\mathbb{R}^n} V_{b_{\mathrm{WG}}}\left(u_1, u_2, \frac{x_2 - x_1}{\varepsilon}\right) f^\varepsilon(t, x_2, u_2)\,\mathrm{d}x_2\,\mathrm{d}u_2 \\ &= \varepsilon^n \int_{\mathbb{S}^{n-1}} \int_{\mathbb{R}^n} V_{b_{\mathrm{WG}}}(u_1, u_2, z)\, f^\varepsilon(t, x_1 + \varepsilon z, u_2)\,\mathrm{d}z\,\mathrm{d}u_2. \end{aligned}$$

Now, we perform a Taylor expansion of $f^\varepsilon(t, \cdot, u_2)$ at x_1 to obtain

$$f^\varepsilon(t, x_1 + \varepsilon z, u_2) = f^\varepsilon(t, x_1, u_2) + \varepsilon z \cdot \nabla_x f^\varepsilon(t, x_1, u_2) + \frac{1}{2}\varepsilon^2 z^T \,\mathrm{D}_x^2 f^\varepsilon(t, x_1, u_2) \cdot z + \mathcal{O}(\varepsilon^3).$$

Since, we consider the weighted Gaussian potential $V_{b_{\mathrm{WG}}}$, as defined in Equation (2.1.6), we use $\int_{\mathbb{R}^n} z V_{b_{\mathrm{WG}}}(u_1, u_2, z)\,\mathrm{d}z = 0$, and thus for the potential $V_f(t, x_1, u_1)$, we have that

$$\begin{aligned} V_f(t, x_1, u_1) =& \varepsilon^n \int_{\mathbb{S}^{n-1}} \left(\int_{\mathbb{R}^n} V_{b_{\mathrm{WG}}}(u_1, u_2, z)\,\mathrm{d}z \right) f^\varepsilon(t, x_1, u_2)\,\mathrm{d}u_2 \\ &+ \frac{\varepsilon^{n+2}}{2} \int_{\mathbb{S}^{n-1}} \int_{\mathbb{R}^n} V_{b_{\mathrm{WG}}}(u_1, u_2, z) z^T \,\mathrm{D}_x^2 f^\varepsilon(t, x_1, u_2) \cdot z\,\mathrm{d}z\,\mathrm{d}u_2 + \mathcal{O}(\varepsilon^{n+3}). \end{aligned}$$

Notice that with the scaling factor (2.1.5) we have for the potential $V_{b_{\mathrm{WG}}}$,

$$\begin{aligned} \int_{\mathbb{R}^n} V_{b_{\mathrm{WG}}}(u_1, u_2, z)\,\mathrm{d}z &= b_{\mathrm{WG}}^2(u_1, u_2), \\ \int_{\mathbb{R}^n} (z \otimes z) V_{b_{\mathrm{WG}}}(u_1, u_2, z)\,\mathrm{d}z &= \frac{1}{2} b_{\mathrm{WG}}^2(u_1, u_2)\Sigma. \end{aligned} \tag{2.6.1}$$

Using (2.6.1), we obtain

$$V_f(t,x_1,u_1) = \varepsilon^n \int_{\mathbb{S}^{n-1}} \left(1-\chi^2(u_1\cdot u_2)^2\right) f(t,x_1,u_2)\,\mathrm{d}u_2 + \frac{\varepsilon^{n+2}}{4}\int_{\mathbb{S}^{n-1}} \left(1-\chi^2(u_1\cdot u_2)^2\right)\Sigma(u_1,u_2):\mathrm{D}_x^2 f(t,x_1,u_2)\,\mathrm{d}u_2 + \mathcal{O}(\varepsilon^{n+3}).$$

Then,

$$V_f^\varepsilon(t,x_1,u_1) = \frac{1}{\varepsilon^n}V_f(t,x_1,u_1) = W_f(t,x_1,u_1) + \varepsilon^2 B_f(t,x_1,u_1) + \mathcal{O}(\varepsilon^3).$$

where W_f and B_f are Equations (2.2.2) and (2.2.3) in the lemma. ∎

2.6.2 Proof of Lemma 2.4.2

Proof. We will consider the change of variables given in (2.4.1) throughout the following proof and thus we can recast

$$\begin{aligned}\boldsymbol{\psi}(u) &= h_\eta(\cos\theta)\sin\theta\, v,\\ G_{\eta(\rho)A_\Omega}(u) &= g_\eta(\theta),\end{aligned}$$

where $g_\eta(\theta)$ is given in (2.4.2).

To begin with, doing the change of variables (2.4.1), the integral (2.4.4) corresponds to

$$\int_{\mathbb{S}^{n-1}} (u\cdot\Omega)^k\, G_{\eta(\rho)A_\Omega}\boldsymbol{\psi}(u)\;\mathrm{d}u = c_{k,1}\left(\int_{S^{n-2}} v\;\mathrm{d}v\right).$$

The integral in v is zero since the integrand is odd. Moreover, the function $c_{k,p}$ is defined in (2.2.19).

Proceeding similarly, we consider (2.4.12) and transform (2.4.5) into

$$\int_{\mathbb{S}^{n-1}} (u\cdot w)(u\cdot\Omega)^k\, G_{\eta(\rho)A_\Omega}\boldsymbol{\psi}(u)\;\mathrm{d}u = c_{k,2}\left(\int_{\mathbb{S}^{n-2}} v\otimes v\;\mathrm{d}v\right)w = \frac{c_{k,2}}{n-1}P_{\Omega^\perp}w.$$

Now, the integral (2.4.6) is computed analogously, since we know the value of $\partial G_{\eta(\rho)A_\Omega}$ from Lemma 2.4.1 and using that $P_{\Omega^\perp}\partial\Omega = \partial\Omega$.

Integral (2.4.7) is also computed analogously using relation (2.4.11).

Moreover, considering (2.4.11) we recast integral (2.4.8) as

$$\int_{\mathbb{S}^{n-1}} (u\cdot\Omega)^{2k}(u\cdot w)^2\, G_{\eta(\rho)A_\Omega}\boldsymbol{\psi}(u)\;\mathrm{d}u = 2(\Omega\cdot w)c_{2k+1,1}\left(\int_{S^{n-2}} v\otimes v\;\mathrm{d}v\right)w,$$

and since $w\perp\Omega$ the integral vanishes.

Finally, the integral (2.4.9) is computed in the same way as above using the corresponding expression for $\partial^2 G_{\eta(\rho)A_\Omega}$ provided in Lemma 2.4.1. ∎

2.6.3 Numerical Approximation of $K(\eta)$ and Additional Figures

In the following, we outline the method we use to approximate the diffusion parameter $K(\eta)$ in Figures 2.3 and 2.10c. One can approximate $S_2(\eta)$ via applying numerical quadrature such as the adaptive Gauss–Kronrod quadrature to (2.2.12), we refer to this approximation as $\tilde{S}_2$. Next, the function $\eta(\rho)$ can be interpolated by computing $\tilde{S}_2(\eta_j)$ at equidistant points $\eta_j = \frac{C(1-\chi^2)j}{m}$ for $1 \leq j \leq m$ where m is the number of interpolation points and $C > 0$ is a large enough constant. Using these points, one can define $\tilde{\eta}$ as the Akima interpolation of $\left(\frac{\eta_j}{\alpha \tilde{S}_2(\eta_j)}, \eta_j\right)$. The regularization effect of the Akima interpolation is useful to counter numerical instabilities for small values of η close to the unknown η^*. Finally, to approximate K, we evaluate

$$\tilde{K}(\rho) \coloneqq 1 - \frac{\chi^2}{n} - \sigma \frac{n-1}{n} \tilde{S}_2(\tilde{\eta}(\rho))\tilde{\eta}'(\rho)$$

where the derivative $\tilde{\eta}'$ is the derivative of the Akima interpolant.

We finish the appendices with some additional figures from our numerical experiments.

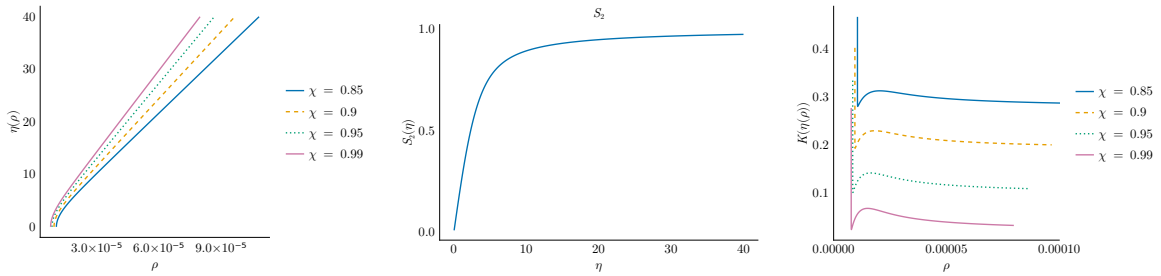

(a) $\eta(\rho)$ with respect to ρ. (b) $S_2(\eta)$ with respect to η. (c) $K(\eta)$ with respect to ρ.

Figure 2.10: (a) Plots of $\eta(\rho)$ with respect to ρ, for different χ values corresponding to different colors. Notice that η is non-decreasing with respect to ρ. (b) A plot of $S_2(\eta)$ versus η. (c) Evolution of the diffusion coefficient K with respect to the particle density ρ. Different colors correspond to different χ values.

3 A Spectral-Based Method for Network-Formation PDEs

This chapter contains a manuscript in preparation for submission of results of an ongoing collaboration with Pedro Aceves Sanchez, Pierre Degond and Sara Merino Aceituno.

Contents

Abstract

We propose and study a simple and scalable Fourier-based spectral method for a continuum model of network formation under periodic boundary conditions. The model provides the evolution of the pressure p and the conductivity m over time. The evolution of p is given by an anisotropic Poisson equation, while the equation for m contains three terms corresponding to a diffusion and an activation term of the network – that depends on the gradient of the pressure – as well as a relaxation term that acts as a decaying term. This system arises as a formal

L^2-gradient flow of a non-convex energy functional. Our algorithm combines two ingredients: (i) a splitting method for the equation for m, where the activation and relaxation parts are solved analytically, and the diffusion part is solved via Fast Fourier Transform (FFT), and (ii) an FFT combined with the Conjugate Gradient (CG) method applied to the equation for the pressure. This makes the scheme easy to implement compared to implicit schemes and naturally extensible to three dimensions on uniform periodic grids. To showcase the method, we recover the previously documented influence of the activation strength c, the diffusion coefficient D, and the metabolic exponent γ on the morphology of emergent networks, and report grid convergence results.

3.1 Introduction

3.1.1 PDE System for Network Formation

Biological transportation networks are characterised by their ability to efficiently balance cost, efficiency and resilience [16, 35]. Such networks are fundamental processes and occur in various contexts, such as leaf venation in plants [35, 85], blood circulation in mammals [94], and the transport of electric charge in neural networks [55, 87]. Therefore, understanding these networks and the underlying mechanisms of their evolution is of great interest. Consequently, the aim of comprehending the emergence, formation, and adaptation of such networks has inspired many mathematical approaches to model these phenomena, ranging from discrete graph-based descriptions [12, 16, 78] to continuum models based on partial differential equations (PDEs) [79].

In this paper, we focus on a PDE model describing network formation in porous media first introduced in [77]. Particularly, we will propose a numerical method that is simpler compared to those proposed previously in the literature and that has the potential to be extended to three dimensions. The model describes the change of pressure $p = p(t, x, y) \in \mathbb{R}$ and conductivity $m = m(t, x, y) \in \mathbb{R}^2$ over the space variables $x, y \in \mathbb{R}$ and time $t \in [0, \infty)$. We have

$$-\nabla \cdot [((m \otimes m) + r\mathrm{Id})\, \nabla p] = S, \tag{3.1.1a}$$

$$\partial_t m - D^2 \Delta m - c^2 (m \cdot \nabla p) \nabla p + |m|^{2(\gamma-1)} m = 0, \tag{3.1.1b}$$

where the tensor product $\otimes$ is defined as $m \otimes m := (m_i m_j)_{i,j\in\{1,2\}}$, $r(x, y) \geq r_0 > 0$ is the isotropic background permeability of the medium, $\gamma \in \mathbb{R}$ is the metabolic exponent, $D > 0$ is the diffusive constant and $c > 0$ is the activation parameter. Furthermore, Id denotes the (2×2)- identity matrix and S represents the sources and sinks in the medium. In the sequel, we assume periodic boundary conditions for p and m and time-independent $S = S(x, y)$, with $\int_{\mathbb{R}^2} S(x, y)\, \mathrm{d}x\, \mathrm{d}y = 0$ where the integral is in the whole domain, since it is a solvability condition for (3.1.1a).

Note that for the following numerical experiments in Section 3.5, we will consider the model to be described on a rectangular domain Ω with periodic boundary conditions.

Meaning of the equations. In the elliptic equation for the pressure p (3.1.1a), the term $(m \otimes m + r\mathrm{Id})$ gives a permeability tensor depending on space (x, y) and time t. This elliptic equation actually arises by combining the quasi-incompressibility of the fluid with Darcy's law. Darcy's law links the velocity u and the pressure p of a fluid in a porous medium in the form

$$u(t, x, y) = -K(t, x, y) \nabla p(t, x, y), \tag{3.1.2}$$

where $K(t,x,y)$ is the conductivity of the medium, in our case $K(t,x,y) = (m \otimes m + r\mathrm{Id})$. Now, assuming the quasi-incompressibility of the fluid and the conservation of mass, we have

$$\nabla \cdot u(t,x,y) = S(x,y). \tag{3.1.3}$$

Substituting Darcy's law (3.1.2) into relation (3.1.3) leads to the equation for the pressure (3.1.1a).

Additionally, note that the principal directions of the conductivity tensor $(m \otimes m + r\mathrm{Id})$ are given by $m/|m|$ and $m^{\perp}$ with corresponding eigenvalues $r(x)+|m|^2$ and $r(x)$, respectively. This can also be interpreted as an increase of the principal permeability by $|m|^2$ in the direction of the conductivity m while the flow only 'feels' the background permeability $r(x)$ in the direction of $m^{\perp}$.

Furthermore, equation (3.1.1b) is a parabolic reaction-diffusion equation which governs the evolution of the network conductivity m. It consists of the diffusive term $D^2\Delta m$ that accounts for random effects in the network; the activation term $c^2(m \cdot \nabla p)\nabla p$ that acts as a pumping term and thus the driving force to extend the network in the direction of the pressure gradient ∇p; lastly, the algebraic relaxation term $|m|^{2(\gamma-1)}m$ acts as a decaying term and represents the functional derivative of the metabolic cost required to sustain the network.

The system for the pressure p and the conductivity m (3.1.1a)–(3.1.1b) is coupled, non-local, and it can be interpreted as the formal L^2-gradient flow induced by the energy functional $\mathcal{E}[m]$, given by

$$\mathcal{E}[m] := \frac{1}{2}\int_{\Omega}\left(D^2|\nabla m|^2 + \frac{|m|^{2\gamma}}{\gamma} + c^2(m\cdot\nabla p[m])^2 + c^2 r(x)|\nabla p[m]|^2\right)\mathrm{d}x, \tag{3.1.4}$$

which is highly non-convex [67, 68]. Here, $p[m] \in H^1(\Omega)$ denotes the unique solution of the Poisson equation (3.1.1a) corresponding to a given conductivity m, under periodic boundary conditions. The first and second terms in (3.1.4) represent the diffusion and relaxation energies, respectively, while the last two terms describe the energy associated with the interaction between the network and the fluid flow. In [67], the authors proved that the energy functional is non-increasing along smooth solutions and that for weak solutions, the following energy dissipation inequality holds:

$$\mathcal{E}[m(t)] \le \mathcal{E}[m(0)] \qquad \text{for all } t \ge 0.$$

The system (3.1.1a)-(3.1.1b) was derived from a discrete-graph model introduced by Hu and Cai [78], which describes the evolution of conductivities on graphs subject to Kirchhoff's law and energy minimisation principles. Both approaches, the discrete (e.g., [64, 69, 78]) and the continuous (e.g., [2,3,9,67,79]) one, as well as connections between these (e.g., [27,65,66]), have been extensively studied resulting in a variety of analytical results on e.g., existence of solutions, stability and steady states, a rigorous continuum limit of the discrete model as well as numerical investigations illustrating arising network patterns.

3.1.2 Contributions and Scope

We propose a Fourier-based spectral algorithm for system (3.1.1) on periodic domains that is: (i) simple to implement (no assembly or inversion of large sparse matrices), (ii) high-order accurate in space, and (iii) naturally extensible to 3D uniform grids. The third point is particularly important when it comes to applications, as many biological networks, such as vascularisation, occur in three dimensions.

Across the literature, system (3.1.1) has been discretised using mixed/standard finite elements and finite differences, paired with time integrators tailored to stiffness: mixed finite elements in space with an implicit–explicit first-order Euler scheme and adaptive time stepping (and Dirichlet/Neumann boundary conditions) in [68]; finite elements with Crank–Nicolson for diffusion, explicit treatment of the remaining terms, and very small time steps to ensure energy decay in [2]; operator splitting for the conductivity equation combining explicit Euler (activation), implicit Euler with bisection (relaxation), and exact diffusion, plus a preconditioned GMRES solver for the pressure in [3]; fully implicit second-order and semi-implicit first-order energy-decaying schemes with a Conjugate Gradient solver for the Poisson equation in [56]; ADI (alternating direction implicit method) and symmetric ADI schemes on uniform Cartesian grids for the tensor model in [9, 10]; and low-order finite elements with semi-implicit backward Euler time stepping and Richardson extrapolation with accuracy assessment in [8]. We expand on this literature in Section 3.3.

This extensive and varied literature is due to the challenges in simulating system (3.1.1): the non-linear nature of the system; the degeneracy for $D = 0$; the stiffness and ill-conditioning issues – for larger values of the background conductivity r the stiffness increases, but as $r \to 0$ the problem becomes ill-conditioned (particularly, for fully implicit 2D solvers). Moreover, it has been reported that the solutions are very sensitive to the parameters γ, D, r and spatial mesh sizes. Our method is not unconditionally energy-stable and inherits a time-step restriction from the activation subdynamics. Nonetheless, in the periodic setting, it delivers accurate and scalable simulations using FFTs, providing a practical computational tool that can complement implicit and energy-decaying schemes.

3.1.3 Structure of this Paper

In Section 3.2, we review recent advances for system (3.1.1) and related models. Next, we focus on the literature on numerical methods for system (3.1.1) in Section 3.3. Details of the proposed numerical method are given in Section 3.4. Section 3.5 presents numerical experiments and parameter studies, and Section 3.6 reports grid convergence results. Section 3.7 provides conclusions and outlines directions for future work.

3.2 Background and Related Work

3.2.1 Analytical Results on the Network System

The system of equations (3.1.1) presented above has been extensively studied analytically and numerically in a wide range of works [2, 3, 8–10, 56, 65–70, 79]. In the following, we provide a concise overview of the main analytic results.

- **Existence and uniqueness of solutions.** The existence of global weak solutions in the energy space of system (3.1.1) with $r = 1$ has been studied for $\gamma \geq 1$ in [67], with $r = r(x) > r_0 > 0$ for $\frac{1}{2} \leq \gamma < 1$ in [68] and additionally for $\gamma \geq \frac{1}{2}$ in [3]. Moreover, the existence and uniqueness of local (global for the one-dimensional case) in time mild solutions of system (3.1.1a)-(3.1.1) has been proven in [67] for $r = 1$ and $\gamma \geq 1$ and extended for general $r = r(x) > r_0 > 0$ and $\frac{1}{2} < \gamma < 1$ in [68] and for $\gamma > \frac{1}{2}$ in [3]. Furthermore, Albi et al. [2] explored the possible existence of singular limit solutions with respect to the parameters of the model.
  Additionally, for the corresponding PDE model, where only non-negative diagonal tensor fields $c(x) \in \mathbb{R}^d$ for the conductivity instead of the vector-valued conductivities m were

taken into account, its global existence of weak solutions was investigated by [66]. Furthermore, in [70] the authors were considering a more general tensor PDE model, which was not only restricted to rank-one tensors but rather to tensors $\mathbb{C} \in \mathbb{R}^{d\times d}$ with $d \leq 3$. This model also considered a more general metabolic cost function for the relaxation term. For this system, the authors proved under certain assumptions on the metabolic cost functional (resulting in a convex energy functional) the existence and uniqueness of global weak solutions.

- **Steady states and stability.** For the above presented system (3.1.1), the long-term behaviour of solutions and thus their stability with respect to the diffusivity constant D have been studied in [67] for $r = 1$ and in [68] for $r = r(x) > r_0 > 0$. In this context, Haskovec et al. [67] have shown that for a large diffusivity constant D, the zero-steady state is stable. Conversely, for small D, the zero-steady state is Turing unstable, and thus network patterns occur. Moreover, they performed a non-linear stability analysis of the system for $D = 0$ in the one-dimensional setting first only for $\gamma \geq 1$ and $r = 1$ and Haskovec et al. [68] and Albi et al. [3] later extended it to $\gamma \geq \frac{1}{2}$ and $r = r(x) > r_0 > 0$. In the multi-dimensional setting, Haskovec et al. [67] achieved constructing pointwise stationary solutions in the case of $\gamma > 1$ and $D = 0$, which was extended to $\frac{1}{2} \leq \gamma \leq 1$ and $D = 0$ in [68].
  For the tensor PDE model, the steady states of the system were analysed for the one- and multi-dimensional settings in [70]. For $D > 0$, the authors prove the existence (for a non-negative and continuous metabolic cost functional) and even uniqueness (for a strictly convex energy functional) of steady states. In the case of $D = 0$, they obtain the existence and uniqueness of a weak solution for $\gamma > 1$. For the one-dimensional case with $D = 0$ and $\gamma \in (0, 1)$, a more detailed analysis of the steady states and their stability has been discussed.

- **Other analytical results:** In [67], it has been proven that the energy functional (3.1.4) is non-increasing along smooth solutions. Moreover, the (non)-convexity properties of it have been analysed in [2]. For various versions of the continuum model similar to system (3.1.1) with and without diffusion terms an analogue to the discrete Murray's law has been formally proven in [69].
  Regarding the already mentioned tensor PDE, in [70] Haskovec et al. have proven that if the non-decreasing metabolic cost functional is (strictly) convex, also the according energy functional of the system is (strictly) convex.
  In [9] the authors compared two different but very similar systems of PDEs describing network formation, i.e., considering a vector-valued conductivity m (as stated in equations (3.1.1a)-(3.1.1b)) and a conductivity tensor $\mathbb{C}$ (as stated in [70] and first introduced in [79]), respectively. They also derived the vector-valued system with respect to m from the tensor system by $\mathbb{C} := m \otimes m$, ignoring the diffusive term for the derivation and re-introducing it later again. The two systems not only differ in the activation term, which is cubic for the vector-valued system and quadratic as well as only depending on $\mathbb{C}$ via p for the tensor-$\mathbb{C}$ system, but also in terms of the metabolic cost term, which becomes singular at $\mathbb{C} = 0$ if $\gamma < 1$ for the tensor-$\mathbb{C}$ system and at $m = 0$ if $\gamma < \frac{1}{2}$ for the vector-valued system.

3.2.2 Origins of the Network System: the Hu-Cai Discrete-Graph Model

An important feature of the PDE system (3.1.1) is that it was derived from a discrete-graph model introduced by [78]. This justifies the shape of the PDE system in the sense that its

features are inherited from an underlying network. In the following, we will briefly describe this discrete-graph model. We consider $G := (V, E)$ to be an undirected graph. Here, V is given as the finite set of vertices and E the finite set of edges, while $n = |V|$ is the number of vertices. It holds that a vertex is not connected to itself by an edge and that two vertices can be connected by at most one edge. So, edge $(i, j) \in E$ connects vertices $i \in V$ and $j \in V$. Since G is an undirected graph, we have that (i, j) and (j, i) represent the same edge. The parameter of the length of an edge is fixed and given by $L_{ij} > 0$ for all edges $(i, j) \in E$. Moreover, the conductivity of an edge $C_{ij} \geq 0$ is subject to the energy optimisation and adaptation process. Initially, it is assumed to be strictly positive for all edges, i.e., $C_{ij} > 0$ at time $t = 0$. The pressure in vertex $i \in V$ is given by P_i and the according pressure drop between vertices $i \in V$ and $j \in V$ follows

$$(\Delta P)_{ij} := P_j - P_i.$$

On the other hand, the oriented flux Q_{ij} from vertex $i \in V$ to vertex $j \in V$ can be written in terms of the conductivities of the edges as

$$Q_{ij} := C_{ij} \frac{P_j - P_i}{L_{ij}}, \qquad \forall (i, j) \in E.$$

Moreover, we consider the Kirchhoff law to ensure local mass conservation at each vertex. Hence, we have

$$- \sum_{j \in \mathcal{N}(i)} C_{ij} \frac{P_j - P_i}{L_{ij}} = S_i, \qquad \forall i \in V, \tag{3.2.1}$$

where $\mathcal{N}(i)$ is the set of vertices connected to vertex $i \in V$ via an edge and S_i represents the prescribed source (if $S_i > 0$) or sink (if $S_i < 0$) strength of the flow at vertex i. We also assume the global conservation of mass

$$\sum_{i \in V} S_i = 0$$

as solvability condition of the system. Moreover, Hu and Cai [78] propose a discrete energy functional consisting of a pumping power term and a metabolic cost term, i.e.,

$$\bar{\mathcal{E}}[C] := \sum_{(i,j) \in E} \left(\frac{Q_{ij}[C]^2}{C_{ij}^2} + c_0 C_{ij}^{\gamma} \right) L_{ij} \tag{3.2.2}$$

where c_0 is a metabolic coefficient and γ is an intrinsic constant of the network. Based on this energy functional, such that the dynamics satisfy $\mathrm{d}E/\mathrm{d}t \leq 0$ and the requirement that the dynamics should be equivalent to the diameter-adaptation model for blood vessels [80], Hu and Cai [78] introduce

$$\frac{\mathrm{d}C_{ij}}{\mathrm{d}t} = \left(\frac{Q_{ij}[C]^2}{C_{ij}^{\gamma+1}} - c_0 \gamma \right) C_{ij} L_{ij}, \tag{3.2.3}$$

as the dynamics for the conductivity constrained by the Kirchhoff law (3.2.1). It describes the driving stimulus of flow ($Q_{ij}[C]^2/C_{ij}^{\gamma+1}$) and the intrinsic decreasing stimulus ($c_0\gamma$).

Various studies have also addressed the corresponding microscopic system [3,27,62–66,69,78]. We comment on them next and defer the explanation of the connection between the discrete model presented above and the PDE system (3.1.1) for later.

In [64], the authors adapted the microscopic model proposed by Hu and Cai [78] in order to model auxin transportation in plant leaves. To account for auxin production and reduction in cells, Haskovec et al. [64] adapted the discrete graph-based model proposed in [78], additionally by introducing source terms and decay rates.

- **Existence of solutions.** The global existence of solutions for the coupled ODE-algebraic system proposed by Hu and Cai [78] was studied by Haskovec et al. in [66]. For the discrete auxin-transportation model, in [64], the authors proved the global existence and non-negativity of solutions.

- **Steady states.** For the steady states of the discrete auxin transportation model, Haskovec et al. [64] showed that they satisfy a generalised Murray's law, i.e., a scaling relation for branch conductivities in a transportation network.

- **Topological properties.** Topological properties of the discrete model introduced in [78] were studied analytically in [27], specifically, the question of loop formation in global minimisers of the energy functional. Hence, the authors proved that for $0 < \gamma < 1$ the energy minimiser does not contain loops. But for $\gamma > 1$ the energy minimiser may contain loops and their presence or absence depends on the initial data, such as the symmetry of the data, the configuration of the source and sink terms and the length of the edges. The result on loop-free graphs for $0 < \gamma < 1$ has been extended in [63] to its complement. Hence, in [63] the authors show that for $\gamma < 1$ every tree (or loop-free graph) represents a local minimiser of the energy with a concave metabolic cost term. Moreover, for $\gamma = 1$ they prove that every (local) minimiser is either a tree or that there exists a conductivity matrix with the same energy that corresponds to a loop-free graph. Additionally, in order to account for the robustness of the network, they adapt the energy functional by subtracting a multiple of the Fiedler number. The Fiedler number measures how robust a network is against the removal of edges. For $\gamma = 1$ the adapted energy functional is bounded from below, coercive and convex.

- **Other analytical results.** In [69], the validity of a generalisation of Murray's law for general transportation networks with multiple branches modelled via the discrete model stated in (3.2.1) and (3.2.2) has been shown. Murray's law is a physical principle that predicts the thickness or conductivity of branches in transportation networks.

For the numerical investigation of the discrete model, given in (3.2.1) and (3.2.2), a first attempt by Hu and Cai in [78] illustrates a phase transition at $\gamma = 1$ for the optimal network in the case of a geometry with fixed sinks composing the whole domain. For $\gamma < 1$, they obtain a treelike structure and for $\gamma > 1$ a uniform sheet. These results have been reassured by Albi et al. in [3]. They considered a diamond-shaped geometry and solved the Kirchhoff law via least square minimisation while solving (3.2.3) via implicit Euler. They obtained characteristic loops for $\gamma = 1.5$, loop-less structures for $\gamma = 0.5$ and an 'in-between' state for $\gamma = 1$ and thus a phase transition behaviour for the metabolic exponent γ. The numerical scheme proposed in this paper was adapted by Haskovec et al. in [66]. There, the authors again considered a planar graph in which the vertices and edges form a diamond-shaped geometry. The results demonstrate that the steady states strongly depend on the initial datum and the model parameters. In particular, the system remains stable under small perturbations of the initial data; however, larger perturbations may lead to convergence to a different steady state, indicating non-uniqueness of equilibria. Additionally, the choice of the time-step size is crucial, as convergence becomes extremely slow near the minimiser if the time-step size is too small.

In [63], the authors adapted the microscopic energy functional to account for the robustness of the network via the Fiedler number. They perform numerical experiments on this modified model using the projected subgradient method to find global minimisers. They searched for the optimal transportation network in two different settings: a complete graph with seven nodes and a leaf-shaped graph with 122 nodes and 323 edges. Among others, they obtain that for increasing $\mu > 0$, where μ is the strength factor of the Fiedler number in the adapted model, the graph becomes denser and the number of active edges increases monotonically for the complete graph. On the other hand, the number of active edges does not increase monotonically as μ increases for the leaf-shaped graph.

In [62] Haskovec simulates the discrete model (3.2.1) and (3.2.2) by minimising these equations using a discrete descent algorithm. This algorithm searches the discrete set of local minimisers by repeatedly exchanging a randomly selected edge of the spanning tree with another edge of the underlying graph such that the resulting graph has a lower energy value. This minimisation scheme is combined with a Monte-Carlo approach, such that the tree with the lowest energy value is the final output. Moreover, they investigate the discrete model in the set of a leaf-shaped graph with 122 nodes and 323 edges numerically for the global reaching centrality (GRC) of the (local) minimiser in dependence on the metabolic cost exponent $\gamma \in (0, 1]$. The GRC is a measure of the hierarchical organisation of the transport network, and they observe that with increasing γ, the GRC and thus the degree of hierarchy increase monotonically.

For the auxin transportation model studied in [64], various numerical simulations have been performed. Since the examined system is a stiff problem, implicit formulas are necessary, and thus, the authors considered a multi-step solver for their numerical experiments. They studied the influence of various geometries, specifically diamond-shaped, round, and oval grids, on the strength of the source and sink terms, as well as on small perturbations of the initial data. Hence, they observe that the model is robust to variations of the underlying grid and that the resulting network is stable under small perturbations of the initial data. Moreover, they conclude that the choice of the strength of the source and sink terms is vital for the resulting patterns. Additionally, not only a single source term but multiple sources and sinks within the domain were considered, which led to similar networks to those observed in leaves. Overall, the numerical results demonstrate that the model can effectively connect an auxin source-sink pair with a mid-vein and also produce branching vein patterns.

3.2.3 Continuum Limit

Limits via Mesoscopic Models

Finally, there are also mesoscopic models connecting the discrete and PDE models. In [27], a mesoscopic model is introduced that connects the discrete and continuum models for network formation from [78] and [79]. This mesoscopic model avoids explicit pressure terms in the energy. Instead, it takes the form of a Wasserstein-type gradient flow constrained by a Poisson equation. It characterises the evolution of a probability measure, indicating the directional presence of conductive edges at a specific point in space and time. The authors also conclude that solutions of the discrete network, realised as connected graphs with a finite number of edges and nodes, are special stationary states of the mesoscopic model.

A more general mesoscopic model has been established in [71], where the network is modelled via a probability measure μ representing the joint probability of the tensor-valued conductivity $\mathbb{C}$ at spatial location x. Hence, this framework generalises the model in [27], which is restricted to rank-one tensor-valued conductivities $\mathbb{C}$. Haskovec et al. [71] derive the gradient flow of

the corresponding energy functional with respect to the 2-Wasserstein topology in the space of probability measures. They prove that the energy functional is convex and semi-continuous. Notably, this convexity holds for all $\gamma > 0$ in contrast to the discrete and macroscopic models, where convexity is restricted to $\gamma > 1$. Moreover, a reduced Wasserstein gradient flow with respect to the conductivity variable alone is formulated. These two derivations lead to transport equations coupled to the Poisson equation, modelling dynamic changes in the transportation network. A further gradient flow with respect to the Fisher-Rao metric is derived, resulting in reaction-type partial differential equations, for which equilibrium states are also characterised. The authors conclude that not only the model presented in [27] but also the macroscopic models in [3, 67, 68, 70] can be obtained as reductions or special cases from their unified model.

Direct Limits from Discrete to Continuum Models

A specific case of the discrete system (3.2.1) and (3.2.2), involving a diagonal permeability tensor $\mathbb{C}$, was formally derived in [66] from the discrete network formation model introduced in [78]. This system arises as the formal L^2-gradient flow of the continuum energy functional, which itself results from the limiting process of a sequence of discrete problems under network refinement, with the geometry restricted to two-dimensional rectangular grids. The derivation was later made rigorous in [65], where the continuum functional was shown to be the Γ-limit of a sequence of discrete energy functionals with respect to the strong L^2-topology. Moreover, in [70], the formal derivation of the continuum energy functional was extended to the limit of a sequence of unstructured triangulations on a bounded domain. Additionally, the derivation of the resulting tensor PDE model was not only restricted to rank-one tensors but rather to tensors $\mathbb{C} \in \mathbb{R}^{d\times d}$ with $d \leq 3$ and considering a more general metabolic cost-function M.

In [64], the authors derived the formal macroscopic limit of the discrete auxin transportation model, which differs from other discrete formulations by the inclusion of additional sink and source terms. The derivation of the macroscopic limit was carried out for discrete graphs given by rectangular equidistant grids. For a suitable parameter range, the existence of weak solutions of the obtained continuum limit and of its steady states has been proven. Building on the mesoscopic model introduced in [27], the authors of [64] employ a monokinetic ansatz to derive a corresponding evolution equation for the conductivities.

3.3 Existing Numerical Methods for the Network System

The qualitative properties of the evolved network structures when performing numerical simulations on system (3.1.1) were first studied in [2, 3, 68]. Haskovec et al. in [68] used mixed finite elements for spatial approximations and an implicit-explicit first-order Euler scheme with adaptive time stepping to approximate time. Moreover, a diamond-shaped two-dimensional domain with one edge cut and Dirichlet (p) and homogeneous Neumann (m) boundary conditions was considered. Their numerical experiments focused on varying the parameters for the metabolic cost term γ and the diffusion term D and demonstrated a strong sensitivity to the mesh for certain parameter values. They observe that $\gamma < \frac{1}{2}$ leads to an extinction in finite time of the solution, which is consistent with their analytical results. On the other hand, for $D = 0$ and $\frac{1}{2} \leq \gamma < 1$, their numerical results indicate instability of stationary solutions in two dimensions, which complements their analytical result in one dimension. Furthermore, varying D led to the conclusion that for D too large, no interesting patterns in the stationary network solution occur. For $D = 0$, the conductivity cannot grow, and hence, $D > 0$ is essential for a growing network. In [2], these results were further extended by investigating the impact of different values

of the diffusion constant D, background permeability parameter r and the parameter for the metabolic cost term γ with respect to the intensity of the source and sink term S. In this paper, the authors used finite elements for spatial discretisation and a uniform time discretisation. The diffusive term was solved via a Crank-Nicolson method, and the remaining terms were treated explicitly. They considered a very small time step ($\Delta t = 10^{-5}$) to ensure energy decay. Again, homogeneous Neumann boundary conditions for m and Dirichlet boundary conditions for p on a two-dimensional polygonal domain were considered. In line with [67], they also observed that for small D, a network emerges, but for large D, the network structure is destroyed. Furthermore, they reported that lower permeability values r are associated with finer, more spatially distributed network structures and a faster formation process. Additionally, they monitored that for an increasing magnitude of the source and sink term S, the network tends to spread more throughout the domain. Regarding the influence of γ on the network structure, they concluded that decreasing values of γ show thinner and sparser network structures.

Albi et al. [3] focused on the qualitative behaviour of emerging network structures for differing values of D and γ. In order to solve problem (3.1.1) numerically, they employed finite elements. For equation (3.1.1b), they applied a splitting method as long as the energy is decreasing and switched to a forward-backward splitting if the energy is increasing, but the steady states have not been reached yet. For the splitting method, they compute the activation term via the explicit Euler method, the relaxation term is obtained via the implicit Euler method and bisection, and the diffusion is calculated exactly. Equation (3.1.1a) is solved by a preconditioned generalized minimal residual method (GMRES). The authors consider two different setups for their numerical experiments. On the one hand, they examine a rectangular domain with one source and two sinks for various values of γ. On the other hand, they investigate the qualitative behaviour of the network for various values of γ and D of a diamond-shaped domain with one edge cut, where the source is located, and the rest of the domain acts as a sink. For the first case, they obtain that branching appears for $\gamma = 0.5$, whereas for $\gamma = 0.75$ and $\gamma = 1$, two straight lines connect the source with the sinks. In the second case, i.e., the diamond-shaped geometry, they show that network sparsity increases as γ approaches 0.5. They observe the same behaviour for a decreasing diffusion coefficient. Hence, larger diffusion constants lead to stronger smoothing effects on the network structures.

In [56], Fang et al. especially investigate the stiffness of model (3.1.1), considering homogeneous Neumann boundary conditions for p and Dirichlet boundary conditions for m, and introduce efficient implicit and semi-implicit numerical schemes. They propose a fully implicit scheme for the one- and two-dimensional model, which is of second order in time. They prove that the scheme preserves energy decay and its unconditional stability, i.e., no restriction is placed on the size of the time step. For the two-dimensional case, the fully implicit scheme results in non-linear algebraic equations, which are hard to solve. Thus, the authors also develop a semi-implicit scheme for the one- and two-dimensional model. They prove that the energy decays for this scheme as well, but under a certain stability condition for the time step, which is independent of the mesh size. Moreover, to solve the Poisson equation, they exploit the Conjugate Gradient method. Through their numerical experiments, they show that the semi-implicit scheme is of first order and the fully implicit scheme of second order in time. Moreover, for the one-dimensional case, they recover the extinction of solutions for $\gamma \in [1/2, 1]$ as analytically obtained in [68]. They also investigate the effect of the diffusion coefficient D on the evolving network and found that for decreasing D, the network tends to form finer structural details and reaches equilibrium faster.

Hu and Cai [79] also performed numerical simulations on their proposed model as given in equations (3.1.1) with Dirichlet boundary condition for p and homogeneous Neumann boundary

condition for m. Moreover, they investigate the dependence of emerging treelike or loopy structures on the metabolic function and the source terms via numerical simulations. They observe that for concave metabolic cost functions and for in time and space fixed source and sink terms, treelike structures emerge as optimal transportation networks, while for a convex metabolic cost function, uniform sheets evolve. On the other hand, considering fluctuating source and sink terms, the loop density increases with increasing γ.

In [9], the authors compared the vector-valued system as stated in (3.1.1) and the corresponding tensor-valued system as introduced in [70], not only analytically but also numerically. Thus, for the numerical experiments, they considered only a spatially two-dimensional setting and employed a finite difference scheme on a uniform Cartesian grid with a spatial step $h = \Delta x = \Delta y$. The considered systems are stiff in all their components, and computation time is a crucial factor. Thus, the authors make use of the ADI (alternating direction implicit) method and introduce a small regularisation parameter for the reaction term of the tensor-$\mathbb{C}$ system. First, they carried out an accuracy test for the adopted numerical schemes. They furthermore performed various experiments in order to compare the behaviour of the two systems. Hence, the influence of the parameters for the diffusion D and the reaction γ, as well as the regularisation parameter ε, on the system has been investigated. Overall, they observed that the shape of the two networks is very different (Y-shaped for the vector-valued system (m) and V-shaped for the tensor-valued system ($\mathbb{C}$)) and, with increasing time, move apart from each other. Hence, even after only a few time steps, the solutions of the two systems are very different, which suggests that they intrinsically behave very differently. For the vector-valued model m and $D = 0$, the numerical simulations support the analytical results in [67], i.e., that the steady-states for $\gamma > 1$ are unique, and suggest that for $\gamma < 1$ the steady-states might not be unique.

As a continuation of [9], Astuto et al. in [10] further investigated the numerical simulations of the tensor-valued PDE model. In these experiments, the authors now used a symmetric ADI-scheme regarding the discretisation in time. Their main goal is to investigate the loss of symmetry and its dependence on the model parameters of the network during its evolution, especially its dependence on the background permeability r. They conclude that the condition number for the elliptic operator and thus the asymmetry of the network is increasing as r is decreasing, and that already for $r = 10^{-3}$ the symmetry of the network is completely lost. Moreover, they investigate convergence with respect to the Wasserstein distance, which leads to better results than considering the L^2-norm as provided in [9].

In [8] the authors propose for solving the tensor-valued model and for catching steady state solutions a low order finite element method for space discretisation coupled with a semi-implicit time advancing scheme based on backward Euler. Compared to [9], the authors choose homogeneous Neumann boundary conditions for the pressure p as well as the conductivity tensor $\mathbb{C}$ in [10]. For the simulations they consider a uniform partition of the time interval, uniform triangulations of the domain Ω and again as in [9, 10] add a regularisation parameter for the metabolic term of the conductivity tensor $\mathbb{C}$. They perform an accuracy study, i.e., computing the relative L^2-norm between two solutions with different Δx or δt in space and time, by considering the Richardson extrapolation and confirm first order accuracy. Moreover, they perform numerical experiments with varying values of the diffusion constant D, the background permeability r and the strength factor α of the metabolic cost term. The results show that for $r = 10^{-3}$, more detailed patterns appear, and for $r \to 0$, some oscillations appear in the energy plots while approaching the steady state. Furthermore, as D decreases, the ramifications of the network become thinner and again the energy shows some oscillations while approaching the steady state. On the contrary, for increasing α, more ramifications are observed.

3.4 Fourier–Based Spectral Numerical Method

3.4.1 Key Idea and Motivation

Our algorithm, similar to the one presented in [3], uses a splitting method for the time discretisation of equation (3.1.1b). Specifically, at each time step we compute the conductivity m by updating separately the values for the activation, relaxation and the diffusion terms. The key of our method, however, is in the resolution of the equation for p (3.1.1a). The goal is to use for this a Fourier-based spectral method – implemented via the Fast Fourier Transform (FFT). This is motivated by computational and theoretical considerations. Since we formulate the model with periodic boundary conditions, implementation via FFT is a rather natural choice as it provides an efficient way to compute the spatial derivatives for p and m and to solve the elliptic Poisson equation for the pressure p, which reduces the computational cost from $\mathcal{O}(N^2)$ to $\mathcal{O}(N \log N)$ for N grid points. Hence, a huge advantage of applying FFT compared to Finite Element Methods (FEM) is that the differential operators can be encoded in Fourier space – leading to multiplications in this space – and thus avoids the assembly and inversion of large sparse matrices as in FEM. Moreover, spectral methods such as FFT achieve higher accuracy for smooth enough solutions on coarser meshes compared to FEM. Furthermore, in the setup of uniform meshes and periodic boundary conditions, an extension to higher dimensions will be less complex and thus easier via FFT than via FEM.

3.4.2 Discretisations and Notations

Let $(t^k)_{k=0}^n$ with $n \geq 1$ and $0 \leq t^0 < ... < t^k < t^{k+1} < ... < t^n \geq T$ be a discretisation of the time interval $[0, T]$, with $\Delta t^k = t^{k+1} - t^k$.

Given a bounded rectangular domain $\Omega = [0, L_x] \times [0, L_y]$, for $L_x,\ L_y > 0$, we discretise the domain via a uniform rectangular mesh $\mathcal{T}_h$ with $h = (h_x, h_y) \in \mathbb{R}^2$ and $h_x, h_y > 0$ being the mesh sizes in x and y direction. Thus, we define the associated set of vertices to the given mesh $\mathcal{T}_h$ as $\{(x_i, y_j) : 0 \leq i \leq N_x, 0 \leq j \leq N_y\}$, where $N_x + 1$ and $N_y + 1$ denotes the number of elements along the x-axis and y-axis respectively. If we consider given mesh sizes h_x and h_y of the partition $\mathcal{T}_h$, we have $h_x = \Delta x = \frac{L_x}{N_x}$ and $h_y = \Delta y = \frac{L_y}{N_y}$, we obtain $0 = x_0 < x_1 < ... < x_i < ... < x_{N_x} = L_x$ with $x_{i+1} = x_i + \Delta x$ as partition of $[0, L_x]$ and analogously $y_{j+1} = y_j + \Delta y$ with $y_0 = 0$ and $y_{N_y} = L_y$ as partition of $[0, L_y]$.

We denote by p_h^k the time and space discretised solution of (3.1.1a) and by m_h^k the time and space discretised solution of (3.1.1b). We denote by p_{ij}^k the approximated discretised solution of the pressure p at node (x_i, y_j) at time t^k, i.e., $p_{ij}^k \approx p(t^k, x_i, y_j)$ and analogously for the conductivity m, i.e., $m_{ij}^k \approx m(t^k, x_i, y_j)$.

3.4.3 Splitting for the Conductivity Equation

We split (3.1.1b) into activation, relaxation, and diffusion substeps.

Activation Term

The activation part of the parabolic equation of m (3.1.1b) is given by

$$\partial_t m = c^2 \left(m \cdot \nabla p\right) \nabla p = c^2 \left(\nabla p \otimes \nabla p\right) m.$$

For $|\nabla p(t,x,y)| \neq 0$ the exact solution reads

$$m(t,x,y) = \frac{1}{|\nabla p|^2}\left[\left((\nabla p)^\perp \otimes (\nabla p)^\perp\right) + (\nabla p \otimes \nabla p)\exp(c^2|\nabla p|^2 t)\right] m_0(x,y), \tag{3.4.1}$$

with $m_0(x,y) = m(0,x,y)$. If $|\nabla p(t,x,y)| = 0$, then $\partial_t m(t,x,y) = 0$ and in this case $m(t,x,y) = m_0(x,y)$.

The time and space discretised version of (3.4.1) reads

$$m_{ij}^{k+1} = \begin{cases} m_{ij}^k & \text{if} \quad |\nabla p_{ij}^k|^2 = 0, \\ \frac{m_{ij}^k}{|\nabla p_{ij}^k|^2}\left(\left(\nabla p_{ij}^k\right)^\perp \otimes \left(\nabla p_{ij}^k\right)^\perp + \left(\nabla p_{ij}^k \otimes \nabla p_{ij}^k\right)\exp\left(c^2|\nabla p_{ij}^k|^2 \Delta t^k\right)\right) & \text{else,} \end{cases} \tag{3.4.2}$$

where $m_{ij}^k = m(t^k, x_i, y_j)$ and $p_{ij}^k = p(t^k, x_i, y_j)$ are the numerical approximations of m and p at time t_k at node (x_i, y_j) as described in the beginning of the section.

Remark 3.4.1. *The term* $\exp(c^2|\nabla p|^2\Delta t)$ *in expression* (3.4.1) *creates stiffness, which restricts the admissible time-step size* Δt*. In particular,* Δt *must be chosen sufficiently small so that this term remains bounded and can be computed reliably in numerical simulations.*

Relaxation Term

The metabolic cost term for the evolution of the conductivity m is given by the equation

$$\partial_t m = -|m|^{2(\gamma-1)} m,$$

whose solution is

$$m(t,x,y) = \begin{cases} m_0(x,y)\exp(-t) & \text{if} \quad \gamma = 1, \\ m_0(x,y) & \text{else if} \quad |m_0| = 0, \\ \frac{1}{|m_0(x,y)|}\left(|m_0(x,y)|^{2(1-\gamma)} - 2(1-\gamma)t\right)^{1/2(1-\gamma)} m_0(x,y) & \text{otherwise.} \end{cases}$$

We consider the following time and space discretisation for this solution:

$$m_{ij}^{k+1} = \begin{cases} m_{ij}^k \exp(-\Delta t^k) & \text{if } \gamma = 1, \\ m_{ij}^k & \text{else if } |m_{ij}^k| = 0, \\ a_{ij}^k \mathbb{1}_{b_{ij}^k \geq 0} & \text{otherwise,} \end{cases} \tag{3.4.3}$$

where

$$\begin{aligned} a_{ij}^k &:= \frac{m_{ij}^k}{|m_{ij}^k|}\left(|m_{ij}^k|^{2(1-\gamma)} - 2(1-\gamma)\Delta t^k\right)^{\frac{1}{2(1-\gamma)}}, \\ b_{ij}^k &:= |m_{ij}^k|^{2(1-\gamma)} - 2(1-\gamma)\Delta t^k, \end{aligned}$$

and $\mathbb{1}$ is the indicator function.

The indicator function in the last case of (3.4.3) ensures that the solution stays real, as negative values for b_{ij}^k might lead to complex solutions, depending on the value of $\gamma \in [0,1)$. This approximation is necessary since, if we wanted to stop the computation at the time when

the solution hits zero, this would put the following constraint on the time step

$$\Delta t \leq \frac{|m_0(x)|^{2(1-\gamma)}}{2(1-\gamma)},$$

which, for $\gamma \in [0,1)$, leads to very restrictive time steps.

Diffusion Term

The diffusive term is given by

$$\partial_t m = D^2 \Delta m. \tag{3.4.6}$$

Since we consider periodic boundary conditions, we can apply the Fourier transform $\mathcal{F}$. We denote the Fourier-space variables by $\xi_x \in \mathbb{R}$ and $\xi_y \in \mathbb{R}$. With these variables, the Laplacian Δ in Euclidean space transforms into $-[\xi_x^2 + \xi_y^2]$ in Fourier space. Hence, we are able to transform equation (3.4.6) into

$$\frac{d}{dt}\mathcal{F}(m) = D^2 \left[-\xi_x^2 - \xi_y^2\right] \mathcal{F}(m).$$

These equations can be solved explicitly, and thus we obtain as solution for m

$$m(t) = \mathcal{F}^{-1}\left(e^{D^2[-\xi_x^2-\xi_y^2]t} \frac{\mathcal{F}(m)(t_0)}{e^{D^2[-\xi_x^2-\xi_y^2]t_0}}\right), \tag{3.4.7}$$

where $\mathcal{F}^{-1}$ denotes the inverse Fourier transform and t_0 is the initial time.

Next, to approximate this solution for m numerically, we will use the Fast Fourier Transform (FFT) as approximation of the Fourier transform. Thus, we will consider the space and time discretised version of equation (3.4.7) in the following. Remember that we consider the space $[0,T] \times \Omega$ where $\Omega = [0, L_x] \times [0, L_y]$. We denote the discrete version of the Fourier transform as $\hat{\mathcal{F}}$ and its inverse by $\hat{\mathcal{F}}^{-1}$. Moreover, we define the discretised Fourier-space variables $\hat{\xi}_x$ and $\hat{\xi}_y$ such that $\hat{\xi}_x(\ell)$ for $0 \leq \ell < N_x$ is given by

$$\hat{\xi}_x(\ell) := \begin{cases} \frac{2\pi\ell}{L_x} & \text{for } 0 \leq \ell \leq \frac{N_x}{2}, \\ \frac{2\pi(\ell - N_x)}{L_x} & \text{for } \frac{N_x}{2} < \ell < N_x \end{cases}$$

where N_x is the number of nodes used for the FFT (i.e., in our case $N_x = {}^{L_x}/_{\Delta x}$ and analogously for $\hat{\xi}_y(j)$ as $0 \leq j < N_y$. Thus, the time and space discretised solution $m_{\ell j}^k$ to the diffusion equation (3.4.6) reads

$$m_{\ell j}^{k+1} = \hat{\mathcal{F}}^{-1}\left(e^{D^2\left[-\xi_x(\ell)^2 - \xi_y(j)^2\right]\Delta t^k} \mathcal{F}(m_{\ell j}^k)\right). \tag{3.4.8}$$

For the implementation of the approximation of the diffusion term via FFT, we use the FFTW library developed by Frigo and Johnson [60] and apply it in two dimensions. For further details on the FFTW and its implementation, see [60]

3.4.4 Equation for the Pressure p: FFT+CG

The method we use to compute the equation for the pressure p (3.1.1a) combines the Fourier transformation and the Conjugate Gradient (CG) method.
As for the diffusive part of the equation for m, i.e., (3.4.6), we apply the FFT to transform

equation (3.1.1a) into

$$-\mathcal{F}^{-1}\left[i\begin{pmatrix}\xi_x\\ \xi_y\end{pmatrix}\cdot\mathcal{F}\left((m\otimes m+r\mathrm{Id})\,\mathcal{F}^{-1}\left[i\begin{pmatrix}\xi_x\\ \xi_y\end{pmatrix}\mathcal{F}(p)\right]\right)\right]=S,$$

where $\mathcal{F}$ is the continuous Fourier transformation, $\mathcal{F}^{-1}$ the inverse Fourier transformation, i is the imaginary unit, and ξ_x and ξ_y are the Fourier-space variables.

Setting $\hat{\mathcal{F}}$ and $\hat{\mathcal{F}}^{-1}$ as the discrete (inverse) Fourier transformation, the time and space discretised version of the above equation reads

$$-\hat{\mathcal{F}}^{-1}\left[i\begin{pmatrix}\hat{\xi}_x(\ell)\\ \hat{\xi}_y(j)\end{pmatrix}\cdot\hat{\mathcal{F}}\left(\left(m_{\ell j}^k\otimes m_{\ell j}^k+r\mathrm{Id}\right)\hat{\mathcal{F}}^{-1}\left[i\begin{pmatrix}\hat{\xi}_x(\ell)\\ \hat{\xi}_y(j)\end{pmatrix}\hat{\mathcal{F}}\left(p_{\ell j}^{k+1}\right)\right]\right)\right]=S_{\ell j}. \quad (3.4.9)$$

Here, $S_{\ell j}$ is the numerical approximation of the source-and sink terms, i.e., $S_{\ell j}\approx S(x_\ell,x_j)$.

Now, in order to compute $p_{\ell j}^{k+1}$, we will apply the CG method to equation (3.4.9) with $p_{\ell j}^k$ as initial data for the iterative method. In general, the CG method solves symmetric, positive definite linear systems of the form $Ax=b$ with an iterative procedure, where $A\in\mathbb{R}^{n\times n}$ and $x,b\in\mathbb{R}^n$ [20]. Note that for the numerical computation of the CG method, it is not necessary that the matrix A is explicitly available, since only the matrix-vector product will be used, and moreover, the CG algorithm terminates if the residual error is smaller than a given threshold [20]. We apply the CG method as described in Algorithm 10.1 in [20]. For further details on the CG method, we refer to Chapter 10.4 and, in particular, Algorithm 10.1 in [20].

3.4.5 Stopping Criteria and Energy Evaluation

We impose two stopping criteria. One is based on the relative change of the conductivity m:

$$\Delta m_h^k:=\frac{||m_h^k-m_h^{k-1}||_2}{\Delta t^k||m_h^{k-1}||_2},$$

here $\|\cdot\|_2$ is the discrete L^2-norm. We use this stopping criterion as a signal that the simulation is close to a stationary solution. The second stopping criterion terminates the algorithm if the discrete energy increases, that is, if $\mathcal{E}_h^k\geq\mathcal{E}_h^{k-1}$, with

$$\mathcal{E}_h^k(m_h^k):=\frac{D^2}{2}\|\nabla m_h^k\|_2^2+\frac{rc^2}{2}\|\nabla p_h^k\|_2^2+\frac{c^2}{2}\|m_h^k\cdot\nabla p_h^k\|_2^2+\frac{1}{2\gamma}\||m_h^k|^\gamma\|_2^2.$$

3.4.6 Pseudocode

Table 1 gives the pseudocode to simulate system (3.1.1).

3.5 Numerical Experiments

3.5.1 Numerical Setup

To showcase the numerical method presented in Section 3.4, we will consider two types of experiments on $\Omega=[0,1]^2$ with periodic boundary conditions inspired by previously considered setups in the literature. Unless stated otherwise, we use $r=0.1$, $c=200$, a fixed time step

Algorithm 1: FFT+CCG splitting algorithm for (3.1.1)

Input: $\Omega = [0, L_x] \times [0, L_y]$, r, c, D, γ, $\Delta x, \Delta y$, Δt, initial m_0, source S with $\int_\Omega S \, \mathrm{d}x \, \mathrm{d}y = 0$, periodic BCs

Output: p_h^k, m_h^k

while $\Delta m_h^k := \frac{||m_h^k - m_h^{k-1}||_2}{\Delta t^k ||m_h^{k-1}||_2} > \varepsilon$ and $\mathcal{E}_h\left(m_h^{k+1}\right) < \mathcal{E}_h\left(m_h^k\right)$

  Step 1 (solve equation (3.1.1a)**):** Compute p_h^{k+1} with S, m_h^k and r via solving

$$-\nabla \cdot [(rI + m_h^k \otimes m_h^k) \nabla p_h^{k+1}] = S$$

  with FFT+CG as described in Section 3.4.4;

  Step 2 (solve eq.(3.1.1b) **via splitting algorithm):**

  Activation: (use explicit solution)

  compute gradient of p via FFT

  compute solution of m of activation term as stated in equation (3.4.2)

  Relaxation: (use explicit solution)

  update m_h^{k+1} according to equation (3.4.3)

  Diffusion: (solved via FFT)

  compute m_h^{k+1} via FFT and the inverse FFT as stated in equation (3.4.8)

return solutions p_h^{k+1}, m_h^{k+1}

$\Delta t = 0.005$ conforming to Remark 3.4.1, and a CG residual threshold $\|res^k\| \leq 10^{-7}$. For the stopping criteria of the algorithm, we pick $\Delta m_h^k \leq 10^{-4}$.

We also consider three different initial conditions for the conductivity vector m:

$$m_{\text{ini}}^A = \big(\exp(-10^4(y-0.5)^2 - 50(x-0.5)^2),\, 0\big), \tag{3.5.1}$$

$$m_{\text{ini}}^B = \big(\exp(-50(y-0.5)^2 - 50(x-0.5)^2),\, 0\big), \tag{3.5.2}$$

$$m_{\text{ini}}^{\text{const}} = (1, 1). \tag{3.5.3}$$

Note that all these initial conditions for the conductivity are periodic in the considered domain Ω. Here m_{ini}^{const} is isotropic, while m_{ini}^A is anisotropic. The initial condition m_{ini}^B is isotropic but not equal in its components. The maximum value of $m_{ini,1}^A$ and $m_{ini,1}^B$ in Ω is reached at the centre of the domain Ω at (0.5,0.5), and then it decays exponentially. However $m_{ini,1}^A$ decays faster along the y axis. The initial data m_{ini}^A, m_{ini}^B and m_{ini}^{const} are inspired from the ones used in previous literature [3, 9].

Inspired also from previous literature, we will consider two setups for the source S in (3.1.1a). In Section 3.5.2, we investigate experiments where we examine a squared domain with one source and four sinks. In Section 3.5.3 we study the case where the whole domain acts as a sink.

3.5.2 One Source and Four Sinks

In this setup, we consider one source and four sinks so that $S = S_4(x, y)$ reads

$$S_4(x, y) = S_{source}(x, y) - \sum_{i=1}^{4} S_{sink_i},$$

with

$$S_{source}(x, y) = \exp(-1000((y - 0.5)^2 + (x - 0.5)^2)),$$

and

$$S_{sink_i} = \frac{1}{4} \exp(-1000((y - y_i)^2 + (x - x_i)^2)) \qquad \text{for } i \leq 4.$$

Notice that indeed $\int_\Omega S(x, y)dxdy = 0$ holds. Here, the source S_{source} is centred at $(0.5, 0.5)$ and decays rapidly (exponentially) in an isotropic way. The sinks are located at different points, they also decay exponentially and are isotropic. Specifically, the sinks are located at $(x_1, y_1) = (0.2, 0.2), (x_2, y_2) = (0.2, 0.8), (x_3, y_3) = (0.8, 0.2)$ and $(x_4, y_4) = (0.8, 0.8)$, which results in a periodic setup, which is symmetric along the axes. For the simulations, we consider $c = 200$ and $D = 0.0025$ since these are values for which a clear network emerges and an initial conductivity given by m^A_{ini} in (3.5.1). This initial data will make the network want to develop towards the right and the left.

Figure 3.1 depicts this initial setup for these simulations as well as the time evolution of the discretised energy $\mathcal{E}^k_h$ for $\gamma = 1$.

In Figure 3.2 and 3.3, the corresponding simulation results for $\gamma \in \{0.5, 0.7, 0.75, 0.8, 0.9, 1\}$ for $\log_{10} |m|^2$ and for $|\nabla p|^2$ are presented. Note that we set $t_{end} = 150$ and all simulations except for $\gamma = 0.5$ stopped due to reaching t_{end}. For these simulations, the different energy evolutions over time look similar to the one depicted in Figure 3.1 for $\gamma = 1$, and thus we assume that the results for $t_{end} = 150$ are close to the steady states. For $\gamma = 0.5$, the simulation broke at $t^k = 20.545$ due to energy increase. This is the reason why we do not observe a network between the source and the sinks. We remind the reader that for general r, the existence of solutions has been proven only for $\gamma \geq \frac{1}{2}$. We observe that for $\gamma \in \{0.9, 1\}$ at the steady states, there are no branches but rather straight lines from the source to the sinks, and as γ increases, the network is getting thicker. Regarding $\gamma \in \{0.7, 0.75, 0.8\}$, we notice that as γ increases, the branching point of the network moves closer to the source in the centre. In general, we see that as γ increases, the steady state becomes more diagonally symmetric, which means that the anisotropic effect of the initial conductivity m^A_{ini} is lost. The case $\gamma = 1$ is a critical case. We see that in this case, the branches are significantly wider, indicating that diffusion becomes more dominant.

For completeness, we also added the figures for the $|\nabla p|^2$ in this setup in Figure 3.3.

3.5.3 Internal Sink

For this section, we only consider an internal sink term, which means that the sink is constantly spread over the whole domain such that the total integral of the source and sink term is 0, i.e., $\int_\Omega S(x, y)\,\mathrm{d}x\,\mathrm{d}y = 0$. In the following the source and sink term $S = S_{int}(x, y)$ is given by

$$S_{int}(x, y) = \exp(-1000((y - 0.5)^2 + (x - 0.5)^2)) - \frac{\pi}{1000}.$$

Figure 3.4 shows the time evolution of the formation of the network for $c = 200$,

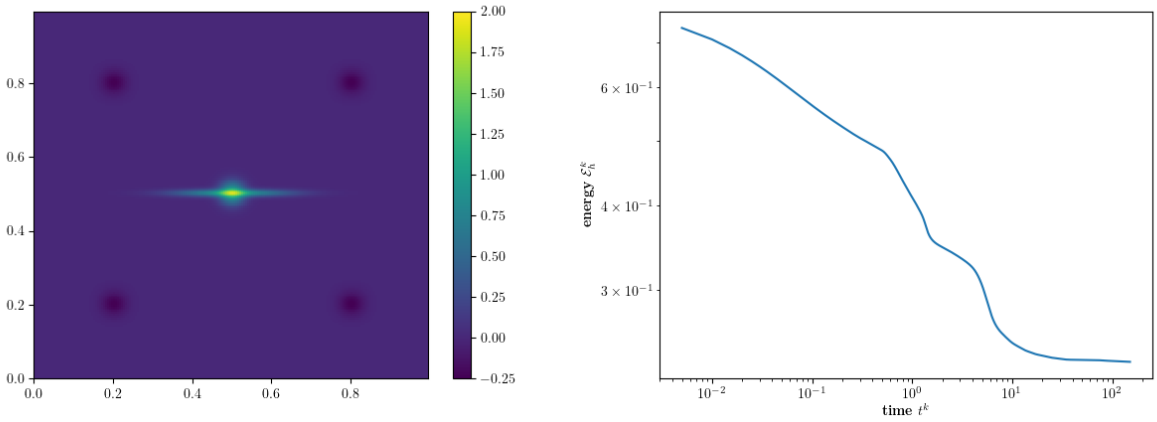

Figure 3.1: Left: Source and sink term $S_4(x, y)$ and initial conductivity m_{ini}^A. Right: Evolution of the discrete energy $\mathcal{E}_h^k$ for $c = 200, D = 0.0025$ and $\gamma = 1$.

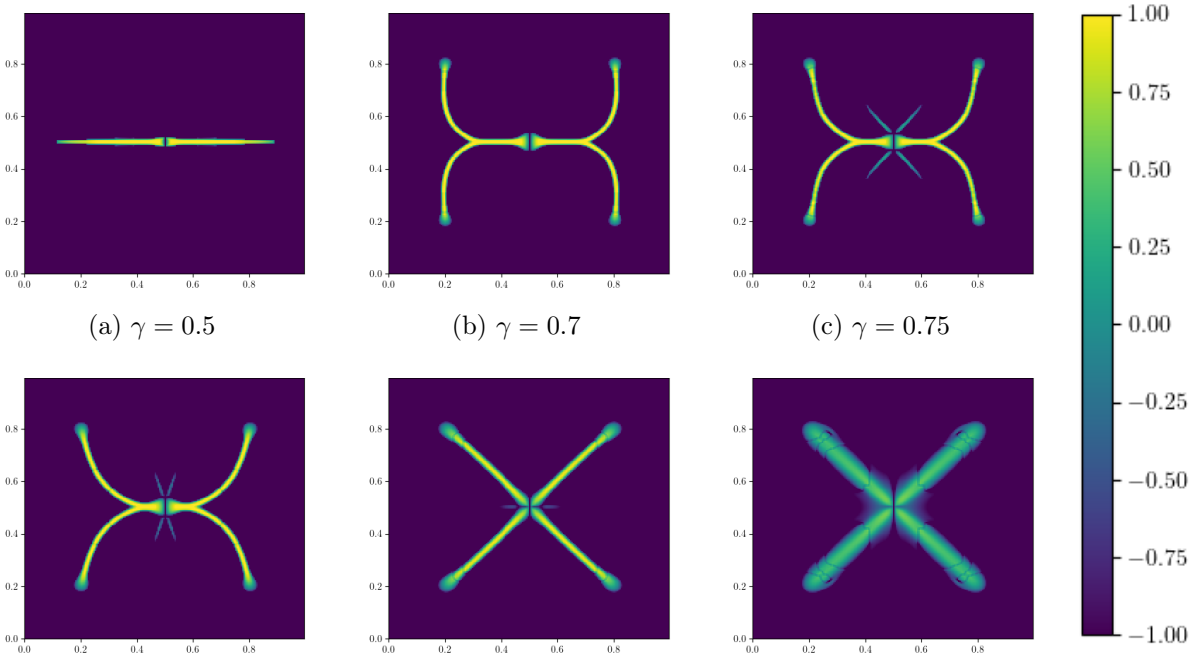

(a) $\gamma = 0.5$ (b) $\gamma = 0.7$ (c) $\gamma = 0.75$

(d) $\gamma = 0.8$ (e) $\gamma = 0.9$ (f) $\gamma = 1$

Figure 3.2: Steady states of $\log_{10}|m|^2$ for $c = 200$, $D = 0.0025$, m_{ini}^A, S_4 (one source, four sinks) and varying metabolic exponent $\gamma \in \{0.5, 0.7, 0.75, 0.8, 0.9, 1\}$. We observe more symmetric networks and branches moving closer to the source as γ increases.

$D = 0.0025, \gamma = 0.75$ starting from the constant initial condition m_{ini}^{const} as stated in (3.5.3). We observe that branches are evolving, but they vanish over time as the energy decreases, and only a few main branches remain at later times ($t = 50$, $t = 200$), indicating a transition toward a simpler, energetically favourable structure.

The corresponding evolution of the discretised energy $\mathcal{E}_h^k$ as well as the evolution of the relative

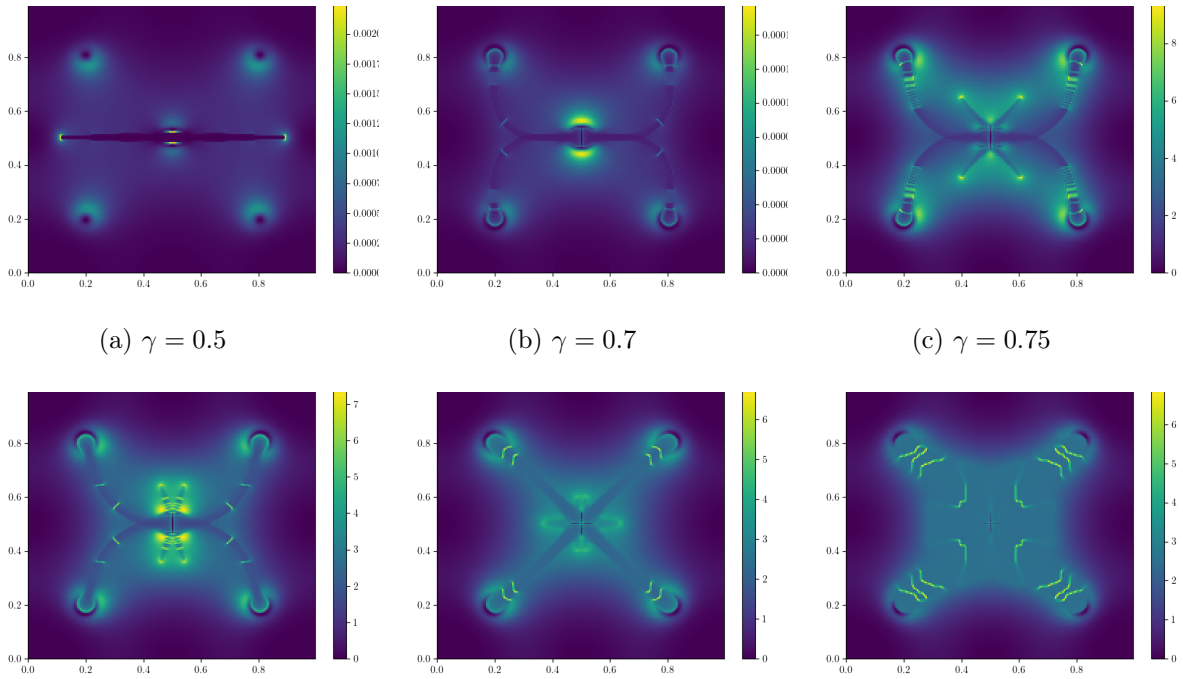

(a) $\gamma = 0.5$ (b) $\gamma = 0.7$ (c) $\gamma = 0.75$

(d) $\gamma = 0.8$ (e) $\gamma = 0.9$ (f) $\gamma = 1$

Figure 3.3: Steady states of $|\nabla p|^2$ for $c = 200, D = 0.0025$, m^A_{ini}, S_4 (one source, four sinks) and varying metabolic exponent $\gamma \in \{0.5, 0.7, 0.75, 0.8, 0.9, 1\}$.

error of the conductivity vector m, i.e., $\|\Delta m^k_h\|_2$, over time are shown in Figure 3.5. We observe a monotonic decrease in energy and its eventual stabilisation, accompanied by a decrease in the relative change of m. Although the breaking condition for the conductivity m is not yet satisfied at $t_{end} = 200$, the results suggest that the system is already very close to equilibrium.

(3.5.2)

Figure 3.6 shows a comparison of the final states of the network at $t_{end} = 200$ for different initial conditions, i.e., for m^A_{ini} as stated in (3.5.1) (left column of the figure), m^B_{ini} as defined in (3.5.2) (middle column of the figure) and m^{const}_{ini} given in (3.5.3) (right column of the figure). It not only depicts the norm of the conductivity vector $|m|$ but also the norm of the pressure gradient $|\nabla p|$ at the final state. Moreover, the different values of the relative error of the conductivity m for the breaking condition are given by $\|\Delta m^{const}\|_2 = 6.06 \cdot 10^{-3}$ for the constant initial value of m and by $\|\Delta m^A\|_2 = 2.67 \cdot 10^{-3}$ and $\|\Delta m^B\|_2 = 3.54 \cdot 10^{-3}$ at $t_{end} = 200$. Since the energy changes only marginally in all three cases at t_{end}, we assume to be close to the steady state in all scenarios. However, the final states for m and p behave very differently depending on the initial conditions. We observe that for the constant initial condition m^{const}_{ini}, the branches are curvier, located at different points in space and less clear compared to the results for m^A_{ini} and m^B_{ini}. Hence, we conclude that different initial conditions might lead to different steady states, which is in coherence with numerical results by [9] and the fact that the energy is non-convex.

Next, we investigate the influence of the activation parameter c on the network. Therefore, we consider the values $c = 200$ and $c = 100$ for two different setups. In both scenarios, we use $\gamma = 0.75$ as the value for the exponent of the metabolic cost term. On the other hand, we consider $D = 0.0025$ and $D = 0.0075$ as the diffusion constant. The numerical results for the logarithm of the Euclidean norm of the conductivity $m(t, x, y)$ are depicted in Figure 3.7. The

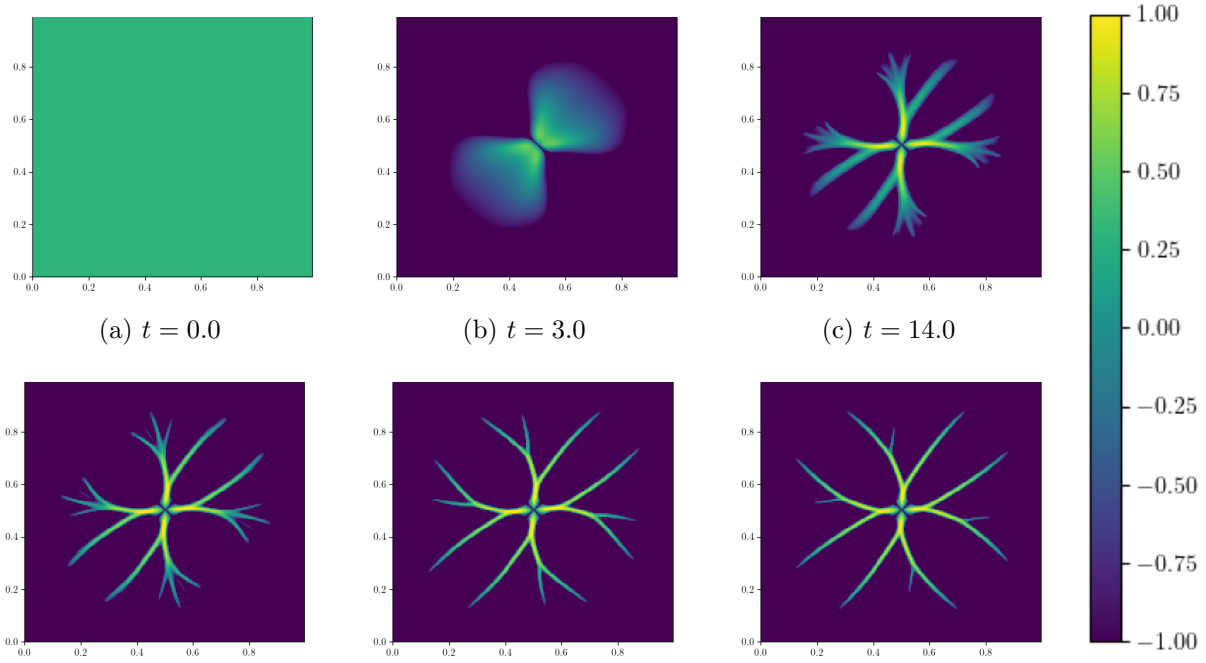

(a) $t = 0.0$ (b) $t = 3.0$ (c) $t = 14.0$

(d) $t = 20.0$ (e) $t = 50.0$ (f) $t = 200.0$

Figure 3.4: Time evolution of $\log_{10}|m|$ for $c = 200, D = 0.0025$ and $\gamma = 0.75$, m_{ini}^{const} and S_{int} (internal sink). At times $t = 3$ and $t = 14$ a dense branching network is formed. But as time evolves, smaller branches vanish, and the structure simplifies such that only a few main branches remain at $t_{end} = 200$.

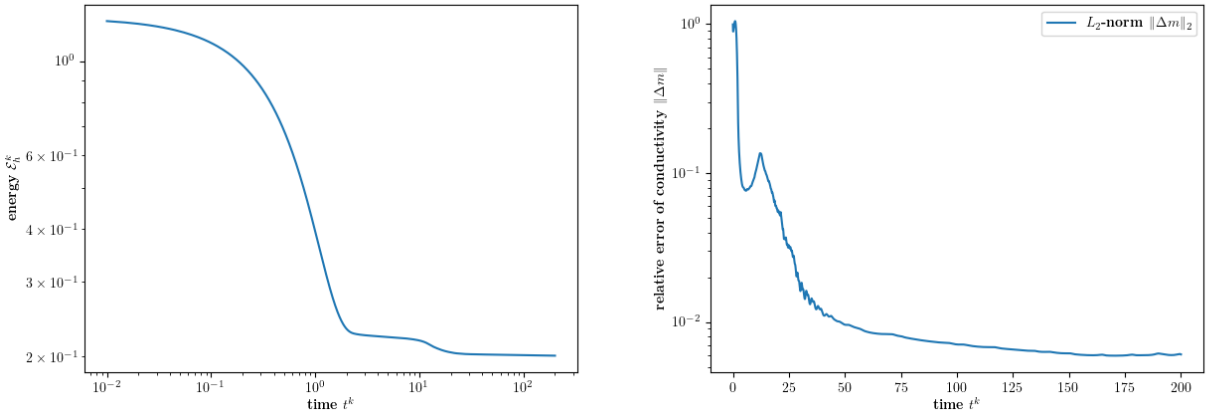

(a) Energy evolution over time (b) Evolution of $\|\Delta m\|_2$ over time

Figure 3.5: Time evolution of the discrete energy $\mathcal{E}_h^k$ and the relative error of the conductivity vector $\|\Delta m_h^k\|_2$ for $c = 200, D = 0.0025$, $\gamma = 0.75$, m_{ini}^{const} and S_{int} (internal sink). The energy decreases monotonically and stabilises, indicating that the system is close to equilibrium, while the relative change in m is decreasing accordingly.

right column of the figure shows the results for $c = 100$, and the left column shows $c = 200$. The first row corresponds to $D = 0.0025$, and the second row corresponds to $D = 0.0075$.

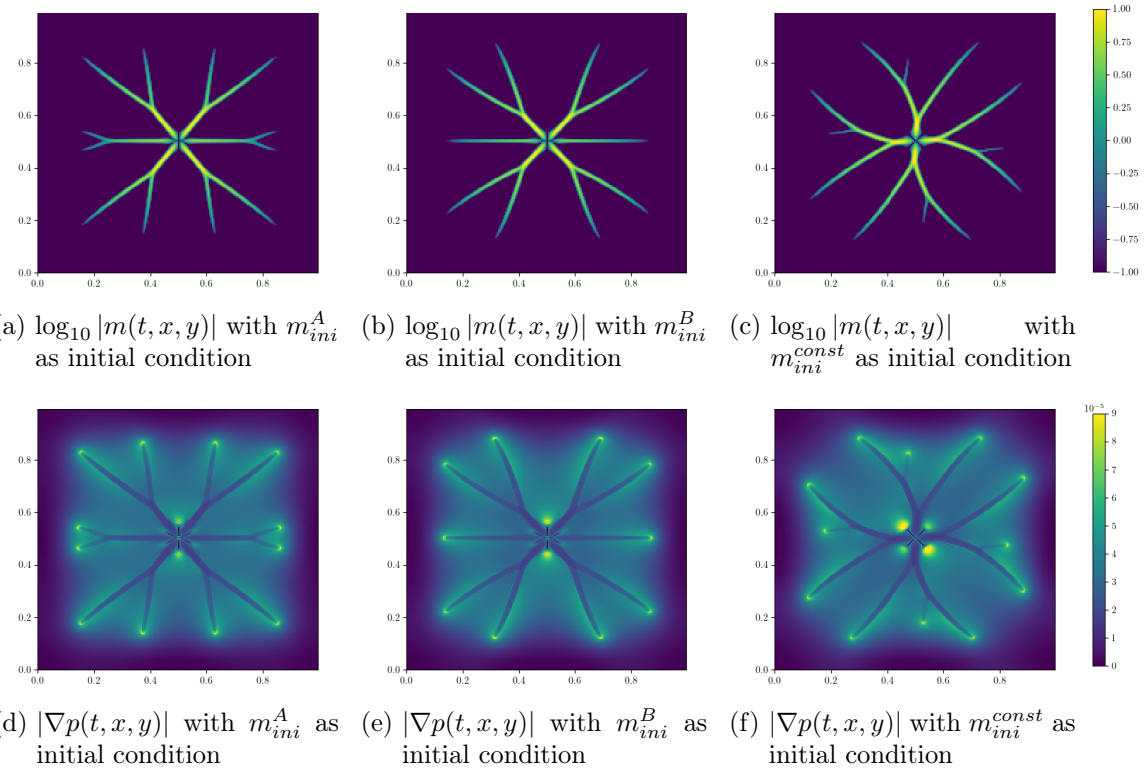

(a) $\log_{10}|m(t,x,y)|$ with m^A_{ini} as initial condition

(b) $\log_{10}|m(t,x,y)|$ with m^B_{ini} as initial condition

(c) $\log_{10}|m(t,x,y)|$ with m^{const}_{ini} as initial condition

(d) $|\nabla p(t,x,y)|$ with m^A_{ini} as initial condition

(e) $|\nabla p(t,x,y)|$ with m^B_{ini} as initial condition

(f) $|\nabla p(t,x,y)|$ with m^{const}_{ini} as initial condition

Figure 3.6: Comparison of numerical results for the conductivity $m(t,x,y)$ and the pressure gradient $|\nabla p(t,x,y)|^2$ close to steady state ($t_{end} = 200$) for different initial conditions m_{ini}. The modelling parameters chosen are $c = 200, \gamma = 0.75, r = 0.1, D = 0.0025$, $\Delta t^k = 0.005$, S_{int} (internal sink). First column: results for m^A_{ini}. Middle column: results for m^B_{ini}. Last column: results for m^{const}_{ini}. We conclude that different initial conditions lead to different steady states for $\gamma = 0.75$.

We observe that for $c = 200$ the network forms thicker and more pronounced branches, which also reach further into the domain than for $c = 100$. On the other hand, smaller activation ($c = 100$) leads to sparser networks, and in the presented cases, the networks even collapse to a simple cross (for $D = 0.0025$) or star-shaped configuration (for $D = 0.0075$). Moreover, we conclude that for smaller diffusion parameters, as depicted in the top row for $D = 0.0025$, the networks are finer and more detailed with thin filaments extending outward, while larger diffusion ($D = 0.0075$, bottom row) leads to smoother and more compact networks with fewer but thicker branches. Hence, the combined effects indicate that activation has to dominate the diffusion part for the emergence of complex networks, while increased diffusion or reduced activation suppresses branching and the system tends to converge to simpler steady states.

In Figure 3.8 we study the influence of the diffusion parameter D and the metabolic exponent γ on the evolution of the network. We consider $c = 200$ as the activation constant. The initial condition for the conductivity $m(t,x,y)$ is given by m^A_{ini} as stated in (3.5.1). The numerical results for $\log_{10}|m|$ of the conductivity m are depicted in that figure, where γ varies in $\{0.5, 0.75, 0.8, 1\}$ (top to bottom row of the figure) and $D \in \{0.001, 0.0025, 0.005, 0.0075, 0.01\}$ (left to right column of the figure). We observe that for small values of diffusion, finer and highly branched networks evolve. On the other hand, increasing D leads to thicker and smoother structures,

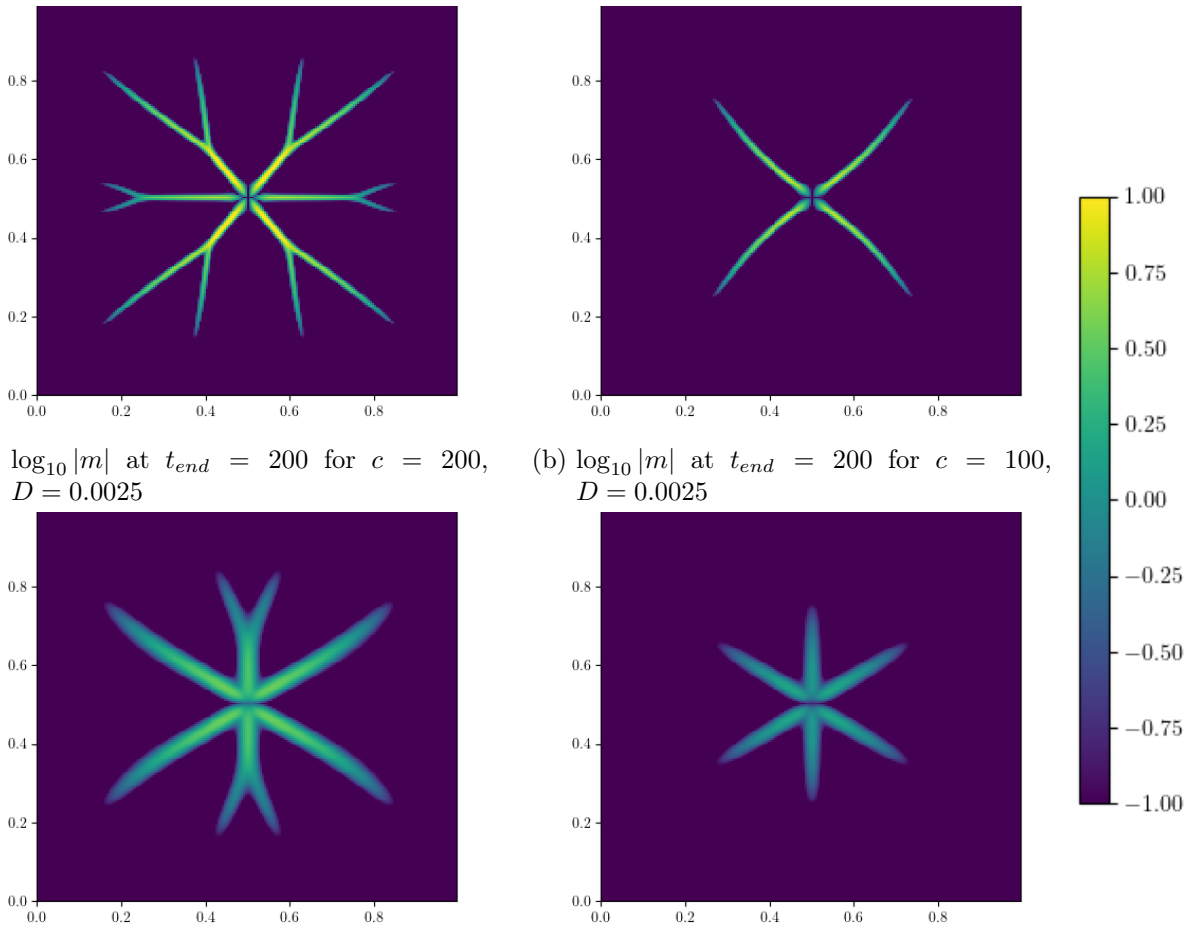

(a) $\log_{10}|m|$ at $t_{end} = 200$ for $c = 200$, $D = 0.0025$

(b) $\log_{10}|m|$ at $t_{end} = 200$ for $c = 100$, $D = 0.0025$

(c) $\log_{10}|m|$ at $t_{end} = 150$ for $c = 200$, $D = 0.0075$

(d) $\log_{10}|m|$ at $t_{end} = 150$ for $c = 100$, $D = 0.0075$

Figure 3.7: Comparison of numerical results for the conductivity m close to steady state for different values of the activation parameter c. The parameters chosen are $\gamma = 0.75, r = 0.1, \Delta t^k = 0.005$, m^A_{ini} and the internal sink S_{int}. Left column: $c = 200$. Right column: $c = 100$. Top row: $D = 0.0025$. Bottom row: $D = 0.0075$. Larger activation parameters result in thicker, more branched structures that extend further into the domain.

suppressing the fine details of the network. Hence, smaller diffusion constants form rich branching patterns, while larger diffusion enforces global uniformity. Moreover, we conclude from the figure that the exponent of the metabolic cost term γ controls the density of the network, that is, small values of γ give rise to sparse and tree-like patterns since the system minimises total metabolic cost, while increasing the value of γ leads to denser and more space-filling networks, and thus to broader regions of active flow. Overall, we deduce from these simulation results that complex networks emerge when *gamma* has a moderate value (i.e., $\gamma = 0.75$) and small values for the diffusion coefficient D. Large diffusion (i.e., $D = 0.01$) and large γ lead to nearly homogeneous steady states.

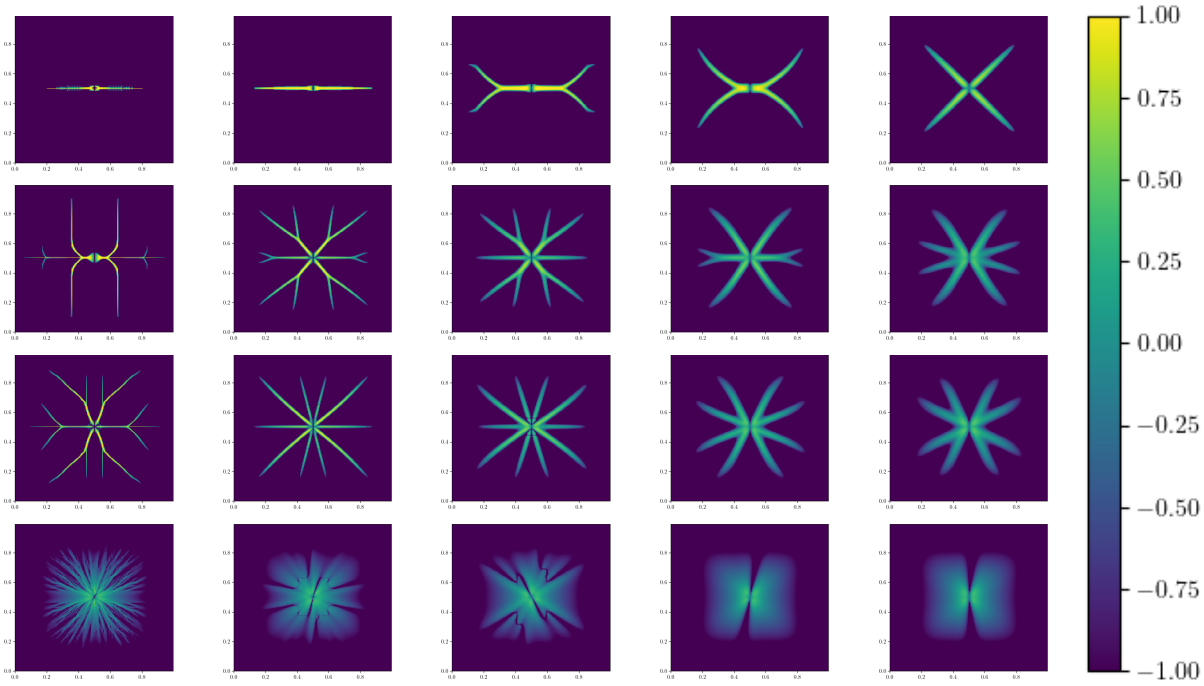

Figure 3.8: Value $\log_{10}|m|$ for $c = 200$, m^A_{ini}, and S_{int} (internal sink). From top to row γ varies in $\{0.5, 0.75, 0.8, 1\}$ and from left to right columns D varies in $\{0.001, 0.0025, 0.005, 0.0075, 0.01\}$. The network shown is the one at time $t_{end} = 200$ or when the algorithm broke due to an increase in energy or reaching the steady state.

3.6 Grid Convergence

To investigate whether the simulation outcomes depend on the chosen grid, as observed in [68], we perform a grid convergence test. For this, we will take values of c corresponding to 100 and 50 to reduce the computational time. We compute the order of convergence for the pressure p via the following formula

$$q_p \approx \frac{\ln\left(\frac{\|p_{\Delta x} - p_{\frac{\Delta x}{2}}\|_2}{\|p_{\frac{\Delta x}{2}} - p_{\frac{\Delta x}{4}}\|_2}\right)}{\ln 2},$$

where $p_{\Delta x}$ denotes the solution for p on a regular grid with grid size Δx. We define analogously $q_{\|m\|}$ and $q_{\|\nabla p\|}$.

We consider $\Omega = [0,1]^2$, $N_x = N_y \in \{50, 100, 200, 400\}$, $r = 0.1$, and $S = S_{\text{int}}$. Table 3.1 corresponds to the setup with $c = 100$, $\gamma = 0.75$, $D = 0.01$, $\Delta t = 0.05$ and m^A_{ini} and reports the rate q at increasing times (the coarsest run terminates at $t \approx 91$ due to reaching steady state). Table 3.2 considers the case $c = 50$, $\gamma = 1$, $D = 0.0025$ and m^{const}_{ini}. Table 3.3 considers the case with m^A_{ini} with factor 1000 instead of 10^4 in the exponential, $c = 50, \gamma = 1, D = 0.0025$. Missing numbers are either due to the simulations still running (i.e., Table 3.1) or that they terminated at an earlier time (i.e., Table 3.2 for $N = 50, 100, 200$ and $t = 35$ and $t = 40$ as well as $t = 40$ for $N = 100, 200, 400$).

The numerical method proposed utilises the FFT, the CG method, and the splitting method. The splitting method has order 1, whereas in the CG method, we can choose the desired accuracy.

	$N = 50, 100, 200$			$N = 100, 200, 400$			$N = 200, 400, 800$		
time t	$q_{\|m\|}$	$q_{\|\nabla p\|}$	q_p	$q_{\|m\|}$	$q_{\|\nabla p\|}$	q_p	$q_{\|m\|}$	$q_{\|\nabla p\|}$	q_p
5	6.6747	5.0983	5.6516	3.9922	3.8377	3.2919	3.4010	4.5286	5.6811
10	6.9849	5.0677	5.6942	3.7730	3.9284	3.4008	—	—	—
50	7.9296	6.3999	7.8724	3.6918	3.6324	2.8776	—	—	—
91	7.8778	6.3763	7.6062	4.2736	4.1772	4.0374	—	—	—

Table 3.1: Observed orders q for $c = 100,\ \gamma = 0.75,\ D = 0.01,\ \Delta t = 0.05,\ m^A_{\text{ini}},\ S_{\text{int}},\ N = N_x = N_y$.

	$N = 50, 100, 200$			$N = 100, 200, 400$			$N = 200, 400, 800$		
time $t[s]$	$q_{\|m\|}$	$q_{\|\nabla p\|}$	q_p	$q_{\|m\|}$	$q_{\|\nabla p\|}$	q_p	$q_{\|m\|}$	$q_{\|\nabla p\|}$	q_p
15	2.5533	2.209	2.7430	4.6220	3.7932	4.4483	8.2958	6.2632	6.8885
35	—	—	—	4.7246	3.7308	4.5646	8.3799	6.4396	6.9787
40	—	—	—	—	—	—	8.3838	6.4438	6.9735

Table 3.2: Observed orders q for $c = 100,\ \gamma = 1,\ D = 0.0025,\ \Delta t = 0.5,\ m^{const}_{ini},\ S_{\text{int}},\ N = N_x = N_y$.

	$N = 50, 100, 200$			$N = 100, 200, 400$			$N = 200, 400, 800$		
time $t[s]$	$q_{\|m\|}$	$q_{\|\nabla p\|}$	q_p	$q_{\|m\|}$	$q_{\|\nabla p\|}$	q_p	$q_{\|m\|}$	$q_{\|\nabla p\|}$	q_p
45	4.8019	2.5699	3.773	2.5099	2.7235	2.3999	6.6369	3.9876	5.5382
55	4.8009	2.5625	3.7567	2.5115	2.7251	2.3969	6.639	3.987	5.5368

Table 3.3: Observed orders q for $c = 100,\ \gamma = 1,\ D = 0.0025,\ \Delta t = 0.05$ with m^A_{ini} with factor 1000 instead of 10^4, $S_{\text{int}},\ N = N_x = N_y$.

Spectral methods have an exponential order of convergence. Due to this mixture of accuracies, it is not obvious to predict which should be the expected order of convergence of the method. However, so far, the numerical evidence shows that the method has a high order of convergence. It is in particular noticeable that no observable aliasing effects appear in the simulations.

3.7 Conclusions and Perspectives

In this paper, we considered the elliptic-parabolic model (3.1.1) to study the formation of biological networks. The model was derived as a continuum limit of the discrete Hu-Cai model and formulated as an L^2-gradient flow of a non-convex energy functional. In Section 3.2, we provided a detailed literature review on results and related models at the micro-, meso- and macroscopic scale.

We introduced a Fourier-based spectral splitting method for the network formation PDE (3.1.1) under periodic boundary conditions. The algorithm is built from (1) a splitting method for the conductivity m with (i) exact-in-time substeps for activation and relaxation, (ii) an exact diffusion step implemented with FFT, and (2) a CG method to solve the equation for the pressure p based on using FFT.

This combination yields a simple-to-implement solver with high spatial accuracy and scalability to 3D uniform grids. Our parameter studies recover qualitative features reported in the literature: diffusion D smooths and thickens networks, activation c enhances branching, and the

metabolic exponent γ tunes the sparsity/density of steady patterns. Grid convergence results support the accuracy of our approach.

Limitations and future directions of this work include:

- Time-step restriction due to the activation update (Remark 3.4.1); adaptive time-stepping strategies may be used in practice.
- The scheme is not unconditionally energy-stable; energy-decaying variants (e.g., semi-implicit or implicit substeps) could be hybridised with the current framework.
- Preconditioners beyond the constant-coefficient could further reduce CG iterations.
- Extension to 3D, which would benefit from improving the current computational time (either with adaptive time-steps or improved preconditioners as mentioned in the previous points).

Despite its limitations, the proposed method fills a practical niche among existing solvers: it is concise, fast, and robust enough for both qualitative and quantitative studies, and is easily extensible to 3D problems where network formation is particularly relevant for applications such as vascularisation.

4 Mean-Field Limit for a Network of Fibers

This chapter consists of results of an ongoing collaboration with Sara Merino-Aceituno.

Contents

Abstract

We provide a short, self-contained derivation of the kinetic equation for link-mediated fiber networks, recasting the proof in [15, 39] entirely in terms of empirical measures. The model features two-dimensional rod-like fibers with a repulsive potential, where fiber-fiber interactions happen through a network of linked fibers. With our formal derivation solely based on the empirical fiber distribution and the empirical link measure, we highlight the main assumptions that need to be proven to make the mean-field limit rigorous.

4.1 Introduction

This chapter revisits the model introduced by Degond et al. in [39] for the formation of fiber networks, designed to describe the fibrous component of the extracellular matrix in biological tissues, as in [90]. Understanding how fiber networks form and evolve is crucial for explaining tissue mechanics and function. The model we consider features two-dimensional, identical fiber elements of fixed length that can dynamically link and unlink; when linked, fibers tend to align with one another.

Our primary objective is to provide a formal, self-contained rederivation of the kinetic equation governing the system of interacting fiber elements by recasting the arguments of [15, 39]. Whereas the original derivation combines counting arguments, conditional probabilities, and interpretative reasoning to compute key expressions, our approach relies exclusively on the calculus of empirical measures. This shift in methodology clarifies the structure of the argument and clearly identifies the assumptions required to pass to the mean-field limit, and thereby represents a first step toward a complete mathematical justification. In particular, we highlight

the necessity of a bijection between the labels of the fibers and their positions. To justify this bijection when there is a finite number of fiber elements, we incorporate a short-range repulsive potential that accounts for volume exclusion between fiber elements. This prevents two fibers from occupying the same position.

The mean-field regime addressed in this work is nonstandard, since interactions do not arise from metric proximity but are mediated exclusively through dynamically created links between fibers. This induces an evolving network structure for which classical metric mean-field limits are not directly applicable. While there is a substantial literature on mean-field limits for interacting systems on graphs – most notably via graphon techniques – our framework is different as we do not consider a graphon in the limit of large number of fibers.

4.1.1 Structure of the Paper

The results presented in the following account only for the deterministic dynamics of the fiber system. However, for completeness, we present the full model as introduced in [39] in Section 4.2. The mean-field limit for the deterministic system is derived in Section 4.3. The key objects entering the limit – the empirical distribution of fibers and the empirical measure of links – are introduced in Section 4.3.1. Our main resultTheorem 4.3.3 is stated and discussed in Section 4.3.4. Finally, in Section 4.4 we give some concluding remarks and perspectives on future work.

4.2 Discrete Model for Fibers

As mentioned in the introduction, we consider only the fibrous elements of the extracellular matrix of a biological tissue. We assume that a fiber in the extracellular matrix is built out of many fiber elements, which link together to form a fiber. Therefore, to model the evolution of such a fiber network, we describe and extend a discrete model for the fiber elements first introduced by Degond et al [39]. In this model, we assume that fiber elements repel each other via a repulsive potential, accounting for volume exclusion interactions, and their position and orientation are subject to fluctuations or noise. Moreover, fibers can randomly link, when they are close enough, or unlink. When fibers link, they try to align with each other. In the context of the extracellular matrix, the linking and alignment account for the formation of larger fiber elements. By linking, fibers build up a network. Fiber unlinking accounts for breakage in the network. Therefore, the fiber network of the extracellular matrix is remodelled via this linking/unlinking process.

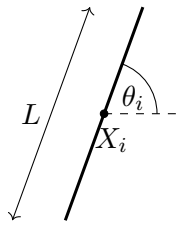

Figure 4.1: Fiber element with centre $X_i \in \mathbb{R}^2$, orientation $\theta_i \in [-\pi, \pi)$ and length L.

Hence, we consider a model of $N > 0$ fiber elements, represented as identical rods of length L. Each fiber element i, for $i = 1, \dots, N$, is characterised by by the position of its centre $X_i \in \mathbb{R}^2$ and its orientation, given by an angle $\theta_i \in [-\pi, \pi)$, see also Figure 4.1. The microscopic model

for the evolution of the positions $(X_i)_{i=1,\dots,N}$ and the orientations $(\theta_i)_{i=1,\dots,N}$ over time is given by a second-order system of stochastic differential equations:

$$\begin{aligned} \mathrm{d}X_i &= -\mu\nabla_{X_i}\left(W_{links} + W_{align} + W_{rep}\right)\,\mathrm{d}t + \sqrt{2D_x}\,\mathrm{d}B_i^t, \\ \mathrm{d}\theta_i &= -\lambda\partial_{\theta_i}\left(W_{links} + W_{align} + W_{rep}\right)\,\mathrm{d}t + \sqrt{2D_\theta}\,\mathrm{d}\tilde{B}_i^t, \end{aligned}$$

where ∇_{X_i} denotes the gradient with respect to X_i and ∂_{θ_i} the derivative with respect to θ_i. The terms involving ∇_{X_i} and ∂_{θ_i} correspond to gradient flow dynamics whose effect is to generate dynamics that minimise the sum of the potentials W_{links}, W_{align}, W_{rep}. The potential W_{links} describes the spring-like linking force between linked fibers; the potential W_{align} imposes that linked fibers align; the potential W_{rep} corresponds to a repulsive potential between fibers. In course of this work, we consider a general repulsive potential. Taking particular shapes for this potential into account will be part of future work. The positive coefficients $\mu, \lambda > 0$ parametrise the strength of the potentials. Finally, $(B_i^t)_{i=1,\dots,N}$ and $(\tilde{B}_i^t)_{i=1,\dots,N}$ correspond to independent Brownian motions that account for random effects or fluctuations, and $D_x \geq 0$, $D_\theta \geq 0$ are their diffusive constants.

We note that the discrete system (4.2.1) can be seen as the limit of a fourth-order system in the overdamped or inertialess regime. This is typical for many cellular systems since inertia effects in small-scale dynamics on a fluid tend to be negligible. We also note that the difference with respect to the model presented in [39] is that we are introducing a repulsive potential.

The dynamics given by (4.2.1) are, however, not complete. We also need to describe the stochastic process by which fibers link and unlink.

Creation and destruction of links between fibers. We consider a functional

$$\Gamma : \mathbb{R}^2 \times [-\pi, \pi) \times \mathbb{R}^2 \times [-\pi, \pi) \to \mathbb{R}_+$$

acting on two fibers, such that $\Gamma(X_i, \theta_i, X_j, \theta_j) = \Gamma(X_j, \theta_j, X_i, \theta_i)$ and

$$\Gamma(X_i, \theta_i, X_j, \theta_j) > 0,$$

if and only if two fibers are 'close' to each other. The definition of the closeness of fibers is a modelling assumption, a simple example could be the indicator function on the set $|X_i - X_j| < R$ for some radius $R > 0$.

This functional Γ can be interpreted as a 'switch' that activates if two specific fibers are capable of forming a link. Specifically, a pair of fibers (X_i, θ_i) and (X_j, θ_j) link at a rate

$$\tilde{\nu}_\ell := \frac{\nu_\ell}{N}\Gamma(X_i, \theta_i, X_j, \theta_j), \qquad \nu_\ell > 0.$$

At the same time, existing links disappear at a given rate $\nu_d > 0$. These linking and unlinking processes follow independent Poisson processes with the given rates $\tilde{\nu}_l$ and ν_d, respectively.

Linking potential W_{links}. We define $\eta(t)$ as the number of links at time t. Moreover, let $p \in \{1, \dots, \eta(t)\}$, then p indicates the p-th link $(i_p, j_p) \in \{1, \dots, N\}^2$ where the indices i_p and j_p denote the labels of the corresponding distinctive linked fibers (X_{i_p}, θ_{i_p}) and (X_{j_p}, θ_{j_p}). Note that we assume that only a single link between the fibers i and j can be formed. So, the unique points $X_{i_p}^p$ and $X_{j_p}^p$ of the intersection of the linked fiber pair (X_{i_p}, θ_{i_p}) and (X_{j_p}, θ_{j_p}),

as depicted in Figure 4.2, is determined by

$$X_{i_p}^p = X_{i_p} + \ell_{i_p}\omega_{i_p}, \qquad X_{j_p}^p = X_{j_p} + \ell_{j_p}\omega_{j_p},$$

where $\omega_i = \omega(\theta_i) := (\cos\theta_i, \sin\theta_i)$ is defined as the unit vector in the orientation of fiber i and $\ell_{i_p}, \ell_{j_p} \in [-L/2, L/2]$ to ensure that the linking point is located along the fiber. The quantities ℓ_{i_p} and ℓ_{j_p} are determined by

$$\ell_{i_p} = \bar{\ell}(X_{i_p}, \omega_{i_p}, X_{j_p}, \omega_{j_p}), \qquad \ell_{j_p} = \bar{\ell}(X_{j_p}, \omega_{j_p}, X_{i_p}, \omega_{i_p}),$$

with

$$\bar{\ell}(X_{i_p}, \omega_{i_p}, X_{j_p}, \omega_{j_p}) := \frac{\left|(X_{j_p} - X_{i_p}) \times \omega_{j_p}\right|}{\left|\omega_{i_p} \times \omega_{j_p}\right|},$$

at the time of the link's creation and stay constant throughout the lifetime of the link, i.e., $\frac{\mathrm{d}}{\mathrm{d}t}\ell_{i_p} = \frac{\mathrm{d}}{\mathrm{d}t}\ell_{j_p} = 0$ during this time interval. Here, $\times$ denotes the cross product between two vectors $a = (a_1, a_2)$ and $b = (b_1, b_2)$ and thus is given by $a \times b = a_1 b_2 - a_2 b_1$.

Throughout the lifetime of the link a spring-like restoring force is exerted at the attachment points $X_{i_p}^p$ and $X_{j_p}^p$, causing them to attract each other whenever they are displaced. The potential V acting on fibers $(X_1, \theta_1), (X_2, \theta_2)$ which is imposed by the spring-like restoring force is thus given by $V\colon \mathbb{R}^2 \times [-\pi, \pi) \times [-L/2, L/2] \times \mathbb{R}^2 \times [-\pi, \pi) \times [-L/2, L/2] \to \mathbb{R}_0^+$ with

$$V(X_1, \theta_1, \ell_1, X_2, \theta_2, \ell_2) \coloneqq \frac{\kappa}{2}|X_1 + \ell_1\omega(\theta_1) - (X_2 + \ell_2\omega(\theta_2))\,|^2.$$

Note, that V is symmetric in the sense that $V(X_i, \theta_i, l_i, X_j, \theta_j, l_j) = V(X_j, \theta_j, l_j, X_i, \theta_i, l_i)$ and that the linking potential of a fiber i to itself is zero by definition, i.e., $V(X_i, \theta_i, l_i, X_i, \theta_i, l_i) = 0$. The constant κ is a measure of the strength of the restoring force. Hence, the larger κ, the stronger the link is maintained.

Next, we formulate the linking potential of the system W_{links} as the sum over all existing links of the potential V,

$$W_{links} = \frac{1}{2}\sum_{p=1}^{\eta(t)} V(X_{i_p}, \theta_{i_p}, \ell_{i_p}, X_{j_p}, \theta_{j_p}, \ell_{j_p}).$$

As mentioned in the beginning, $\eta = \eta(t)$ is the number of links at time t. The factor $1/2$ prevents double counting of links, since each link appears twice – as (i, j) and (j, i).

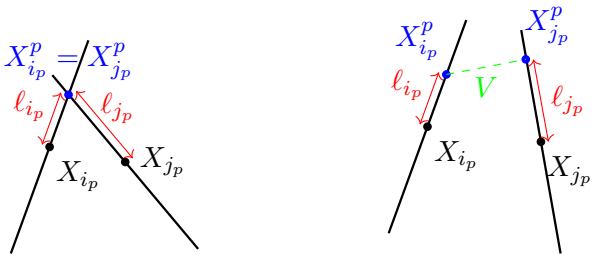

Figure 4.2: Left: two linked fiber elements with centres X_{i_p}, X_{j_p}, linking point $X_{i_p}^p = X_{j_p}^p$ and the distances from their centres to the linking point ℓ_{i_p} and ℓ_{j_p}.
Right: as the two linked fibers align, the spring-like restoring potential V pulls the displaced attachment points $X_{i_p}^p$ and $X_{j_p}^p$ back together.

Alignment potential W_{align}. Linked fiber elements are subject to an alignment force. This alignment models the fibers' resistance to bending. The binary alignment potential $b : [-\pi, \pi)^2 \to \mathbb{R}_0^+$ between two linked fiber elements only depends on the angles θ_1 and θ_2 and thus reads

$$b(\theta_1, \theta_2) = \alpha |\sin(\theta_1 - \theta_2)|^\beta,$$

where $\beta > 0$ is a modelling parameter and $\alpha > 0$ can be interpreted as a flexural modulus. Thus, it represents the stiffness of the fibers to bending.

Since this potential is only acting on linked fiber pairs, the total alignment potential W_{align} is therefore given by the sum of the alignment potential over all linked fiber pairs, i.e.,

$$W_{align} = \frac{1}{2} \sum_{p=1}^{\eta(t)} b(\theta_{i_p}, \theta_{j_p}).$$

Again, as for the linking potential, the factor $1/2$ is required since each link is counted twice.

Repulsive potential W_{rep}. Biologically, fibers, or rather fiber elements, possess a certain volume. Consequently, in the discrete setting, it actually is not possible for two fibers to occupy the same space at the same time. To model this, we introduce a repulsive potential $\psi^R(X_i, \theta_i, X_j, \theta_j) : \mathbb{R}^2 \times [-\pi, \pi) \times \mathbb{R}^2 \times [-\pi, \pi) \to \mathbb{R}$ between two fibers, (X_i, θ_i) and (X_j, θ_j), acting on their positions and orientations. In the simplest case, one could consider a potential that depends only on the distance between the centres of the fibers and is non-zero in the region $|X_i - X_j| < R$, for some radius $R > 0$. However, this sort of radial potential does not capture the anisotropy of the particles. For this reason, anisotropic potentials like the Berne-Pechukas potential [19] or an anisotropic repulsive potential of Gaussian type as introduced in Chapter 2 and [86] are more appropriate.

Generally, we assume that ψ^R is non-negative and symmetric, i.e., $\psi^R(X_i, \theta_i, X_j, \theta_j) = \psi^R(X_j, \theta_j, X_i, \theta_i) \geq 0$, with $R > 0$ giving a typical interaction distance. Hence, the position X_i of the corresponding fiber element i is unique for all $i \in \{1, \dots, N\}$. We also assume the repulsive potential acting on fiber element i itself is zero, i.e., $\psi^R(X_i, \theta_i, X_i, \theta_i) = 0$.

The repulsive potential of the whole system W_{rep} is thus defined as

$$W_{rep} = \frac{1}{N} \sum_{i,j=1}^{N} \psi^R(X_i, \theta_i, X_j, \theta_j).$$

A comment on the random movement (noise). Fibers are part of physiological tissues. To be able to account for random movement of this tissue, we include random positional and orientational motion of the fiber elements, i.e., Brownian motions B_i^t and $\tilde{B}_i^t$ acting on positions X_i and orientations θ_i with diffusion constants D_x and D_θ, respectively.

Final equations. With the previous notations, we recast system (4.2.1) to describe the dynamics within any time interval between two linking and unlinking processes of fibers, which

implies that $\eta(t)$, ℓ_{i_p} and ℓ_{j_p} are constant within the considered time interval:

$$\begin{aligned}
\mathrm{d}X_i = &-\frac{\mu}{2}\nabla_{X_i}\Bigg(\sum_{\substack{p=1\\ i_p=i}}^{\eta} V\left(X_{i_p},\theta_{i_p},\ell_{i_p},X_{j_p},\theta_{j_p},\ell_{j_p}\right)\\
&\qquad + \sum_{\substack{p=1\\ j_p=i}}^{\eta} V\left(X_{i_p},\theta_{i_p},\ell_{i_p},X_{j_p},\theta_{j_p},\ell_{j_p}\right)\Bigg)\,\mathrm{d}t\\
&- \frac{\mu}{N}\sum_{j=1}^{N}\nabla_{X_i}\psi^R(X_i,\theta_i,X_j,\theta_j)\,\mathrm{d}t + \sqrt{2D_x}\,\mathrm{d}B_i^t,\\
\mathrm{d}\theta_i = &-\frac{\lambda}{2}\partial_{\theta_i}\Bigg(\sum_{\substack{p=1\\ i_p=i}}^{\eta}(V+b)\left(X_{i_p},\theta_{i_p},\ell_{i_p},X_{j_p},\theta_{j_p},\ell_{j_p}\right)\\
&\qquad + \sum_{\substack{p=1\\ j_p=i}}^{\eta}(V+b)\left(X_{i_p},\theta_{i_p},\ell_{i_p},X_{j_p},\theta_{j_p},\ell_{j_p}\right)\Bigg)\,\mathrm{d}t\\
&- \frac{\lambda}{N}\sum_{j=1}^{N}\partial_{\theta_i}\psi^R(X_i,\theta_i,X_j,\theta_j)\,\mathrm{d}t + \sqrt{2D_\theta}\,\mathrm{d}\tilde{B}_i^t.
\end{aligned}$$

4.3 Mean-Field Limit for the Deterministic Dynamics

In this section, we will state and prove our main result, Theorem 4.3.3. Throughout this section, we will solely focus on the deterministic terms of the discrete system. Therefore, we consider a time interval with no link creation or destruction taking place, and thus neglect the Poisson linking and unlinking process. Moreover, we assume no random noise or fluctuation and set the diffusion constants $D_x = D_\theta = 0$.

4.3.1 Empirical Measures Associated to the Discrete System

In the following, we define empirical measures that enable the particle system to be reformulated in a manner that simplifies the mean-field derivation.

Empirical distribution of fiber elments. The empirical distribution of the fiber elements $f^N = f^N(t,x,\theta)$ for $t \geq 0, x \in \mathbb{R}^2$ and $\theta \in [-\pi,\pi)$ is given by

$$f^N(t,x,\theta) = \frac{1}{N}\sum_{i=1}^{N}\delta_{(X_i(t),\theta_i(t))}(x,\theta),$$

where $\delta_{(X_i(t),\theta_i(t))}(x,\theta) = \delta_{X_i(t)}(x)\delta_{\theta_i(t)}(\theta)$ represents the Dirac delta distribution on $\mathbb{R}^d\times[-\pi,\pi)$ located at $(X_i(t),\theta_i(t))$ at time t.

Empirical measure for the links. Next, for $t \geq 0$, $x,y \in \mathbb{R}^2$, $\theta_x,\theta_y \in [-\pi,\pi)$, $\ell_x,\ell_y \in [-L/2, L/2]$ we define the empirical measure $g^{K,N} = g^{K,N}(t,x,\theta_x,\ell_x,y,\theta_y,\ell_y)$ for the

links of fiber elements by

$$g^{K,N}(t,x,\theta_x,\ell_x,y,\theta_y,\ell_y) := \frac{1}{2K}\sum_{p=1}^{\eta(t)} \delta_{[(X_{i_p}(t),\theta_{i_p},\ell_{i_p});(X_{j_p}(t),\theta_{j_p},\ell_{j_p})]}(x,\theta_x,\ell_x,y,\theta_y,\ell_y),$$

where $\eta(t)$ is the number of links at time t and K is the initial number of links at time $t=0$, i.e., $K=\eta(0)$. Instead of taking the average regarding to the current number of links $\eta(t)$, we rather consider averaging via the factor $1/K$, which sets the number of links at time t in relation to the initial number of links. Notice, in particular, that $g^{K,N}$ is an empirical measure, but not an empirical distribution. Moreover,

$$\begin{aligned}\delta_{[(x,\theta_x,\ell_x);(y,\theta_y,\ell_y)]}(z,\theta_z,\ell_z,u,\theta_u,\ell_u) :=& \\ \delta_{(x,\theta_x,\ell_x,y,\theta_y,\ell_y)}(z,\theta_z,\ell_z,u,\theta_u,\ell_u) &+ \delta_{(y,\theta_y,\ell_y,x,\theta_x,\ell_x)}(z,\theta_z,\ell_z,u,\theta_u,\ell_u).\end{aligned}$$

Recall that p denotes the p-th link at time t, with i_p and j_p denoting the labels of the two distinctive fiber elements forming this link. Since the link relation is symmetric – (i_p,j_p) and (j_p,i_p) represent the same link – we include the factor $1/2$ to avoid double counting. Also, with this definition, $g^{K,N}$ is symmetric, i.e.,

$$g^{K,N}(t,x,\theta_x,\ell_x,y,\theta_y,\ell_y) = g^{K,N}(t,y,\theta_y,\ell_y,x,\theta_x,\ell_x).$$

In the sequel, we will focus only on the deterministic dynamics. However, one can formally add the stochastic terms arising from the linking and unlinking process. For completeness, we explain the effect of these jump processes on $g^{K,N}$ in the appendix.

In this section, we will formally compute the mean-field limit as $K,N\to\infty$. The goal is to derive equations for the probability density $f=f(t,x,\theta_x)$ of particles at position x with orientation θ_x at time t for the fiber particles and for the measure $g=g(t,x,\theta_x,\ell_x,y,\theta_y,\ell_y)$ of the links between fibers at states (x,θ_x) and (y,θ_y) with linking distances ℓ_x and ℓ_y respectively at time t. To do this, we first introduce some convenient notation in the next section and explain the relation between f^N and $g^{K,N}$ in the subsequent section.

4.3.2 Compact Notations

To make the proofs and statements easier to read, we introduce some convenient notation in this section. We consider the following integration domains:

$$H := \mathbb{R}^2\times[-\pi,\pi)\times[-L/2,L/2]\times\mathbb{R}^2\times[-\pi,\pi)\times[-L/2,L/2], \tag{4.3.1}$$

$$H_f := \mathbb{R}^2\times[-\pi,\pi), \tag{4.3.2}$$

$$H_1 := [-L/2,L/2]\times[-L/2,L/2]\times[-\pi,\pi)\times\mathbb{R}^2. \tag{4.3.3}$$

In addition, we introduce the compact variable $Z_i=(X_i,\theta_i)$. This allows us to express

equations (4.2.2) with $D_x = D_\theta = 0$ in a more concise form as

$$\begin{aligned} \mathrm{d}Z_i =& \frac{1}{2}\nabla_{Z_i}\left(\sum_{\substack{p=1\\ i_p=i}}^{\eta} W\left(Z_{i_p},\ell_{i_p},Z_{j_p},\ell_{j_p}\right)+\sum_{\substack{p=1\\ j_p=i}}^{\eta} W\left(Z_{i_p},\ell_{i_p},Z_{j_p},\ell_{j_p}\right)\right)\mathrm{d}t \\ &-\frac{1}{N}\sum_{j=1}^{N}\nabla_{Z_i}\psi^R\left(Z_i,Z_j\right)\mathrm{d}t, \end{aligned} \tag{4.3.4}$$

with

$$W\left(Z_i,\ell_i,Z_j,\ell_j\right) = -\left(V\left(Z_i,\ell_i,Z_j,\ell_j\right)+b\left(\theta_i,\theta_j\right)\right),$$

and $\nabla_{Z_i} = (\mu\nabla_{X_i}, \lambda\partial_{\theta_i})$.

4.3.3 Relation between f^N and $g^{K,N}$

In the following, we investigate the relation between the empirical distribution of the fibers f^N and the empirical measure of the links $g^{K,N}$. For this, we define

$$\tilde{h}^N\colon \mathbb{R}_0^+\times\{1,\dots,N\}\times\{1,\dots,N\}\times[-L/2,L/2]\times[-L/2,L/2]\to\mathcal{D}\left([-L/2,L/2]\times[-L/2,L/2]\right),$$

where $\mathcal{D}$ denotes the space of distributions, such that

$$\tilde{h}^N\left(t,i,j,\cdot,\star\right) = \begin{cases} 0 \text{ if } i \text{ and } j \text{ are not linked,} \\ \displaystyle\sum_{\substack{p=1\\ i_p=i\\ j_p=j}}^{\eta(t)} \delta_{\ell_{i_p}(t)}(\cdot)\delta_{\ell_{j_p}(t)}(\star) \qquad \text{otherwise.} \end{cases}$$

Assumption 1. There exists a bijection between labels and the values (i.e., the positions) that the fibers take.

This assumption is reasonable for finite N as we expect the repulsive potential to impede that two fibers occupy the same position. Thus, different labels i, j map to different positions X_i and X_j and vice versa.

Under Assumption 1 we define $h^N : \mathbb{R}_0^+ \times H \to \mathcal{D}\left([-L/2,L/2]\times[-L/2,L/2]\right)$ such that

$$h^N\left(t,Z_i,\ell_1,Z_j,\ell_2\right) = \tilde{h}^N\left(t,i,j,\ell_1,\ell_2\right).$$

Notice that h^N is symmetric in its variables, i.e,

$$h^N\left(t,Z_i,\ell_1,Z_j,\ell_2\right) = h^N\left(t,Z_j,\ell_2,Z_i,\ell_1\right).$$

Next, via h^N, we will set the empirical link measure $g^{K,N}$ in relation to the empirical fiber distribution f^N.

Lemma 4.3.1. *Assume 1. In the space of continuous and compactly supported test functions $\varphi \in C_c^\infty(H)$ that are symmetric ($\varphi\left(z,\ell_z,w,\ell_w\right) = \varphi\left(w,\ell_w,z,\ell_z\right)$) it holds, in distribution sense:*

$$Nh^N\left(t,z,\ell_z,w,\ell_w\right)f^N(t,z)f^N(t,w) = \frac{K}{N}g^{K,N}\left(t,z,\ell_z,w,\ell_w\right).$$

Proof. On the one hand, it holds that

$$\begin{aligned}
A &:= \sum_{i=1}^{N}\sum_{j=1}^{N}\int_{[-L/2,L/2]^2} \varphi\left(Z_i,\ell_1,Z_j,\ell_2\right) h^N\left(Z_i,\ell_1,Z_j,\ell_2\right)\,\mathrm{d}\ell_1\,\mathrm{d}\ell_2 \\
&= \sum_{i=1}^{N}\sum_{j=1}^{N}\sum_{\substack{p=1\\ i_p=i\\ j_p=j}}^{\eta}\int_{[-L/2,L/2]^2} \varphi\left(Z_i,\ell_1,Z_j,\ell_2\right)\delta_{\ell_{i_p}}(\ell_1)\delta_{\ell_{j_p}}(\ell_2)\,\mathrm{d}\ell_1\,\mathrm{d}\ell_2 \\
&= \sum_{i=1}^{N}\sum_{j=1}^{N}\sum_{\substack{p=1\\ i_p=i\\ j_p=j}}^{\eta} \varphi\left(Z_i,\ell_i,Z_j,\ell_j\right) \\
&= \frac{1}{2}\sum_{i=1}^{N}\sum_{j=1}^{N}\sum_{\substack{p=1\\ i_p=i\\ j_p=j}}^{\eta} \left[\varphi\left(Z_i,\ell_i,Z_j,\ell_j\right)+\varphi\left(Z_j,\ell_j,Z_i,\ell_i\right)\right] \\
&= \frac{1}{2}\sum_{p=1}^{\eta}\sum_{i=1}^{N}\sum_{j=1}^{N}\tilde{\delta}_{i_p=i}\tilde{\delta}_{j_p=j}\left[\varphi\left(Z_i,\ell_i,Z_j,\ell_j\right)+\varphi\left(Z_j,\ell_j,Z_i,\ell_i\right)\right] \\
&= \frac{1}{2}\sum_{p=1}^{\eta}\left[\varphi\left(Z_{i_p},\ell_{i_p},Z_{j_p},\ell_{j_p}\right)+\varphi\left(Z_{j_p},\ell_{j_p},Z_{i_p},\ell_{i_p}\right)\right] \\
&= K\int_H \varphi\left(z,\ell_z,w,\ell_w\right) g^{K,N}\left(t,z,\ell_z,w,\ell_w\right)\,\mathrm{d}z\,\mathrm{d}\ell_z\,\mathrm{d}w\,\mathrm{d}\ell_w,
\end{aligned}$$

where $\tilde{\delta}$ is the Kronecker delta. In the fourth equality we used the symmetry of φ.

On the other hand, using the definition of f^N for expression A, we also have

$$A = N^2\int_H \varphi\left(z,\ell_z,w,\ell_w\right) h^N\left(z,\ell_z,w,\ell_w\right) f^N(t,z)f^N(t,w)\,\mathrm{d}z\,\mathrm{d}\ell_z\,\mathrm{d}w\,\mathrm{d}\ell_w.$$

By combining the two expressions, we obtain the result. ∎

In the sequel, we will assume the following:

Assumption 2. Suppose that $K/N \to \xi$ for $\xi \in (0,\infty)$ as $K, N \to \infty$. Moreover, as $K, N \to \infty$, we assume that the limits $f^N \to f$ and $g^{K,N} \to g$ hold for some regular functions $f,\ g$ ('regular' in the sense that we can define their derivatives) and that the limits are strong enough so that they can be exchanged with integrals. Additionally, we assume that $Nh^N \to h$ as $N \to \infty$.

Corollary 4.3.2. *Suppose that Assumptions 1 and 2 hold. In the space of compactly supported continuous test functions $\varphi \in C_c^\infty(H)$ that are symmetric $(\varphi\left(z,\ell_z,w,\ell_w\right) = \varphi\left(w,\ell_w,z,\ell_z\right))$ it holds, in distribution sense:*

$$h\left(z,\ell_z,w,\ell_w\right) f(t,z)f(t,w) = \xi g\left(t,z,\ell_z,w,\ell_w\right),$$

in the limit $N, K \to \infty$.

The result is a direct application of Lem. 4.3.1.

4.3.4 Main Result

In the following, we will state and prove our main result, Theorem 4.3.3, which gives the kinetic equations for the probability distribution f of the fibers and link measure g. As mentioned, we will only focus on the deterministic terms in the sequel and thus not only assume that the diffusion constants $D_x = D_\theta = 0$ for the stochastic terms of the discrete system but also neglect the Poisson processes of linking and unlinking of fiber elements as we suppose to only consider a time interval where no creation or destruction of links take place.

Theorem 4.3.3 (Mean-field limit)**.** *Suppose that Assumptions 1 and 2 hold. Moreover, assume that $D_x = D_\theta = 0$ and that we consider a time interval during which no creation or destruction of links take place, and hence $\eta(t)$, ℓ_x and ℓ_y are constant. Then, $f = f(t, x, \theta_x)$ and $g = g(t, x, \theta_x, \ell_x, y, \theta_y, \ell_y)$ satisfy the following equations:*

$$\partial_t f - \nabla_x \cdot F_1 - \partial_\theta F_2 - \mu \nabla_x \cdot (\nabla_x \psi^R * f) - \lambda \partial_\theta (\partial_\theta \psi^R * f) = 0, \tag{4.3.5}$$

where '$*$' denotes a convolution and

$$\begin{aligned}
\frac{\mathrm{d}g}{\mathrm{d}t} - \Big(& \nabla_x \cdot \big(\frac{g}{f(t,x,\theta_x)} F_1(t,x,\theta_x) \big) + \mu \nabla_x \cdot \Big(g(\nabla_x \psi^R * f)(t,x,\theta_x) \Big) \\
& + \nabla_y \cdot \big(\frac{g}{f(t,y,\theta_y)} F_1(t,y,\theta_y) \big) + \mu \nabla_y \cdot \Big(g(\nabla_y \psi^R * f)(t,y,\theta_y) \Big) \\
- \Big(& \partial_{\theta_x} \big(\frac{g}{f(t,x,\theta_x)} F_2(t,x,\theta_x) \big) + \lambda \partial_{\theta_x} \Big(g(\partial_{\theta_x} \psi^R * f)(t,x,\theta_x) \Big) \\
& + \partial_{\theta_y} \big(\frac{g}{f(t,y,\theta_y)} F_2(t,y,\theta_y) \big) + \lambda \partial_{\theta_y} \Big(g(\partial_{\theta_y} \psi^R * f)(t,y,\theta_y) \Big) = 0,
\end{aligned} \tag{4.3.6}$$

with

$$\begin{cases}
F_1(t,x,\theta_x) = \mu \xi \displaystyle\int_{H_1} (g \nabla_x V)(t,x,\theta_x,\ell_x,y,\theta_y,\ell_y) \, \mathrm{d}\ell_x \, \mathrm{d}\ell_y \, \mathrm{d}\theta_y \, \mathrm{d}y, \\
F_2(t,x,\theta_x) = \lambda \xi \displaystyle\int_{H_1} \big(g(\partial_{\theta_x} V + \partial_{\theta_x} b) \big)(t,x,\theta_x,\ell_x,y,\theta_y,\ell_y) \, \mathrm{d}\ell_x \, \mathrm{d}\ell_y \, \mathrm{d}\theta_y \, \mathrm{d}y,
\end{cases}$$

where H_1 is given in (4.3.3)*. Notice that we define $g/f(t,x,\theta_x) = 0$ if $f(t,x,\theta_x) = 0$.*

Remark 4.3.1 (Comparison with the equations from Reference [39])**.** *We obtain the same equations as stated in reference [39] with the extra terms in ψ^R since we also consider a repulsive potential between fiber elements acting on their positions and orientations.*

In order to prove Theorem 4.3.3, we will use various lemmas:

Lemma 4.3.4. *Suppose Assumption 1 holds. Let $\varphi \in C_c^\infty(H_f)$ with $\varphi = \varphi(z)$ be a compactly supported continuous test function with H_f defined in* (4.3.2)*, and let $U \in C^1(H)$, $U = U(z, \ell_z, w, \ell_w)$ with H given in* (4.3.1) *be a continuous function such that U is symmetric in the sense that $U(z, \ell_z, w, \ell_w) = U(w, \ell_w, z, \ell_z)$, then*

$$\frac{1}{2}\frac{1}{N}\sum_{i=1}^{N}\nabla_{Z_i}\varphi(Z_i)\cdot\nabla_{Z_i}\left(\sum_{\substack{p=1\\ i_p=i}}^{\eta}U(Z_{i_p},\ell_{i_p},Z_{j_p},\ell_{j_p})+\sum_{\substack{p=1\\ j_p=i}}^{\eta}U(Z_{i_p},\ell_{i_p},Z_{j_p},\ell_{j_p})\right) \tag{4.3.7}$$
$$=\frac{K}{N}\int_H\nabla_z\varphi(z)\cdot\nabla_z U(z,\ell_z,w,\ell_w)g^{K,N}\left(t,z,\ell_z,w,\ell_w\right)\,\mathrm{d}z\,\mathrm{d}\ell_z\,\mathrm{d}w\,\mathrm{d}\ell_w.$$

Lemma 4.3.5. *Suppose Assumption 1 holds and, for simplification, that $\psi^R\equiv 0$. Then, for all continuous and compactly supported test functions $\tilde{\varphi}=\tilde{\varphi}\left(z,l_z,w,l_w\right),\tilde{\varphi}\in C_c^\infty(H)$ which are symmetric ($\tilde{\varphi}\left(z,\ell_z,w,\ell_w\right)=\tilde{\varphi}\left(w,\ell_w,z,\ell_z\right)$), it holds that*

$$\begin{aligned}
&\frac{1}{K}\sum_{p=1}^{\eta}\left(\nabla_{Z_{i_p}}\tilde{\varphi}\left(Z_{i_p},\ell_{i_p},Z_{j_p},\ell_{j_p}\right)\cdot\frac{dZ_{i_p}(t)}{dt}+\nabla_{Z_{j_p}}\tilde{\varphi}\left(Z_{i_p},\ell_{i_p},Z_{j_p},\ell_{j_p}\right)\cdot\frac{dZ_{j_p}(t)}{dt}\right)\\
&=\int_H g^{K,N}\left(t,z,\ell_z,w,\ell_w\right)\nabla_z\tilde{\varphi}\left(z,\ell_z,w,\ell_w\right)\\
&\qquad\cdot\left(\nabla_z\int_{H_1}W\left(z,\ell_1,u,\ell_2\right)\;Nh^N\left(z,\ell_1,u,\ell_2\right)f^N(t,u)d\ell_1d\ell_2du\right)dzd\ell_zdwd\ell_w\\
&\quad+\int_H g^{K,N}\left(t,z,\ell_z,w,\ell_w\right)\nabla_w\tilde{\varphi}\left(z,\ell_z,w,\ell_w\right)dzd\ell_zdwd\ell_w\\
&\qquad\cdot\left(\nabla_w\int_{H_1}W\left(u,\ell_1,w,\ell_2\right)\;Nh^N\left(u,\ell_1,w,\ell_2\right)f^N(t,u)d\ell_1d\ell_2du\right)dzd\ell_zdwd\ell_w
\end{aligned}$$

Proof of Theorem 4.3.3. First, we compute the mean-field limit for f^N as $N,K\to\infty$. We consider $\varphi\in C_c^\infty(H_f)$ to be a compactly supported continuous test function, then

$$\frac{\mathrm{d}}{\mathrm{d}t}\int_{H_f}\varphi(z)f^N(t,z)\,\mathrm{d}z=\frac{\mathrm{d}}{\mathrm{d}t}\left(\frac{1}{N}\sum_{i=1}^{N}\varphi(Z_i(t))\right)=\frac{1}{N}\sum_{i=1}^{N}\nabla_{Z_i}\varphi(Z_i(t))\cdot\frac{\mathrm{d}Z_i(t)}{\mathrm{d}t},$$

Inserting expression (4.3.4) for ${}^{\mathrm{d}Z_i(t)}/_{\mathrm{d}t}$ and noting that η is constant during the considered time interval yields

$$\begin{aligned}
\frac{\mathrm{d}}{\mathrm{d}t}\int_{H_f}\varphi(z)f^N(t,z)\,\mathrm{d}z=&\frac{1}{2N}\sum_{i=1}^{N}\nabla_{Z_i}\varphi(Z_i)\cdot\nabla_{Z_i}\left(\sum_{\substack{p=1\\ i_p=i}}^{\eta}W\left(Z_{i_p},\ell_{i_p},Z_{j_p},\ell_{j_p}\right)\right)\\
&+\frac{1}{2N}\sum_{i=1}^{N}\nabla_{Z_i}\varphi(Z_i)\cdot\nabla_{Z_i}\left(\sum_{\substack{p=1\\ j_p=i}}^{\eta}W\left(Z_{i_p},\ell_{i_p},Z_{j_p},\ell_{j_p}\right)\right)\\
&-\frac{1}{N}\sum_{i=1}^{N}\nabla_{Z_i}\varphi(Z_i)\cdot\left(\frac{1}{N}\sum_{j=1}^{N}\nabla_{Z_i}\psi^R(Z_i,Z_j)\right).
\end{aligned}$$

Applying Lemma 4.3.4 and the definition of f^N leads to

$$\begin{aligned}\frac{\mathrm{d}}{\mathrm{d}t}\int_{H_f}\varphi(z)f^N(t,z)\,\mathrm{d}z =& \frac{K}{N}\int_H \nabla_z\varphi(z)\cdot\nabla_z W\left(z,\ell_z,w,\ell_w\right)g^{K,N}\left(t,z,\ell_z,w,\ell_w\right)\,\mathrm{d}z\,\mathrm{d}\ell_z\,\mathrm{d}w\,\mathrm{d}\ell_w\\ &-\int_{H_f}\nabla_z\varphi(z)\cdot\left(\int_{H_f}\nabla_z\psi^R(z,w)f^N(t,w)\,\mathrm{d}w\right)f^N(t,z)\,\mathrm{d}z.\end{aligned}$$

Now, taking the limit $N,K\to\infty$, and using the assumption that $K/N\to\xi$, $f^N\to f$, $g^{K,N}\to g$, we obtain, after integration by parts:

$$\begin{aligned}\int_{H_f}\varphi(z)\partial_t f(t,z)\,\mathrm{d}z =& -\xi\int_H\varphi(z)\nabla_z\cdot\left(\nabla_z W\left(z,\ell_z,w,\ell_w\right)g\left(t,z,\ell_z,w,\ell_w\right)\right)\,\mathrm{d}z\,\mathrm{d}\ell_z\,\mathrm{d}w\,\mathrm{d}\ell_w\\ &+\int_{H_f}\varphi(z)\nabla_z\cdot\left(\int_{H_f}\left(\nabla_z\psi^R(z,w)f(t,w)\,\mathrm{d}w\right)f(t,z)\right)\,\mathrm{d}z.\end{aligned}$$

Considering that $W=-(V+b)$ and rewriting ∇_Z and Z back to the original variables, the previous equation corresponds to the kinetic equation for $f=f(t,x,\theta)$ in (4.3.5) in weak form.

Next, we derive the kinetic equation for the link measure $g=g(t,z,\ell_z,w,\ell_w)$. Analogously as done for f^N, we consider a continuous compactly supported test function $\tilde{\varphi}\in C_c^\infty(H)$, which is symmetric such that $\tilde{\varphi}(z,\ell_z,w,\ell_w)=\tilde{\varphi}(w,\ell_w,z,\ell_z)$. Then, taking the symmetry of $\tilde{\varphi}$ into account, we have that

$$\begin{aligned}&\int_H\tilde{\varphi}(z,\ell_z,w,\ell_w)g^{K,N}(t,z,\ell_z,w,\ell_w)\,\mathrm{d}z\,\mathrm{d}\ell_z\,\mathrm{d}w\,\mathrm{d}\ell_w\\ &=\frac{1}{2K}\left(\sum_{p=1}^{\eta}\tilde{\varphi}\left(Z_{i_p},\ell_{i_p},Z_{j_p},\ell_{j_p}\right)+\sum_{p=1}^{\eta}\tilde{\varphi}\left(Z_{j_p},\ell_{j_p},Z_{i_p},\ell_{i_p}\right)\right)\\ &=\frac{1}{K}\sum_{p=1}^{\eta}\tilde{\varphi}\left(Z_{i_p},\ell_{i_p},Z_{j_p},\ell_{j_p}\right).\end{aligned}$$

As a next step, we differentiate the integral above with respect to time t, refer to $\frac{\mathrm{d}\ell_i(t)}{\mathrm{d}t}=0$ in the here considered time interval and apply Lemma 4.3.5. Hence, we obtain

$$\begin{aligned}&\frac{\mathrm{d}}{\mathrm{d}t}\int_H\tilde{\varphi}(z,\ell_z,w,\ell_w)g^{K,N}(t,z,\ell_z,w,\ell_w)\,\mathrm{d}z\,\mathrm{d}\ell_z\,\mathrm{d}w\,\mathrm{d}\ell_w\\ &=\frac{1}{K}\frac{\mathrm{d}}{\mathrm{d}t}\left(\sum_{p=1}^{\eta}\tilde{\varphi}\left(Z_{i_p},\ell_{i_p},Z_{j_p},\ell_{j_p}\right)\right)\\ &=\frac{1}{K}\left[\sum_{p=1}^{\eta}\nabla_{Z_{i_p}}\tilde{\varphi}\left(Z_{i_p},\ell_{i_p},Z_{j_p},\ell_{j_p}\right)\cdot\frac{\mathrm{d}Z_{i_p}(t)}{\mathrm{d}t}\right.\\ &\qquad\left.+\sum_{p=1}^{\eta}\nabla_{Z_{j_p}}\tilde{\varphi}\left(Z_{i_p},\ell_{i_p},Z_{j_p},\ell_{j_p}\right)\cdot\frac{\mathrm{d}Z_{j_p}(t)}{\mathrm{d}t}\right]\\ &=\int_H g^{K,N}\left(t,z,\ell_z,w,\ell_w\right)\nabla_z\tilde{\varphi}\left(z,\ell_z,w,\ell_w\right)\end{aligned}$$

$$\cdot \left(\int_{H_1} \nabla_z W(z,\ell_1,u,\ell_2) N h^N(z,\ell_1,u,\ell_2) f^N(t,u)\,\mathrm{d}\ell_1\,\mathrm{d}\ell_2\,\mathrm{d}u \right) \mathrm{d}z\,\mathrm{d}\ell_z\,\mathrm{d}w\,\mathrm{d}\ell_w$$
$$- \int_H g^{K,N}(t,z,\ell_z,w,\ell_w)\,\nabla_z\tilde{\varphi}(z,\ell_z,w,\ell_w) \cdot \left(\int_{H_f} \nabla_z \psi^R(z,u) f^N(t,u)\,\mathrm{d}u \right) \mathrm{d}z\,\mathrm{d}\ell_z\,\mathrm{d}w\,\mathrm{d}\ell_w$$

$$+ \int_H g^{K,N}(t,z,\ell_z,w,\ell_w)\,\nabla_w\tilde{\varphi}(t,z,\ell_z,w,\ell_w)$$
$$\cdot \left(\int_{H_1} \nabla_w W(u,\ell_1,w,\ell_2) N h^N(u,\ell_1,w,\ell_2) f^N(t,u)\,\mathrm{d}\ell_1\,\mathrm{d}\ell_2\,\mathrm{d}u \right) \mathrm{d}z\,\mathrm{d}\ell_z\,\mathrm{d}w\,\mathrm{d}\ell_w$$
$$- \int_H g^{K,N}(t,z,\ell_z,w,\ell_w)\,\nabla_w\tilde{\varphi}(z,\ell_z,w,\ell_w) \cdot \left(\int_{H_f} \nabla_w \psi^R(u,w) f^N(t,u)\,\mathrm{d}u \right) \mathrm{d}z\,\mathrm{d}\ell_z\,\mathrm{d}w\,\mathrm{d}\ell_w.$$

Now, taking the limit $N, K \to \infty$, $g^{K,N} \to g$, $f^N \to f$ by Assumption 2 and applying Corollary 4.3.2 we have that

$$(Nh^N)(u,\ell_1,w,\ell_2) \to \xi \frac{g(u,\ell_1,w,\ell_2)}{f(u)f(w)}.$$

We eventually obtain, after integration by parts, that

$$\int_H \tilde{\varphi}(z,\ell_z,w,\ell_w)\partial_t g(t,z,\ell_z,w,\ell_w)\,\mathrm{d}z\,\mathrm{d}\ell_z\,\mathrm{d}w\,\mathrm{d}\ell_w$$
$$= -\xi \int_H \tilde{\varphi}(z,\ell_z,w,\ell_w)\,\nabla_z \cdot \Big(g(t,z,\ell_z,w,\ell_w)$$
$$\left(\int_{H_1} \nabla_z W(z,\ell_1,u,\ell_2) \frac{g(t,z,\ell_1,u,\ell_2)}{f(t,z)}\,\mathrm{d}\ell_1\,\mathrm{d}\ell_2\,\mathrm{d}u \right) \Big) \mathrm{d}z\,\mathrm{d}\ell_z\,\mathrm{d}w\,\mathrm{d}\ell_w$$
$$+ \int_H \tilde{\varphi}(z,\ell_z,w,\ell_w)\,\nabla_z \cdot \left(g(t,z,\ell_z,w,\ell_w) \left(\int_{H_f} \nabla_z \psi^R(z,u) f(t,u)\,\mathrm{d}u \right) \right) \mathrm{d}z\,\mathrm{d}\ell_z\,\mathrm{d}w\,\mathrm{d}\ell_w$$
$$- \xi \int_H \tilde{\varphi}(z,\ell_z,w,\ell_w)\,\nabla_w \cdot \Big(g(t,z,\ell_z,w,\ell_w)$$
$$\left(\int_{H_1} \nabla_w W(u,\ell_1,w,\ell_2) \frac{g(t,u,\ell_1,w,\ell_2)}{f(t,w)}\,\mathrm{d}\ell_1\,\mathrm{d}\ell_2\,\mathrm{d}u \right) \Big) \mathrm{d}z\,\mathrm{d}\ell_z\,\mathrm{d}w\,\mathrm{d}\ell_w$$
$$+ \int_H \tilde{\varphi}(z,\ell_z,w,\ell_w)\,\nabla_w \cdot \left(g(t,z,l_z,w,l_w) \left(\int_{H_f} \nabla_z \psi^R(u,w) f(t,u)\,\mathrm{d}u \right) \right) \mathrm{d}z\,\mathrm{d}\ell_z\,\mathrm{d}w\,\mathrm{d}\ell_w.$$

This equation represents the weak form of the kinetic equation for g in (4.3.6), after inserting the relation $W = -(V + b)$ and changing back to the original variables x, θ. ∎

Proof of Lemma 4.3.4. First, we only consider the expression of the sum with respect to $i_p = i$ and rewrite it with the help of the according Dirac Delta distributions as follows

$$B_1 := \frac{1}{N} \sum_{i=1}^{N} \nabla_{Z_i} \varphi(Z_i) \cdot \left(\sum_{\substack{p=1 \\ i_p = i}}^{\eta} \nabla_{Z_{i_p}} U\left(Z_{i_p}, \ell_{i_p}, Z_{j_p}, \ell_{j_p}\right) \right)$$

$$= \int_{H_f} \int_H \nabla_u \varphi(u) \cdot \nabla_z U(z, \ell_z, w, \ell_w) \left(\frac{1}{N} \sum_{i=1}^{N} \delta_{Z_i}(u) \left[\sum_{p=1}^{\eta} \tilde{\delta}_{i_p=i} \, \delta_{Z_{i_p}}(z) \delta_{\ell_{i_p}}(\ell_z) \delta_{Z_{j_p}}(w) \delta_{\ell_{j_p}}(\ell_w) \right] \right) \mathrm{d}z \, \mathrm{d}\ell_z \, \mathrm{d}w \, \mathrm{d}\ell_w \, \mathrm{d}u,$$

where $\tilde{\delta}_{i_p=i}$ denotes the Kronecker delta.
Now, it holds that

$$\begin{aligned} &\frac{1}{N} \sum_{i=1}^{N} \delta_{Z_i}(u) \left[\sum_{p=1}^{\eta} \tilde{\delta}_{i_p=i} \, \delta_{Z_{i_p}}(z) \delta_{\ell_{i_p}}(\ell_z) \delta_{Z_{j_p}}(w) \delta_{\ell_{j_p}}(\ell_w) \right] \\ &\quad = \sum_{p=1}^{\eta} \left(\frac{1}{N} \sum_{i=1}^{N} \delta_{Z_i}(u) \tilde{\delta}_{i_p=i} \right) \delta_{Z_{i_p}}(z) \delta_{\ell_{i_p}}(\ell_z) \delta_{Z_{j_p}}(w) \delta_{\ell_{j_p}}(\ell_w) \\ &\quad = \sum_{p=1}^{\eta} \left(\frac{1}{N} \sum_{i=1}^{N} \tilde{\delta}_{i_p=i} \right) \delta_{Z_{i_p}}(u) \delta_{Z_{i_p}}(z) \delta_{\ell_{i_p}}(\ell_z) \delta_{Z_{j_p}}(w) \delta_{\ell_{j_p}}(\ell_w). \end{aligned}$$

Moreover, since $\frac{1}{N} \sum_{i=1}^{N} \tilde{\delta}_{i_p=i} = \frac{1}{N}$ and for any φ, U it holds

$$\int_{H_f} \int_{H_f} \varphi(u) U(z, \ell_z, w, \ell_w) \delta_{Z_{i_p}}(u) \delta_{Z_{i_p}}(z) \, \mathrm{d}u \, \mathrm{d}z = \int_{H_f} \varphi(z) U(z, \ell_z, w, \ell_w) \delta_{Z_{i_p}}(z) \, \mathrm{d}z,$$

we conclude that

$$B_1 = \frac{1}{N} \int_H \nabla_z \varphi(z) \cdot \nabla_z U(z, \ell_z, w, \ell_w) \left(\sum_{p=1}^{\eta} \delta_{Z_{i_p}}(z) \delta_{\ell_{i_p}}(\ell_z) \delta_{Z_{j_p}}(w) \delta_{\ell_{j_p}}(\ell_w) \right) \mathrm{d}z \, \mathrm{d}\ell_z \, \mathrm{d}w \, \mathrm{d}\ell_w.$$

Similarly, we have for the second term of the sum in equation (4.3.7) that

$$\begin{aligned} B_2 \;&:=\; \frac{1}{N} \sum_{i=1}^{N} \nabla_{Z_i} \varphi\left(Z_i\right) \cdot \left(\sum_{\substack{p=1 \\ j_p=i}}^{\eta} \nabla_{Z_{j_p}} U\left(Z_{i_p}, \ell_{i_p}, Z_{j_p}, \ell_{j_p}\right) \right) \\ &= \frac{1}{N} \int_H \nabla_w \varphi(w) \cdot \nabla_w U(z, \ell_z, w, \ell_w) \left(\sum_{p=1}^{\eta} \delta_{Z_{i_p}}(z) \delta_{\ell_{i_p}}(\ell_z) \delta_{Z_{j_p}}(w) \delta_{\ell_{j_p}}(\ell_w) \right) \mathrm{d}z \, \mathrm{d}\ell_z \, \mathrm{d}w \, \mathrm{d}\ell_w \\ &= \frac{1}{N} \int_H \nabla_z \varphi(z) \cdot \nabla_z U(w, \ell_w, z, \ell_z) \left(\sum_{p=1}^{\eta} \delta_{Z_{i_p}}(w) \delta_{\ell_{i_p}}(\ell_w) \delta_{Z_{j_p}}(z) \delta_{\ell_{j_p}}(\ell_z) \right) \mathrm{d}z \, \mathrm{d}\ell_z \, \mathrm{d}w \, \mathrm{d}\ell_w \\ &= \frac{1}{N} \int_H \nabla_z \varphi(z) \cdot \nabla_z U(z, \ell_z, w, \ell_w) \left(\sum_{p=1}^{\eta} \delta_{Z_{p(1)}}(w) \delta_{\ell_{i_p}}(\ell_w) \delta_{Z_{j_p}}(z) \delta_{\ell_{j_p}}(\ell_z) \right) \mathrm{d}z \, \mathrm{d}\ell_z \, \mathrm{d}w \, \mathrm{d}\ell_w, \end{aligned}$$

where we exchanged z and w and ℓ_z, ℓ_w accordingly in the integral and used the symmetry of U, i.e., that $U(w, l_w, z, l_z) = U(z, l_z, w, l_w)$. Finally, summing the terms B_1 and B_2 as well as using the definition of $g^{K,N}$ leads to

$$\frac{1}{2}\left(B_1 + B_2\right) = \frac{K}{N}\int_H \nabla_z\varphi(z)\cdot\nabla_z U(z,\ell_z,w,\ell_w) g^{K,N}\left(z,\ell_z,w,\ell_w\right)\,\mathrm{d}z\,\mathrm{d}\ell_z\,\mathrm{d}w\,\mathrm{d}\ell_w,$$

with which we conclude the result.

∎

Proof of Lemma 4.3.5. First, by the definition of h^N, we notice that

$$\begin{aligned}
&\sum_{\substack{k=1\\ i_k=i_p}}^{\eta} \nabla_{Z_{i_p}} W\left(Z_{i_k},\ell_{i_k},Z_{j_k},\ell_{j_k}\right) = \\
&\qquad = \sum_{j=1}^{N}\int_{[-\frac{L}{2},\frac{L}{2}]^2} \nabla_{Z_{i_p}} W\left(Z_{i_p},\ell_1,Z_j,\ell_2\right) h^N\left(Z_{i_p},\ell_1,Z_j,\ell_2\right)\,\mathrm{d}\ell_1\,\mathrm{d}\ell_2 \\
&\qquad = N\int_{H_1} \nabla_{Z_{i_p}} W\left(Z_{i_p},\ell_1,u,\ell_2\right) h^N\left(Z_{i_p},\ell_1,u,\ell_2\right) f^N(t,u)\,\mathrm{d}\ell_1\,\mathrm{d}\ell_2\,\mathrm{d}u,
\end{aligned} \tag{4.3.12}$$

with H_1 defined in (4.3.3). Second, we compute (recall that for simplicity we assume that $\psi^R \equiv 0$):

$$\begin{aligned}
&\sum_{p=1}^{\eta} \nabla_{Z_{i_p}}\tilde{\varphi}\left(Z_{i_p},\ell_{i_p},Z_{j_p},\ell_{j_p}\right)\cdot\frac{dZ_{i_p}(t)}{dt} \\
&\quad = \sum_{p=1}^{\eta} \nabla_{Z_{i_p}}\tilde{\varphi}\left(Z_{i_p},\ell_{i_p},Z_{j_p},\ell_{j_p}\right) \\
&\qquad \cdot\left(\frac{1}{2}\nabla_{Z_{i_p}}\sum_{\substack{k=1\\ i_k=i_p}}^{\eta} W\left(Z_{i_k},\ell_{i_k},Z_{j_k},\ell_{j_k}\right) + \frac{1}{2}\nabla_{Z_{i_p}}\sum_{\substack{k=1\\ j_k=i_p}}^{\eta} W\left(Z_{i_k},\ell_{i_k},Z_{j_k},\ell_{j_k}\right)\right) \\
&\quad = \sum_{p=1}^{\eta} \nabla_{Z_{i_p}}\tilde{\varphi}\left(Z_{i_p},\ell_{i_p},Z_{j_p},\ell_{j_p}\right) \\
&\qquad \cdot\left(\frac{1}{2}\int_{H_1}\nabla_{Z_{i_p}} W\left(Z_{i_p},\ell_1,u,\ell_2\right)\ Nh^N\left(Z_{i_p},\ell_1,u,\ell_2\right) f^N(t,u)d\ell_1 d\ell_2 du\right. \\
&\qquad \left. + \frac{1}{2}\int_{H_1}\nabla_{Z_{i_p}} W\left(u,\ell_1,Z_{i_p},\ell_2\right)\ Nh^N\left(u,\ell_1,Z_{i_p},\ell_2\right) f^N(t,u)d\ell_1 d\ell_2 du\right) \\
&\quad = \sum_{p=1}^{\eta} \nabla_{Z_{i_p}}\tilde{\varphi}\left(Z_{i_p},\ell_{i_p},Z_{j_p},\ell_{j_p}\right) \\
&\qquad \cdot\left(\int_{H_1}\nabla_{Z_{i_p}} W\left(Z_{i_p},\ell_1,u,\ell_2\right)\ Nh^N\left(Z_{i_p},\ell_1,u,\ell_2\right) f^N(t,u)d\ell_1 d\ell_2 du\right)
\end{aligned} \tag{4.3.13}$$

where we used (4.3.12) in the second equality and in the last equality the symmetry of W and h^N – with the changes of variables $\ell_1 \leftrightarrow \ell_2$.

With this, we can show that

$$\begin{aligned}
S :=& \frac{1}{K}\sum_{p=1}^{\eta}\left(\nabla_{Z_{i_p}}\tilde{\varphi}\left(Z_{i_p},\ell_{i_p},Z_{j_p},\ell_{j_p}\right)\cdot\frac{dZ_{i_p}(t)}{dt}+\nabla_{Z_{j_p}}\tilde{\varphi}\left(Z_{i_p},\ell_{i_p},Z_{j_p},\ell_{j_p}\right)\cdot\frac{dZ_{j_p}(t)}{dt}\right)\\
&=\int_H g^{K,N}\left(t,z,\ell_z,w,\ell_w\right)\nabla_z\tilde{\varphi}\left(z,\ell_z,w,\ell_w\right)\\
&\qquad\cdot\left(\int_{H_1}\nabla_z W\left(z,\ell_1,u,\ell_2\right)\ Nh^N\left(z,\ell_1,u,\ell_2\right)f^N(t,u)d\ell_1 d\ell_2 du\right)dzd\ell_z dwd\ell_w\\
&+\int_H g^{K,N}\left(t,z,\ell_z,w,\ell_w\right)\nabla_w\tilde{\varphi}\left(z,\ell_z,w,\ell_w\right)\\
&\qquad\cdot\left(\int_{H_1}\nabla_w W\left(u,\ell_1,w,\ell_2\right)\ Nh^N\left(u,\ell_1,w,\ell_2\right)f^N(t,u)d\ell_1 d\ell_2 du\right)dzd\ell_z dwd\ell_w\\
&=: S_1+S_2.
\end{aligned}$$

Indeed, we compute S_1, which is the first summand of the last expression:

$$\begin{aligned}
S_1 =& \int_H g^{K,N}\left(t,z,\ell_z,w,\ell_w\right)\nabla_z\tilde{\varphi}\left(z,\ell_z,w,\ell_w\right)\\
&\qquad\cdot\left(\int_{H_1}\nabla_z W\left(z,\ell_1,u,\ell_2\right)\ Nh^N\left(z,\ell_1,u,\ell_2\right)f^N(t,u)d\ell_1 d\ell_2 du\right)dzd\ell_z dwd\ell_w\\
=& \frac{1}{2K}\sum_{p=1}^{\eta}\nabla_{Z_{i_p}}\tilde{\varphi}(Z_{i_p},\ell_{i_p},Z_{j_p},\ell_{j_p})\\
&\qquad\cdot\left(\int_{H_1}\nabla_{Z_{i_p}} W\left(Z_{i_p},\ell_1,u,\ell_2\right)\ Nh^N\left(Z_{i_p},\ell_1,u,\ell_2\right)f^N(t,u)d\ell_1 d\ell_2 du\right)\\
&+\frac{1}{2K}\sum_{p=1}^{\eta}\nabla_{Z_{j_p}}\tilde{\varphi}(Z_{j_p},\ell_{j_p},Z_{i_p},\ell_{i_p})\\
&\qquad\cdot\left(\int_{H_1}\nabla_{Z_{j_p}} W\left(Z_{j_p},\ell_1,u,\ell_2\right)\ Nh^N\left(Z_{j_p},\ell_1,u,\ell_2\right)f^N(t,u)d\ell_1 d\ell_2 du\right)\\
=& \frac{1}{2}S,
\end{aligned}$$

where the first equality follows from the definition of $g^{K,N}$ and the last equality follows from (4.3.13) and the symmetry of $\tilde{\varphi}$, W and h.

Since for S_2 we have the symmetric expression, we obtain that $S_1 = S_2$. Therefore, $S_1+S_2 = S$, from which we conclude the result.

∎

4.4 Conclusions and Future Works

Our goal was to provide a clear and self-contained derivation of the kinetic equation for link-mediated fiber interactions, starting from the microscopic dynamics and relying exclusively on

empirical measures. In doing so, we have recast the heuristic arguments of [15, 39] – based on counting and conditional probabilities – into a measure-theoretic framework that makes explicit the structural assumptions required for a mean-field passage.

With this derivation, we have highlighted the two factors that are key to rigorously proving the mean-field limit in Theorem 4.3.3, namely, Assumptions 1 and 2. The first assumption has to do with having a bijection between fiber labels and the values that they take. We justified this for discrete N since the repulsive potential should impede particles with different labels from taking the same position. However, it is unclear if this property would hold in the limit $N \to \infty$. Regarding the second assumption, it is key to have that Nh^N converges, where here h^N can be interpreted as the connectivity matrix. This function connects with the theory of graphons that will be explored in the future to make these results rigorous.

Still, many other open questions remain, to just name a few: establishing tightness and propagation of chaos results for the pair of empirical objects (fiber distribution and link measure); proving well-posedness and regularity for the limiting kinetic equation; and exploring stochastic variants (e.g., noisy alignment and random link dynamics) within the same measure-based methodology.

4.5 Appendix: Effect of the Linking and Unlinking on $g^{K,N}$

We describe the stochastic linking and unlinking dynamics of the fibers via a jump process. In this process, the link measure $g^{K,N} = g^{K,N}(t, x, \theta_x, \ell_x, y, \theta_y, \ell_y)$ undergoes the following jumps:

Creation of a link. When a link between two fibers at positions (x, θ_x) and (y, θ_y) is created, the link measure $g^{K,N}$ jumps as

$$g^{K,N} \mapsto g^{K,N} + \frac{1}{2K}\delta_{[(x,\theta_x,\ell_x);(y,\theta_y,\ell_y)]},$$

at rate

$$\frac{\nu_l}{N}\,\Gamma(x, \theta_x, y, \theta_y)\, Nf^N(t, x, \theta_x)\, Nf^N(t, y, \theta_y),$$

where $Nf^N(t, x, \theta_x)$ gives the number of fibers at position (x, θ_x).

Destruction of a link. When an existing link between two fibers at states (x, θ_x) and (y, θ_y) is destroyed, the link measure $g^{K,N}$ jumps as

$$g^{K,N} \mapsto g^{K,N} - \frac{1}{K}\delta_{[(x,\theta_x,\ell_x);(y,\theta_y,\ell_y)]},$$

at rate

$$\nu_d\, K\, g^{K,N}(t, x, \theta_x, \ell_x, y, \theta_y, \ell_y),$$

where $Kg^{K,N}(t, x, \theta_x, \ell_x, y, \theta_y, \ell_y)$ represents the number of linked fibers at positions (x, θ_x, ℓ_x) and (y, θ_y, ℓ_y) at time t.

List of Figures

List of Tables

Bibliography

[1] J. P. Agnelli, F. Colasuonno, and D. Knopoff. A kinetic theory approach to the dynamics of crowd evacuation from bounded domains. *Mathematical Models and Methods in Applied Sciences*, 25(01):109–129, 2015. ↑2

[2] G. Albi, M. Artina, M. Foransier, and P. A. Markowich. Biological transportation networks: Modeling and simulation. *Analysis and Applications*, 14(01):185–206, 2016. ↑10, 61, 62, 63, 67

[3] G. Albi, M. Burger, J. Haskovec, P. Markowich, and M. Schlottbom. Continuum modeling of biological network formation. In N. Bellomo, P. Degond, and E. Tadmor, editors, *Active Particles, Volume 1 : Advances in Theory, Models, and Applications*, pages 1–48. Springer International Publishing, Cham, 2017. ↑10, 61, 62, 63, 64, 65, 67, 68, 70, 74

[4] G. Albi, L. Pareschi, G. Toscani, and M. Zanella. Recent advances in opinion modeling: Control and social influence. In N. Bellomo, P. Degond, and E. Tadmor, editors, *Active Particles, Volume 1 : Advances in Theory, Models, and Applications*, pages 49–98. Springer International Publishing, Cham, 2017. ↑2

[5] G. Albi, L. Pareschi, and M. Zanella. Opinion dynamics over complex networks: Kinetic modelling and numerical methods. *Kinetic and Related Models*, 10(1):1–32, 2017. ↑2

[6] S. Alt, P. Ganguly, and G. Salbreux. Vertex models: from cell mechanics to tissue morphogenesis. *Philosophical Transactions of the Royal Society B*, 372(1720):20150520, 2017. ↑16

[7] K. Anguige and C. Schmeiser. A one-dimensional model of cell diffusion and aggregation, incorporating volume filling and cell-to-cell adhesion. *Journal of mathematical biology*, 58(3):395–427, 2009. ↑2

[8] C. Astuto, D. Boffi, and F. Credali. Finite element discretization of a biological network formation system: A preliminary study. In C. Parés, M. J. Castro, T. Morales de Luna, and M. L. Muñoz-Ruiz, editors, *Hyperbolic Problems: Theory, Numerics, Applications. Volume II*, HYP 2022. SEMA SIMAI Springer Series, vol 35, pages 247–257. Springer Nature Switzerland, Cham, 2024. ↑62, 69

[9] C. Astuto, D. Boffi, J. Haskovec, P. Markowich, and G. Russo. Comparison of two aspects of a pde model for biological network formation. *Mathematical and Computational Applications*, 27(5):87, 2022. ↑10, 61, 62, 63, 69, 74, 77

[10] C. Astuto, D. Boffi, J. Haskovec, P. Markowich, and G. Russo. Asymmetry and condition number of an elliptic-parabolic system for biological network formation. *Communications on Applied Mathematics and Computation*, 7(1):78–94, 2025. ↑62, 69

[11] J. M. Ball. Mathematics and liquid crystals. *Molecular Crystals and Liquid Crystals*, 647(1):1–27, 2017. ↑20

[12] A.-L. Barabási and R. Albert. Emergence of scaling in random networks. *Science*, 286(5439):509–512, 1999. ↑60

[13] C. Bardos, F. Golse, and C. D. Levermore. Fluid dynamic limits of kinetic equations II convergence proofs for the boltzmann equation. *Communications on Pure and Applied Mathematics*, 46(5):667–753, 1993. ↑2

[14] C. Bardos, F. Golse, and D. Levermore. Fluid dynamic limits of kinetic equations. I. formal derivations. *Journal of Statistical Physics*, 63(1-2):323–344, 1991. ↑2

[15] J. Barré, P. Degond, and E. Zatorska. Kinetic theory of particle interactions mediated by dynamical networks. *Multiscale Modeling & Simulation*, 15(3):1294–1323, 2017. ↑85, 101

[16] M. Barthélemy. Spatial networks. *Physics Reports*, 499(1):1–101, 2011. ↑60

[17] A. Baskaran and M. C. Marchetti. Enhanced diffusion and ordering of self-propelled rods. *Physical Review Letters*, 101(26):268101, 2008. ↑16, 17

[18] A. Baskaran and M. C. Marchetti. Hydrodynamics of self-propelled hard rods. *Physical Review E*, 77(1):011920, 2008. ↑17

[19] B. J. Berne and P. Pechukas. Gaussian model potentials for molecular interactions. *The Journal of Chemical Physics*, 56(8):4213–4216, 1972. ↑10, 17, 19, 34, 89

[20] A. Björck and G. Dahlquist. *Numerical Methods in Scientific Computing Volume II*. Society for Industrial and Applied Mathematics, 2008. ↑73

[21] T. Bodineau, I. Gallagher, L. Saint-Raymond, and S. Simonella. Dynamics of dilute gases: a statistical approach. In *ICM Plenary Lectures*, volume 2, pages 750–795. European Mathematical Society, 2022. ↑17

[22] M. Bodnar and J. J. L. Velázquez. Friction dominated dynamics of interacting particles locally close to a crystallographic lattice. *Mathematical Methods in the Applied Sciences*, 36(10):1206–1228, 2013. ↑17

[23] L. Boltzmann. Weitere Studien über das Wärmegleichgewicht unter Gasmolekülen. volume 66 of *Sitzungsberichte Akademie der Wissenschaften*, pages 275–370. k. und k. Hof- und Staatsdruckerei, Vienna, 1872. ↑1, 2

[24] R. Borsche, A. Klar, A. Meurer, and O. Tse. Mean field models for interacting ellipsoidal particles. *Computers & Mathematics with Applications*, 72(3):704–719, 2016. ↑18

[25] M. Bruna, M. Burger, H. Ranetbauer, and M.-T. Wolfram. Cross-diffusion systems with excluded-volume effects and asymptotic gradient flow structures. *Journal of Nonlinear Science*, 27(2):687–719, 2017. ↑17

[26] M. Bruna, S. J. Chapman, and M. Schmidtchen. Derivation of a macroscopic model for Brownian hard needles. *Proceedings of the Royal Society A: Mathematical, Physical and Engineering Sciences*, 479(2274):20230076, 2023. ↑17

[27] M. Burger, J. Haskovec, P. A. Markowich, and H. Ranetbauer. A mesoscopic model of biological transportation networks. *Communications in Mathematical Sciences*, 17(5):1213–1234, 2019. ↑61, 64, 65, 66, 67

[28] M. C. Calderer, M. G. Forest, and Q. Wang. Kinetic theories and mesoscopic models for solutions of nonhomogeneous liquid crystal polymers. *Journal of Non-Newtonian Fluid Mechanics*, 120(1):69–78, 2004. ↑2

[29] J. A. Carrillo, X. Chen, Q. Wang, Z. Wang, and L. Zhang. Phase transitions and bump solutions of the Keller–Segel model with volume exclusion. *SIAM Journal on Applied Mathematics*, 80(1):232–261, 2020. ↑17

[30] J. A. Carrillo, M. R. D'Orsogna, and V. Panferov. Double milling in self-propelled swarms from kinetic theory. *Kinetic and Related Models*, 2(2):363–378, 2009. ↑2

[31] J. A. Carrillo, M. Fornasier, G. Toscani, and F. Vecil. Particle, kinetic, and hydrodynamic models of swarming. In G. Naldi, L. Pareschi, and G. Toscani, editors, *Mathematical Modeling of Collective Behavior in Socio-Economic and Life Sciences*, pages 297–336. Birkhäuser Boston, Boston, 2010. ↑2

[32] C. Cercignani. *The Boltzmann Equation and Its Applications*, volume 67 of *Applied Mathematical Sciences*. Springer, New York, 1988. ↑1, 2

[33] L.-P. Chaintron and A. Diez. Propagation of chaos: A review of models, methods and applications. I. models and methods. *Kinetic and Related Models*, 15(6):895–1015, 2022. ↑3

[34] F. Chalub, P. Markowich, Be. Perthame, and C. Schmeiser. Kinetic models for chemotaxis and their drift-diffusion limits. *Monatshefte für Mathematik*, 142(1-2):123–141, 2004. ↑2

[35] F. Corson. Fluctuations and redundancy in optimal transport networks. *Physical Review Letters*, 104(4):048703, 2010. ↑10, 60

[36] I. D. Couzin, J. Krause, R. James, G. D. Ruxton, and N. R. Franks. Collective memory and spatial sorting in animal groups. *Journal of Theoretical Biology*, 218(1):1–11, 2002. ↑3

[37] F. Cucker and S. Smale. Emergent behavior in flocks. *IEEE Transactions on Automatic Control*, 52(5):852–862, 2007. ↑2

[38] P. Degond, C. Appert-Rolland, J. Pettré, and G. Theraulaz. Vision-based macroscopic pedestrian models. *Kinetic & related models*, 6(1):809–839, 2013. ↑2

[39] P. Degond, F. Delebecque, and D. Peurichard. Continuum model for linked fibers with alignment interactions. *Mathematical Models and Methods in Applied Sciences*, 26(02):269–318, 2016. ↑2, 8, 11, 23, 85, 86, 87, 94, 101

[40] P. Degond, M. A. Ferreira, and S. Motsch. Damped Arrow–Hurwicz algorithm for sphere packing. *Journal of Computational Physics*, 332:47–65, 2017. ↑16

[41] P. Degond, A. Frouvelle, and J.-G. Liu. From kinetic to fluid models of liquid crystals by the moment method. *Kinetic and Related Models*, 15(3):417–465, 2022. ↑2, 9, 16, 24, 25, 26, 45, 46

[42] P. Degond, A. Frouvelle, and S. Merino-Aceituno. A new flocking model through body attitude coordination. *Mathematical Models and Methods in Applied Sciences*, 27(06):1005–1049, 2017. ↑2, 17

[43] P. Degond, A. Frouvelle, S. Merino-Aceituno, and A. Trescases. Quaternions in collective dynamics. *Multiscale Modelling & Simulation*, 16(1):28–77, 2018. ↑20, 23, 46

[44] P. Degond, A. Frouvelle, S. Merino-Aceituno, and A. Trescases. Hyperbolicity and non-conservativity of a hydrodynamic model of swarming rigid bodies. *Quarterly of Applied Mathematics*, 82(1):35–64, 2024. ↑2

[45] P. Degond, A. Manhart, and H. Yu. A continuum model for nematic alignment of self-propelled particles. *Discrete and Continuous Dynamical Systems - B*, 22(4):1295–1327, 2017. ↑8, 16, 17

[46] P. Degond, A. Manhart, and H. Yu. An age-structured continuum model for myxobacteria. *Mathematical Models and Methods in Applied Sciences*, 28(09):1737–1770, 2018. ↑8, 16, 17

[47] P. Degond and S. Merino-Aceituno. Nematic alignment of self-propelled particles: From particle to macroscopic dynamics. *Mathematical Models and Methods in Applied Sciences*, 30(10):1935–1986, 2020. ↑17, 23, 25, 26, 43, 44, 46, 52

[48] P. Degond, S. Merino-Aceituno, F. Vergnet, and H. Yu. Coupled self-organized hydrodynamics and Stokes models for suspensions of active particles. *Journal of Mathematical Fluid Mechanics*, 21(1):6, 2019. ↑17

[49] P. Degond and S. Motsch. Continuum limit of self-driven particles with orientation interaction. *Mathematical Models and Methods in Applied Sciences*, 18(supp01):1193–1215, 2008. ↑3, 4, 5, 6, 8, 16, 46

[50] Y. Deng, Z. Hani, and X. Ma. Hilbert's sixth problem: derivation of fluid equations via boltzmann's kinetic theory. *arXiv,* 2503.01800, [math.AP], 2025. ↑2

[51] L. Dyson and R. E. Baker. The importance of volume exclusion in modelling cellular migration. *Journal of Mathematical Biology*, 71(3):691–711, 2015. ↑8, 16

[52] B. Düring, J. Franceschi, M.-T. Wolfram, and M. Zanella. Breaking consensus in kinetic opinion formation models on graphons. *Journal of nonlinear science*, 34(4):79, 2024. ↑2

[53] B. Düring, P. Markowich, J.-F. Pietschmann, and M.-T. Wolfram. Boltzmann and Fokker–Planck equations modelling opinion formation in the presence of strong leaders. *Proceedings of the Royal Society. A, Mathematical, physical, and engineering sciences*, 465(2112):3687–3708, 2009. ↑2

[54] B. Düring and M.-T. Wolfram. Opinion dynamics: inhomogeneous Boltzmann-type equations modelling opinion leadership and political segregation. *Proceedings of the Royal Society. A, Mathematical, physical, and engineering sciences*, 471(2182):20150345, 2015. ↑2

[55] A. Eichmann, F. Le Noble, M. Autiero, and P. Carmeliet. Guidance of vascular and neural network formation. *Current Opinion in Neurobiology*, 15(1):108–115, 2005. ↑60

[56] D. Fang, S. Jin, P. Markowich, and B. Perthame. Implicit and semi-implicit numerical schemes for the gradient flow of the formation of biological transport networks. *The SMAI journal of computational mathematics*, 5:229–249, 2019. ↑62, 68

[57] A. Festa, A. Tosin, and M.-T. Wolfram. Kinetic description of collision avoidance in pedestrian crowds by sidestepping. *Kinetic and Related Models*, 11(3):491–520, 2018. ↑2

[58] A. G. Fletcher, M. Osterfield, R. E. Baker, and S. Y. Shvartsman. Vertex models of epithelial morphogenesis. *Biophysical Journal*, 106(11):2291–2304, 2014. ↑16

[59] M. G. Forest, Q. Wang, and R. Zhou. Kinetic theory and simulations of active polar liquid crystalline polymers. *Soft Matter*, 9(21):5207–5222, 2013. ↑2

[60] M. Frigo and S. G. Johnson. The design and implementation of FFTW3. *Proceedings of the IEEE*, 93(2):216–231, 2005. ↑72

[61] I. Gallagher, L. Saint-Raymond, and B. Texier. *From Newton to Boltzmann: hard spheres and shorts-range potentials*, volume 18 of *EMS Zurich Lectures in Advanced Mathematics*. European Mathematical Society, 2014. ↑2

[62] J. Haskovec. Numerical approach to centrality of optimal transportation networks. In A. Sequeira, A. Silvestre, S. S. Valtchev, and J. Janela, editors, *Numerical Mathematics and Advanced Applications ENUMATH 2023, Volume 1*, pages 406–414. Springer Nature Switzerland, Cham, 2025. ↑64, 66

[63] J. Haskovec and Vybíral J. Robust network formation with biological applications. *Networks and Heterogeneous Media*, 19(2):771–799, 2024. ↑64, 65, 66

[64] J. Haskovec, H. Jönsson, L. M. Kreusser, and P. Markowich. Auxin transport model for leaf venation. *Proceedings of the Royal Society A: Mathematical, Physical and Engineering Sciences*, 475(2231):20190015, 2019. ↑61, 64, 65, 66, 67

[65] J. Haskovec, L. M. Kreusser, and P. Markowich. Rigorous continuum limit for the discrete network formation problem. *Communications in Partial Differential Equations*, 44(11):1159–1185, 2019. ↑61, 62, 64, 67

[66] J. Haskovec, L. M. Kreusser, and P. A. Markowich. ODE- and PDE-based modeling of biological transportation networks. *Communications in Mathematical Sciences*, 17(5):1235–1256, 2019. ↑10, 61, 62, 63, 64, 65, 67

[67] J. Haskovec, P. Markowich, and B. Perthame. Mathematical analysis of a PDE system for biological network formation. *Communications in Partial Differential Equations*, 40(5):918–956, 2015. ↑10, 61, 62, 63, 67, 68, 69

[68] J. Haskovec, P. Markowich, B. Perthame, and M. Schlottbom. Notes on a PDE system for biological network formation. *Nonlinear Analysis*, 138:127–155, 2016. ↑61, 62, 63, 67, 68, 81

[69] J. Haskovec, P. Markowich, and G. Pilli. Murray's law for discrete and continuum models of biological networks. *Mathematical Models and Methods in Applied Sciences*, 29(12):2359–2376, 2019. ↑61, 62, 63, 64, 65

[70] J. Haskovec, P. Markowich, and G. Pilli. Tensor PDE model of biological network formation. *Communications in Mathematical Sciences*, 20(4):1173–1191, 2022. ↑62, 63, 67, 69

[71] J. Haskovec, P. Markowich, and S. Portaro. Measure-based approach to mesoscopic modeling of optimal transportation networks. In D. Apushkinskaya, A. Laptev, A. I. Nazarov, and H. Shahgholian, editors, *Friends in Partial Differential Equations. The Nina N. Uraltseva 90th Anniversary Volume*. EMS Press, Berlin, 2025. ↑66

[72] S. Henkes, M. C. Marchetti, and R. Sknepnek. Dynamical patterns in nematic active matter on a sphere. *Physical Review E*, 97(4):042605, 2018. ↑17

[73] J. Herzfeld. Crowding-induced organization in cells: spontaneous alignment and sorting of filaments with physiological control points. *Journal of molecular recognition*, 17(5):376–381, 2004. ↑8

[74] S. Hittmeir, L. Kanzler, A. Manhart, and C. Schmeiser. Kinetic modelling of colonies of myxobacteria. *Kinetic and Related Models*, 14(1):1–24, 2021. ↑2

[75] S. Hittmeir, H. Ranetbauer, C. Schmeiser, and M.-T. Wolfram. Derivation and analysis of continuum models for crossing pedestrian traffic. *Mathematical Models and Methods in Applied Sciences*, 27(07):1301–1325, 2017. ↑2

[76] H. Honda and T. Nagai. Cell models lead to understanding of multi-cellular morphogenesis consisting of successive self-construction of cells. *The Journal of Biochemistry*, 157(3):129–136, 2015. ↑16

[77] D. Hu. *Optimization, Adaptation, and Initialization of Biological Transport Networks.* Notes from lecture, 2013. ↑60

[78] D. Hu and D. Cai. Adaptation and optimization of biological transport networks. *Physical Review Letters*, 111(13):138701, 2013. ↑10, 60, 61, 63, 64, 65, 66, 67

[79] D. Hu and D. Cai. An optimization principle for initiation and adaptation of biological transport networks. *Communications in Mathematical Sciences*, 17(5):1427–1436, 2019. ↑60, 61, 62, 63, 66, 68

[80] D. Hu, D. Cai, and A. V. Rangan. Blood vessel adaptation with fluctuations in capillary flow distribution. *PLOS ONE*, 7(9):1–13, 2012. ↑64

[81] P.-E. Jabin. A review of the mean field limits for vlasov equations. *Kinetic and Related Models*, 7(4):661–711, 2014. ↑2

[82] J. E. Jones. On the determination of molecular fields. I. from the variation of the viscosity of a gas with temperature. *Proceedings of The Royal Society A: Mathematical, Physical and Engineering Sciences*, 106:441–462, 1924. ↑10

[83] Y. Kuramoto. *Chemical oscillations, waves, and turbulence*, volume 19 of *Springer series in synergetics*. Springer, Berlin [u.a.], 1984. ↑2

[84] P. L. Lions and B. Perthame. Propagation of moments and regularity for the 3-dimensional Vlasov-Poisson system. *Inventiones mathematicae*, 105(1):415–430, 1991. ↑2

[85] R. Malinowski. Understanding of leaf development—the science of complexity. *Plants*, 2(3):396–415, 2013. ↑10, 60

[86] S. Merino-Aceituno, S. Plunder, C. Wytrzens, and H. Yoldaş. Macroscopic effects of an anisotropic Gaussian-type repulsive potential: Nematic alignment and spatial effects. *Mathematical Models and Methods in Applied Sciences*, 35(10):2129–2179, 2025. ↑13, 89

[87] O. Michel and J. Biondi. Morphogenesis of neural networks. *Neural Processing Letters*, 2:9–12, 1995. ↑60

[88] V. Narayan, N. Menon, and S. Ramaswamy. Nonequilibrium steady states in a vibrated-rod monolayer: tetratic, nematic, and smectic correlations. *Journal of Statistical Mechanics: Theory and Experiment*, 2006(01):P01005, 2006. ↑8

[89] S. Ngo, F. Ginelli, and H. Chaté. Competing ferromagnetic and nematic alignment in self-propelled polar particles. *Physical Review E*, 86(5):050101, 2012. ↑17

[90] D. Peurichard, F. Delebecque, A. Lorsignol, C. Barreau, J. Rouquette, X. Descombes, L. Casteilla, and P. Degond. Simple mechanical cues could explain adipose tissue morphology. *Journal of Theoretical Biology*, 429:61–81, 2017. ↑11, 85

[91] L. Preziosi, G. Toscani, and M. Zanella. Control of tumor growth distributions through kinetic methods. *Journal of Theoretical Biology*, 514:110579, 2021. ↑2

[92] C. Rackauckas and Q. Nie. Adaptive methods for stochastic differential equations via natural embeddings and rejection sampling with memory. *Discrete and Continuous Dynamical Systems - B*, 22(7):2731–2761, 2017. ↑36

[93] H. Risken. *The Fokker-Planck equation: methods of solution and applications*, volume 18 of *Springer series in synergetics*. Springer, Berlin [u.a.], 1984. ↑2

[94] D. Sedmera. Function and form in the developing cardiovascular system. *Cardiovascular Research*, 91(2):252–259, 2011. ↑10, 60

[95] H. Spohn. *Large scale dynamics of interacting particles*. Texts and monographs in physics. Springer, Berlin [u.a.], 1991. ↑2

[96] A.-S. Sznitman. Topics in propagation of chaos. In P.-L. Hennequin, editor, *Ecole d'Eté de Probabilités de Saint-Flour XIX — 1989*, pages 165–251. Springer Berlin Heidelberg, Berlin [u.a.], 1991. ↑3

[97] M. P. Taylor and J. Herzfeld. Shape anisotropy and ordered phases in reversibly assembling lyotropic systems. *Physical Review A*, 43(4):1892–1905, 1991. ↑8

[98] G. Teschl. *Topics in Linear and Nonlinar Functional Anlaysis*. Graduate Studies in Mathematics. American Mathematical Society, Providence, 2020. ↑21

[99] T. Vicsek, A. Czirók, E. Ben-Jacob, I. Cohen, and O. Shochet. Novel type of phase transition in a system of self-driven particles. *Physical Review Letters*, 75(6):1226–1229, 1995. ↑2, 3

[100] C. Villani. Limite de champ moyen. *Course de DEA*, pages 1–58, 2001. ↑3, 20

[101] E. G. Virga. *Variational Theories for Liquid Crystals*. Chapman and Hall/CRC, New York, 2019. ↑20

[102] H. Wang and P. J. Hoffman. A unified view on the rotational symmetry of equilibiria of nematic polymers, dipolar nematic polymers, and polymers in higher dimensional space. *Communications in Mathematical Sciences*, 6(4):949–974, 2008. ↑35

[103] H. H. Wensink and H. Löwen. Emergent states in dense systems of active rods: from swarming to turbulence. *Journal of Physics: Condensed Matter*, 24(46):464130, 2012. ↑8, 16